# Time-reversal and Interferometry

with applications to forward modeling of wave propagation
and a chapter on receiver functions

Dirk-Jan van Manen
Doctorandus Geophysics 2001
University of Utrecht, the Netherlands

Thesis submitted in fulfilment of
the requirements for the degree of
Doctor of Philosophy

School of GeoSciences
University of Edinburgh
2006

To my parents

*bene et ille, quisquis fuit (ambigitur enim de auctore), cum quareretur ab illo quo tanta diligentia artis spectaret ad paucissimos perventurae, "satis sunt," inquit "mihi pauci, satis est unus, satis est nullus."*

*That fellow, whoever he was (for his identity is uncertain), when asked what good his careful craftsmanship was doing if it would reach only a very few people, did well to answer, "A few are enough for me, one is enough for me, none is enough for me."*

Seneca, Epistulae Morales 7.11

# Declaration

I declare that this thesis has been composed solely by myself and that it has not been submitted, either in whole or in part, in any previous application for a degree. Except where otherwise acknowledged, the work presented is entirely my own.

Dirk-Jan van Manen
September, 2006

# Abstract

In exploration seismics and non-destructive evaluation, acoustic, elastic and electro-magnetic waves sensitive to inhomogeneities in the medium under investigation are used to probe its interior. Waves multiply scattered by the inhomogeneities carry significant information but, due to their non-linear relation with the inhomogeneities, are notoriously difficult to image or invert for subsurface structure. Recently, however, this paradigm may have been broken as it was shown that high-order multiply scattered acoustic waves can be time-reversed and focused onto their original source location through arbitrary, unknown, inhomogeneous media using a so-called time-reversal mirror: in a first step, the multiply scattered waves are recorded on an array of transducers partially surrounding the medium, in the second step the recorded wavefields are time-reversed and re-emitted into the medium (i.e., the time-reversal mirror acts as a linear boundary condition on the medium injecting the time-reversed, multiply scattered wavefield). The multiply scattered waves retrace their paths through the medium and focus on the original source location. In another development the full waveform Green's function between two (passive) receivers has been observed to emerge from crosscorrelation of multiply scattered coda waves. This process is called interferometry. The principal aim of this thesis is to explore the relation between time-reversal and interferometry and to apply the resulting insights to forward modeling of wave propagation in the broader context of inversion. A secondary aim is to see if the seismological receiver function method can be applied to a reflection setting in ways that are both dynamically and kinematically correct. These aims are achieved through: (1) Derivation of an integral representation for the time-reversed wavefield in arbitrary points of an inhomogeneous medium [first, for the acoustic case, based on the Kirchhoff-Helmholtz integral, then for the elastic case based on the Betti-Rayleigh reciprocity theorem]. Evaluation of these integral representations for points other than the original source point will be shown to give rise to the Green's function between the two points. Physically intuitive explanations will be given as to why this is the case. (2) Application of ordinary reciprocity to the integral representation for the time-reversed wavefield to get an expression in terms of sources on the surrounding surface only. This gives rise to an efficient and flexible forward modeling algorithm. By illuminating the medium from the surrounding surface and storing full waveforms in as many points in the interior as possible, full waveform Green's functions between arbitrary points in the volume can be computed by crosscorrelation and summation only. (3) Derivation of an exact, interferometric von Neumann type boundary condition for arbitrary interior perturbed scattering problems. The exact boundary condition correctly accounts for all orders of multiple scattering, both inside the scattering perturbation(s) and between the perturbations and the background model and thus includes all so-called higher-order, long-range interactions. (4) A comprehensive study of the receiver function method in a reflection setting, both kinematically and dynamically. All presented results are verified and illustrated by numerical (finite-difference) modeling. Overall, the results in this thesis demonstrate that, while the original instabilities associated with direct inversion remain, multiply scattered waves *can* be used in an industrial context – both in real-life experiments and in forward modeling – in ways that are stable. The presented advances in forward modeling are argued to have a significant impact on inversion as well, albeit indirectly.

# Acknowledgements

This thesis would not have been possible without the support of many people. First and foremost, however, I would like to thank my parents, sister and brother for their continuing and unconditional support. No matter how complicated the topic of my research, they have always taken an active interest and insisted on understanding at least the basics of what I was doing. My living abroad wasn't always easy, but they understood very early on that this was something I had to do.

Second of all, I want to thank my supervisors, Dr. Johan Robertsson and Dr. Andrew Curtis, for giving me this unique opportunity to do my Ph.D. research under their supervision. It has been a privilege to work with them, and I have learned from them far beyond the topic of the thesis or simply academic terms. I owe a lot of where I am today to them.

Of course, also, none of this would have happened were it not for the initial internships of my good friends and fellow students from Utrecht University: Robbert van Vossen and Remco Muijs. They got the ball rolling and ensured that many of the initial stays in Oslo and Cambridge were a success, both geophysically and socially. Later on, they made sure that whenever I returned to the Netherlands, there would be an opportunity to catch-up and unwind, usually over the course of a great meal.

I also would like to thank here, Annie and Shannon Tofts, who, despite their already busy household with two young daughters, have put me up time and time again on incredibly short notice. Whenever I was returning to Edinburgh after several months, they have welcomed me as part of their family. It was also a great experience to see Olivia and Rosie grow up.

Many friends and colleagues (often synonymous when living abroad) have also proven invaluable during the last few years. From my time in Gatwick before the

Ph.D. research started: Denis and Celine, Alexis and Marika, Christelle and Fred, and Elena. Our trips to Switzerland and Liechtenstein are unforgettable. From Oslo: Aslaug, Kambiz and later on Kurt, Kemal, Sriram and Pranav and Barbara. And in Edinburgh: Sonja, Baerbel, Fahad, Ira, Guy and Steve. David: I'm passing on the torch to you!

I also want to express my gratitude to the European Union. Without their Marie Curie Industry Host Fellowship Grant under the fifth framework program, I would not have had the opportunity as a Dutch person, to do an Industry based Ph.D. in Norway while at the same time being based at the University of Edinburgh, Scotland.

Finally, I want to thank my grandmother. Without saying it, she is perhaps most excited about what I'm doing.

Dirk-Jan van Manen, 30 October 2006.

# Contents

# List of Tables

# List of Figures

# *Chapter 1*

# Introduction

## 1.1 Breaking the irreversibility paradigm

> *We report the first experiments showing the reversibility of transient acoustic waves through high-order multiple scattering by means of an acoustic time-reversal mirror.*

Derode et al., 1995, Phys. Rev. Lett. 75(23), pp. 4206-4209.

With this somewhat cryptic sentence researchers from the Laboratoire Ondes et Acoustique, Universite Paris VII announced the results of their ground breaking experiments to an astonished and even skeptical community of physicists. Further describing their experiments and results, they continued:

> *A point source generates a pulse which scatters through 2000 steel rods immersed in water. The time-reversed waves are found to converge to their source and recover their original wave form, despite the high order of multiple scattering involved and the usual sensitivity to initial conditions of time-reversal processes.*

The experimental setup of Derode *et al.* (1995) is reproduced in figure 1.1. The whole setup is submerged in water (sound speed c=1500 m/s). On the left an ultrasonic acoustic source is shown, emitting a short 3MHz pulse. In the middle a forest of steel rods causes strong multiple scattering of the pulse. On the right, a linear array of 128 piezo-electric transducers records the scattered wavefield, time-reverses it, and sends it back into the medium.

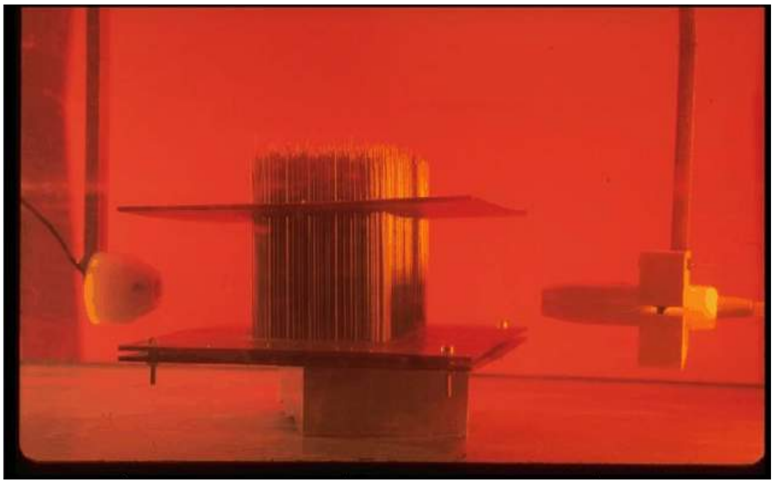

**Figure 1.1:** Experimental setup used by Derode *et al.* (1995) to demonstrate the reversibility of transient acoustic waves through high-order multiple scattering. The whole setup is submerged in water (sound speed c=1500 m/s). On the left an ultrasonic acoustic source is shown, emitting a short 3MHz pulse. In the middle a forest of steel rods causes strong multiple scattering of the pulse. On the right, a linear array of 128 piezo-electric transducers records the scattered wavefield, time-reverses it, and sends it back into the medium. Despite the strong multiple scattering the wavefield retraces its complex path through the medium and focuses on the original source location.

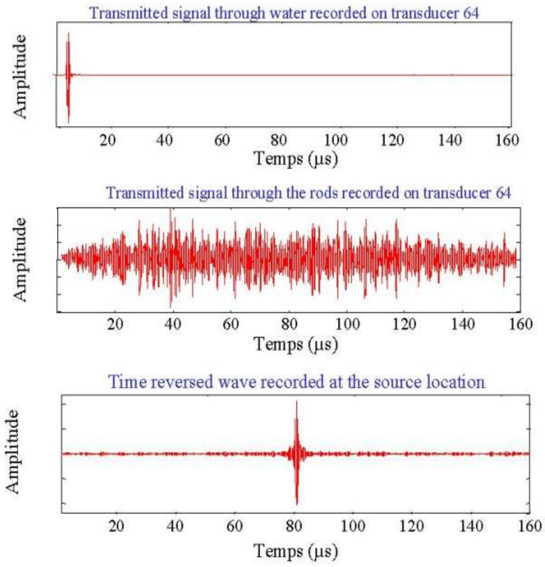

**Figure 1.2:** Experimental results of Derode *et al.* (1995), demonstrating the reversibility of transient acoustic waves through high-order multiple scattering. In the top panel, the 3MHz acoustic pulse is shown. In the middle panel, the strongly scattered signal recorded on the central transducer is shown. Note that the span of the time-axis is unchanged. In the bottom panel, the signal recorded at the original source location after time-reversal is shown. Despite the strong multiple scattering the wavefield focuses on the original source location and the 160 $\mu$s signal is re-compressed to the original duration of the source pulse.

The results are shown in figure 1.2. Despite the strong multiple scattering the wavefield retraces it complex path through the medium and focuses on the original source location!

While it had been known for centuries that the wave-equation in theory is invariant for time-reversal[1], in practice, the nonlinear dependence of the multiply scattered waves on the medium and the finite knowledge of the medium and precision of the recording equipment were expected to lead to instabilities in the reversal process and destroy the time-reversal. And there were good reasons to believe this: after all, it was found to do so in imaging and inversion of acoustic, electro-magnetic and elastic waves and quantum mechanical potentials. Interestingly, even Derode *et al.* (1995) maintain this view as they refer to:

> *the usual sensitivity to initial conditions of time-reversal processes.*

Could it really be that Derode *et al.* (1995) had succeeded in doing the impossible? This would truly be remarkable because it appears to defy the 2$^{\mathrm{nd}}$ law of thermodynamics, which gives time its direction. Throw a stone in the pond and one observes the ripples diverging, however the physically equally plausible converging waves are never observed. Yet, the reported experimental results proved extremely robust and sparked a wave of research into multiple scattering. The apparent paradox of stability was later elegantly resolved in an illuminating comment by Snieder and Scales (1998):

> *The upshot of this issue is that when one discusses instability of multiple scattering processes one should carefully state whether one refers to instability of the wavefield to perturbations of the boundary conditions, instability of the wavefield to perturbations of the medium, or instability of the inverse problem to perturbations of the data. These are different issues that should not be confused. In any case, the experiments of Finks group have shown that it is possible to make use of multiply-scattered waves in an industrial context.*

Roughly at the same time as Derode *et al.* (1995) reported their remarkable results, researchers in the apparently unrelated fields of diffuse field ultrasonics

---

[1] Since the wave equation only contains 2$^{\mathrm{nd}}$ order derivatives in time, replacing $t$ by $-t$ in a solution does not change the result.

and optics were starting to observe phenomena that could not be accounted for using even the most complicated diffusive field theories of radiative transfer. Diffuse ultrasonic fields are usually described without reference to any but the simplest and most local aspects of field phase (Weaver and Lobkis, 2006). Yet coherent backscattering (Akkermans *et al.*, 1988; de Rosny *et al.*, 2004) and Anderson localization (Weaver, 1990) were emerging examples where the global phase of the wavefield could no longer be ignored.

Draeger and Fink (1999), working on one-bit time-reversal of a multiply scattered wavefield propagating on a silicon wafer, were able to show both theoretically and experimentally that by correlation of a chaotic wavefield at points A and B due to a single source at C, the Green's function between the two points is obtained, convolved with the backscattering response from a source point C to itself. They called their relation the "cavity equation". The derivation was based on normal mode theory and the fact that non-diagonal terms in the crosscorrelation of the modal expansions can be ignored if the boundary of the silicon wafer satisfies certain ergodicity properties.

In diffuse field ultrasonics, a similar argument led Weaver and Lobkis (2001) to predict the emergence of the Green's function of a medium from field-field correlations of diffuse fields. The prediction was essentially confirmed in experiments using thermally excited elastic waves (thermal phonons) in finite bodies at MHz frequencies (Weaver and Lobkis, 2001, 2003).

Separately, in exploration seismology, Wapenaar (2003) and Wapenaar *et al.* (2004), using one way reciprocity theorems of the correlation type, succeeded in proving the conjecture by Claerbout (1968) that the reflection response for arbitrary inhomogeneous 3D-media can be computed from the crosscorrelation of noise recordings in a process called "daylight imaging". In an early influential paper titled "Synthesis of a layered medium from its acoustic transmission response" in 1968, Claerbout had shown that the reflection seismogram from a surface source and a surface receiver is one side of the autocorrelation of the seismogram from a source at depth and the same receiver[2]. What distinguishes all these methods is their ability to use the full multiply scattered wave field in a constructive and stable way.

---

[2] Interestingly, he also speculated on that "the synthesis problem with p-sv conversions may be solvable with two-channel time-series analysis."

Without immediately realizing it, Claerbout, Draeger, Weaver and Wapenaar (and their co-workers) had all discovered a process that is now known as interferometric Green's function construction. In interferometry, waves recorded at two receiver locations are correlated to find the Green's function between the locations. The central idea in interferometry is that there may be energy which propagates from an original source point to one of the receiver locations *via* the other receiver location. This energy is recorded at both receivers and, per definition, the path leading up to the first receiver is the same. By crosscorrelating the data, such overlapping paths are removed and the resulting event in the crosscorrelation has a traveltime that corresponds to a wave propagating between the two receivers[3]. Of course, there will also be many spurious events resulting from crosscorrelation between events that do not have a part of their path in common. However, by stacking crosscorrelations for many, appropriately distributed, source locations such spurious events can be removed while the true overlapping paths will be preserved[4].

Finally, Derode *et al.* (2003) showed that there exists a close link between time-reversed acoustics and interferometry. By heuristically reasoning what would be observed when watching time-reversal in a point other than the original source point he was able to show that the time-reversed Green's function between the source point and the second point would be observed. Thus, by replacing one (passive) receiver from the previous paragraph by a source, it becomes clear that the overlapping paths (now occurring between the second point and the time-reversal mirror) are undone in the time-reversal. Thus, the Green function can be recovered as long as the sources in the medium are distributed forming a perfect time-reversal device.

---

[3] Incidentally, the use of crosscorrelations to find traveltime differences between related events on two traces is also a central theme in chapter 5, where the receiver function method will be discussed

[4] At this point, the terms "stacking" and "appropriately distributed" are rather vague and it is not intuitively clear why the spurious events should interfere destructively while the signal interferes constructively. In chapters 2, and 3, these claims will be backed up and formally derived for acoustic and elastodynamic wave propagation and the conditions for appropriate distribution discussed in detail.

## 1.2 Remaining quest(ions) for the coda

When looking at the recent developments surrounding the use of multiply scattered waves a pattern emerges: In all these methods successfully making use of coda waves (i.e., coda wave interferometry, time-reversal and reflection-transmission transforms) crosscorrelation is the essential ingredient, or equivalently, convolution with the time-reverse. Indeed, by now it is well accepted that these algorithms all belong to the same class.

Yet important questions remain unanswered. Under which conditions exactly do the Green's functions emerge? How do we reconcile the results for random and deterministic media (diffuse versus complex wavefields)? In random media, the (uncontrolled) sources, usually distributed throughout the medium, are assumed to be spatially and temporally uncorrelated and have white noise spectra. Construction involves crosscorrelation of just two passive noise recordings of long duration, but no integration. In deterministic media, on the other hand, the sources are typically controlled and they surround the area of interest.

In the following, I show that for deterministic media (and, incidentally, for random media as well), provided the sources on the surrounding surface are excited separately, the Green's function can be reconstructed without having to rely on so-called time/event averaging (see below). Constructive and destructive interference instead arises by integration over the surrounding surface. A physical explanation based on Huygens' principle is given. In contrast, in random media, since a superposition of uncontrolled sources is measured, constructive and destructive interference arises precisely and only because the unwanted cross-terms in the correlation are in the ensemble average uncorrelated and vanish thence.

Time/event averaging also raises questions about convergence rate of the emerging Green's function. Is it feasible to have uncorrelated simultaneous sources on the surrounding surface of a deterministic medium as well? Snieder (2002) discusses the emergence of the ballistic wave in surface wave interferometry and finds that there is a fundamental limit to the signal-to-noise ratio for a given record length and number of observations. In later chapters, where interferometry is exploited in the forward modeling of wave propagation, I explore the possibility of encoding the sources on the surrounding surface using pseudo-noise sequences and firing them simultaneously and derive similar fundamental limits on encoding and decoding.

How do the boundary conditions affect the reconstruction? What is the difference between interferometry in (partially) open versus closed media? I argue that, since time-reversal and interferometric Green's function construction are based on reciprocity theorems of the correlation type and since the media in the forward and time-reversed states are identical and have the same boundary conditions, it follows that no sources are required on interfaces with homogeneous boundary conditions. This is confirmed in the given examples. Also, the implications of having outgoing (absorbing or radiation) boundary conditions on (part of) the surrounding surface are discussed, as this leads to a simplification in the reconstruction formula and/or a reduced illumination or modeling effort.

With the scene set by these remarkable observations and remaining unanswered questions, I now give a brief formal outline of the thesis.

## 1.3 Outline of the thesis

In chapter 2, a methodology based on time-reversal and interferometry is presented that provides a new perspective on modeling of wave propagation in generally inhomogeneous media. The approach relies on a representation theorem of the wave equation to express the Green's function between points in the interior as an integral over the response in those points due to sources on a surface surrounding the medium. A highly efficient two-stage modeling algorithm is then discussed where, in an initial phase, the model is systematically illuminated from a surface surrounding the medium using a sequence of conventional forward modeling runs and, in a second phase, Green's functions between arbitrary points in the volume can be computed by crosscorrelation and summation. The method is illustrated on the acoustic Pluto model and a physical interpretation of the Green's function reconstruction is given. A possible redundancy in the boundary source illumination is also investigated.

In chapter 3, the interferometric modeling method is extended to elastic media and many of the key ideas introduced in chapter 2 are now discussed and explained in more detail. It is shown how the "theorem" by Derode *et al.* (2003) can be derived from an elastodynamic representation theorem. Connections with the Porter-Bojarski equation in the field of generalized holography in optics (Porter, 1969, 1970; Bojarski, 1983) and reciprocity theorems of the correlation type (de Hoop, 1988, 1995; Fokkema and van den Berg, 1993; Wapenaar, 2004) are also explored. A step-by-step example illustrates the method on an acoustic model consisting of isotropic point scatterers embedded in a homogeneous background medium. This is followed by an example for a complex region of the elastic Pluto model and a detailed discussion of computational aspects. A method to drastically speed up the initial forward modeling phase, by encoding the boundary sources and exciting them simultaneously, is also discussed.

In chapter 4, I show that the interferometric modeling method may provide the crucial missing component of an efficient forward modeler in a waveform inversion engine, as an exact boundary condition for arbitrary inhomogeneous locally perturbed scattering problems is proposed. The method uses a source wavefield recorded for the unperturbed model as a boundary condition on the truncated computational domain and updates this boundary condition at every timestep. This is done by extrapolating the wavefield scattered off the perturbations from a surface surrounding the perturbations to the boundary with a Kirchhoff integral. The boundary condition preserves all high-order long-range interactions with the unperturbed background model. Using the interferometric modeling method all Green's functions required for the source wavefield and the extrapolation through the unperturbed model to update the boundary condition (BC) can be computed efficiently and flexibly. Interferometric modeling also removes the need to define the perturbation regions in advance. The method is illustrated using a simple one-dimensional (1D) example.

In chapter 5, I show that the recent work in the seismological community on kinematic aspects of receiver function processing can be extended significantly, by building on relevant results from the exploration and production seismic community in the areas of velocity analysis, stacking and migration. I also propose two alternative ways of receiver function calculation, beyond the usual slowness domain approach: space-time domain (2D) deconvolution, which treats the spatial aspects of mode-conversion completely analogously to the temporal aspects, and model independent receiver function calculation. This last approach enables, at least in theory, complete removal of an incident mode in arbitrarily complex inhomogeneous media, demonstrating the full potential of receiver function calculation in terms of source equalization. Dynamic aspects of receiver function processing are also discussed as these naturally arise when examining the differences between receiver function calculation in a reflection and a transmission setting.

In chapter 6, a discussion and outlook are provided for the work on time-reversal and interferometry, the exact boundary condition and receiver functions. It is argued that the interferometric modeling method is ideally suited for "tunable" full waveform modeling, where accuracy can be traded-off for computational efficiency, without compromising on multiple scattering and maintaining sensitivity to the full seismogram. A suite of suggestions is provided to support this. I also suggest that, by combining the flexibility of interferometric modeling with so-called finite-difference injection methods (Robertsson and Chapman, 2000), we have the essential ingredients for efficient and flexible targeted full waveform inversion. The potential of frequency domain implementations of interferometric modeling is also highlighted. Finally, the outlook for reflection seismic receiver functions is presented.

First, however, we start with time-reversed acoustics and its relation with interferometry and full waveform modeling.

## *Chapter 2*

# Modeling of wave propagation in inhomogeneous media[1]

We present a methodology providing a new perspective on modeling and inversion of wave propagation satisfying time-reversal invariance and reciprocity in generally inhomogeneous media. The approach relies on a representation theorem of the wave equation to express the Green's function between points in the interior as an integral over the response in those points due to sources on a surface surrounding the medium. Following a predictable initial computational effort, Green's functions between arbitrary points in the medium can be computed as needed using a simple cross-correlation algorithm.

## 2.1 Introduction

Many applications in diverse fields such as communications analysis, waveform inversion, imaging, survey and experimental design, and industrial design, require a large number of modelled solutions of the wave equation in different media. The most complete methods of solution, such as finite differences (FD), which accurately model all high-order interactions between scatterers in a medium, typically become prohibitively expensive for realistically complete descriptions

---

[1] This chapter has been published as: van Manen, D., Robertsson, J.O.A., and Curtis, A., 2005, Modeling of wave propagation in inhomogeneous media, Physical Review Letters, Vol. 94, pp. 164301 (week ending 29 APRIL 2005).

of the medium and the geometries of sources and receivers and hence for solving realistic problems based on the wave equation. Here we show that the key to breaking this apparent paradigm lies in a basic reciprocity argument in combination with recent theoretical advances in the fields of time-reversed acoustics (Derode *et al.*, 2003) and interferometric seismic imaging (Weaver and Lobkis, 2001; Wapenaar *et al.*, 2004; Wapenaar, 2004; Schuster, 2001).

In time-reversed acoustics, invariance of the wave equation for time-reversal can be exploited to focus a wave field through a highly scattering medium on an original source point (Derode *et al.*, 1995). Cassereau and Fink (1992, 1993) realized that the acoustic representation theorem (Wapenaar and Fokkema, 2004) can be used to time-reverse a wave field in a volume by creating secondary sources (monopole and dipole) on a surface surrounding the medium such that the boundary conditions correspond to the time-reversed components of a wave field measured there. These secondary sources give rise to the back-propagating, time-reversed wave field inside the medium that collapses onto itself at the original source location. Note that since there is no source term absorbing the converging wave field, the size of the focal spot is limited to half a (dominant) wavelength in accordance with diffraction theory (Cassereau and Fink, 1992). The diffraction limit was overcome experimentally by de Rosny and Fink (2002) by introducing the concept of an “acoustic sink”.

In interferometry, waves recorded at two receiver locations are correlated to find the Green’s function between the locations. Interferometry has been successfully applied to helioseismology (Rickett and Claerbout, 2000), ultrasonics (Weaver and Lobkis, 2001) and exploration seismics (Wapenaar *et al.*, 2004). Recently it was shown that there exists a close link between the time-reversed acoustics and interferometry disciplines when Derode *et al.* (2003) analyzed the emergence of the Green’s function from field-field correlations in an open scattering medium in terms of time-reversal symmetry. The Green’s function can be recovered as long as the sources in the medium are distributed forming a perfect time-reversal device. A rigorous proof for the general case of an arbitrary inhomogeneous elastic medium was presented by Wapenaar (2004).

## 2.2 Theory and Method

Our starting point is the acoustic wave equation in the space-frequency domain: $\partial_i(\rho^{-1}\partial_i p)+(\omega^2/K)p = f$, where $p = p(\mathbf{x}, \omega)$ denotes the pressure field at location $\mathbf{x}$ and frequency $\omega$, $\rho(\mathbf{x})$ and $K(\mathbf{x})$ denote the mass density and incompressibility respectively and $f = f(\mathbf{x}, \omega)$ is a source term denoting the change of volume injection rate density over time. Now consider two states $A$ and $B$ that could occur in the same medium independently: $\partial_i(\rho^{-1}\partial_i p^A) + (\omega^2/K)p^A = f^A$ and $\partial_i(\rho^{-1}\partial_i p^B) + (\omega^2/K)p^B = f^B$. The acoustic representation theorem can be derived by multiplying the equation for the first state by $p^B(\mathbf{x}, \omega)$ and the equation for the second state by $p^A(\mathbf{x}, \omega)$, subtracting and integrating the results over a volume $V$, applying Gauss' theorem to convert the volume integral to a surface integral and identifying state $A$ with a mathematical state [i.e., a state involving (analytic) Green's functions rather than measured quantities (Wapenaar and Fokkema, 2004)]: $f^A(\mathbf{x}) = \delta(\mathbf{x} - \mathbf{x}')$ and $p^A(\mathbf{x}) = G(\mathbf{x}, \mathbf{x}')$, where $\delta(\mathbf{x})$ denotes the Dirac delta distribution and $G(\mathbf{x}, \mathbf{x}')$ the Green's function due to a source at $\mathbf{x}'$. Following a reciprocity argument, interchanging the coordinates $\mathbf{x} \leftrightarrow \mathbf{x}'$ and dropping the superscripts for state $B$ this procedure yields:

$$\begin{aligned} p(\mathbf{x}) = &\int_V G(\mathbf{x}, \mathbf{x}')f(\mathbf{x}')\mathrm{d}V' \\ &+ \int_S \frac{1}{\rho(\mathbf{x}')} \left[\nabla' G(\mathbf{x}, \mathbf{x}')p(\mathbf{x}') - G(\mathbf{x}, \mathbf{x}')\nabla' p(\mathbf{x}')\right] \cdot \mathbf{n}\, \mathrm{d}S', \end{aligned} \tag{2.1}$$

where $\nabla' G(\mathbf{x}, \mathbf{x}')$ denotes the gradient of the Green's function with respect to primed coordinates and $\mathbf{n}$ the normal to the boundary. Thus, the wave field can be computed everywhere inside the volume $V$ once the exciting force $f(\mathbf{x}')$ inside the volume and the wave field $p(\mathbf{x}')$ and its gradient $\nabla' p(\mathbf{x}')$ on the surrounding surface $S$ are known. To time-reverse a wave field in a volume $V$, the wave field $p$ and its gradient $\nabla' p$, measured at the surface $S$ in a first step, have to be time-reversed on the surface such that the time-reversed pressure field $p_{tr}(\mathbf{x})$ radiated from the boundary can be written:

$$p_{tr}(\mathbf{x}) = \int_S \frac{1}{\rho(\mathbf{x}')} \left[\nabla' G(\mathbf{x}, \mathbf{x}')p^*(\mathbf{x}') - G(\mathbf{x}, \mathbf{x}')\nabla' p^*(\mathbf{x}')\right] \cdot \mathbf{n}\, \mathrm{d}S', \tag{2.2}$$

where * denotes complex conjugation and we have ignored the volume integral which corresponds to the acoustic sink (de Rosny and Fink, 2002). Note that Eq. 2.2 can be used to compute the time-reversed wave field (including all high-order interactions) at any location, not just at an original source location. Now, assume that the wave field $p(\mathbf{x}')$ was due to a point source at location $\mathbf{x}_1$ and that we have $p(\mathbf{x}') = G(\mathbf{x}', \mathbf{x}_1)$. By measuring the wave field in a second location $\mathbf{x}_2$, the Green's function and its time-reverse between the source point $\mathbf{x}_1$ and the second point $\mathbf{x}_2$ are observed (Derode *et al.*, 2003; Wapenaar, 2004):

$$\begin{aligned} &G^*(\mathbf{x}_2, \mathbf{x}_1) - G(\mathbf{x}_2, \mathbf{x}_1) = \\ &\quad \int_S \frac{1}{\rho(\mathbf{x}')} \left[\nabla' G(\mathbf{x}_2, \mathbf{x}') G^*(\mathbf{x}', \mathbf{x}_1) - G(\mathbf{x}_2, \mathbf{x}') \nabla' G^*(\mathbf{x}', \mathbf{x}_1)\right] \cdot \mathbf{n}\, \mathrm{d}S', \end{aligned} \tag{2.3}$$

where the negative forward Green's function $-G(\mathbf{x}_2, \mathbf{x}_1)$ arises from the missing acoustic sink (Cassereau and Fink, 1992; de Rosny and Fink, 2002). Using reciprocity, we can rewrite Eq. 2.3 so that it involves only sources on the boundary enclosing the medium:

$$\begin{aligned} &G^*(\mathbf{x}_2, \mathbf{x}_1) - G(\mathbf{x}_2, \mathbf{x}_1) = \\ &\quad \int_S \frac{1}{\rho(\mathbf{x}')} \left[\nabla' G(\mathbf{x}_2, \mathbf{x}') G^*(\mathbf{x}_1, \mathbf{x}') - G(\mathbf{x}_2, \mathbf{x}') \nabla' G^*(\mathbf{x}_1, \mathbf{x}')\right] \cdot \mathbf{n}\, \mathrm{d}S'. \end{aligned} \tag{2.4}$$

Thus, the Green's function between two points $\mathbf{x}_1$ and $\mathbf{x}_2$ can be calculated once the Green's functions between the enclosing boundary and these points are known.

A highly efficient two-stage modelling strategy follows from Eq. 2.4: first, the Green's function terms $G$ and $\nabla' G$ are calculated from boundary locations to internal points in a conventional forward modelling phase; in a second inter-correlation phase, the integral is calculated requiring only cross-correlations and numerical integration. Since the computational cost of typical forward modelling algorithms (e.g., FD) does not significantly depend on the number of receiver locations but mainly on the number of source locations, efficiency and flexibility are achieved by storing the wave field modelled for each of the boundary sources in as many points as possible throughout the medium. To calculate the Green's function between two points the recordings in the first point due to the dipole sources on the boundary are cross-correlated with the recordings in the second point due to the monopole sources, and vice-versa. The resulting cross-correlations are subtracted and numerically integrated over the boundary of source locations. Unprecedented flexibility follows from the fact that the Green's function can be calculated between all pairs of points that were defined up front and stored in the initial modelling phase. Thus, we calculate a partial modelling solution that is common to all Green's functions, then a bespoke component for each Green's function.

## 2.3 Results

Our method is illustrated using a FD implementation of the two-dimensional acoustic wave equation for a typical modelling scenario in an exploration seismic setting. In Fig. 2.1 the compressional wave velocity in a 4.6 x 4.6 km representative region of an Earth model often used to benchmark marine seismic imaging algorithms (Stoughton *et al.*, 2001) is shown. Note the high velocity (4500 m/s) salt body on the right. In black, two points of interest (offset 1 km) are shown. The dotted line denotes the boundary with $N_S = 912$ source locations distributed with a density consistent with the local spatial Nyquist frequency. Outgoing (i.e., radiation or absorbing) boundary conditions (Clayton and Engquist, 1977) are applied right outside the surface enclosing the points of interest to truncate the computational domain.

Forward simulations were carried out for each of the 912 source locations on the boundary and the waveforms stored at 90,000 points distributed throughout the model. Note that because of the cross-symmetry of the terms in the integrand in Eq. 2.4, no sources are required along interfaces with homogeneous boundary conditions (e.g., the Earth's free surface). Depending on the particular wave equation (scalar or vector), several forward simulations may have to be carried out for each source location. In the acoustic example two data sets are required: with monopole and dipole sources respectively. However, when the surface surrounding the medium has outgoing boundary conditions, the wave field and its gradient (traction) are directly related (Holvik, 2003). Hence, the normal derivatives can be calculated from the wave field itself without additional modelling. Fig. 2.2 shows the integrand of Eq. 2.4, inversely weighted by boundary source density,

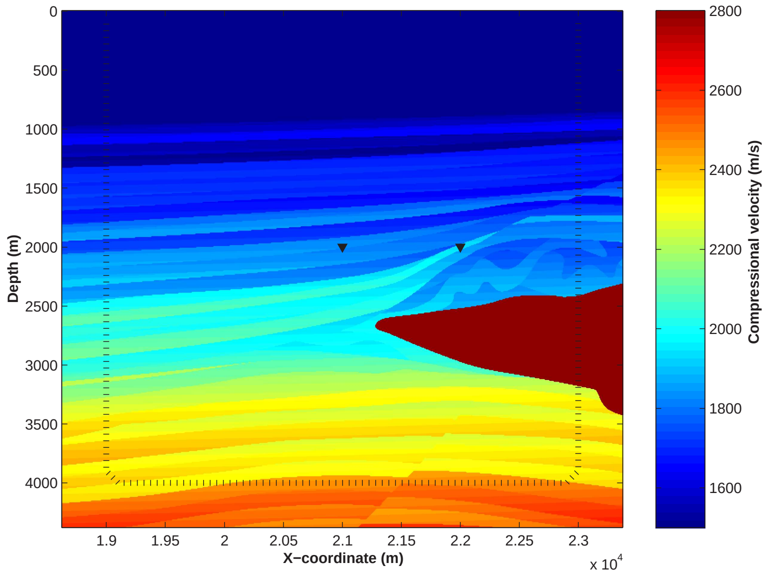

**Figure 2.1:** 2D acoustic marine seismic model [compressional wave velocity] (see e.g., Stoughton *et al.*, 2001, for a description of the model). The color scale is clipped to display weak velocity contrasts (the velocity of salt is 4500 m/s).

for each source location $\mathbf{x}'$ and for the two points $\mathbf{x}_1$ and $\mathbf{x}_2$ in Fig. 2.1. In Fig. 2.3, the resulting Green's function between the points in Fig. 2.1 computed using Eq. 2.4, and a reference trace computed by direct FD modelling, are shown in red and blue respectively.

The signal at negative times corresponds to the waves flowing back in time and opposite direction past the second point. The four inserts show the excellent match between the reference trace and the new method in detail.

Interestingly, the time-series in Fig. 2.2 bear little resemblance to the final Green's function in Fig. 2.3. Eq. 2.4 sums these signals along the horizontal axis and hence relies on the delicate constructive and destructive interference of time-reversed waves back-propagating through the medium, recombining and undoing the scattering at every discontinuity to produce the Green's function.

In Fig. 2.2, each column represents the set of all waves travelling from point $\mathbf{x}_1$ to a single boundary source, correlated with the Green's function from that boundary source to $\mathbf{x}_2$. Some of the waves travelling from $\mathbf{x}_1$ to this boundary source may pass through $\mathbf{x}_2$ before being recorded and therefore have the remainder of their path in common with waves emitted from $\mathbf{x}_2$ in the same direction (or wavenumber). The traveltimes associated with such identical

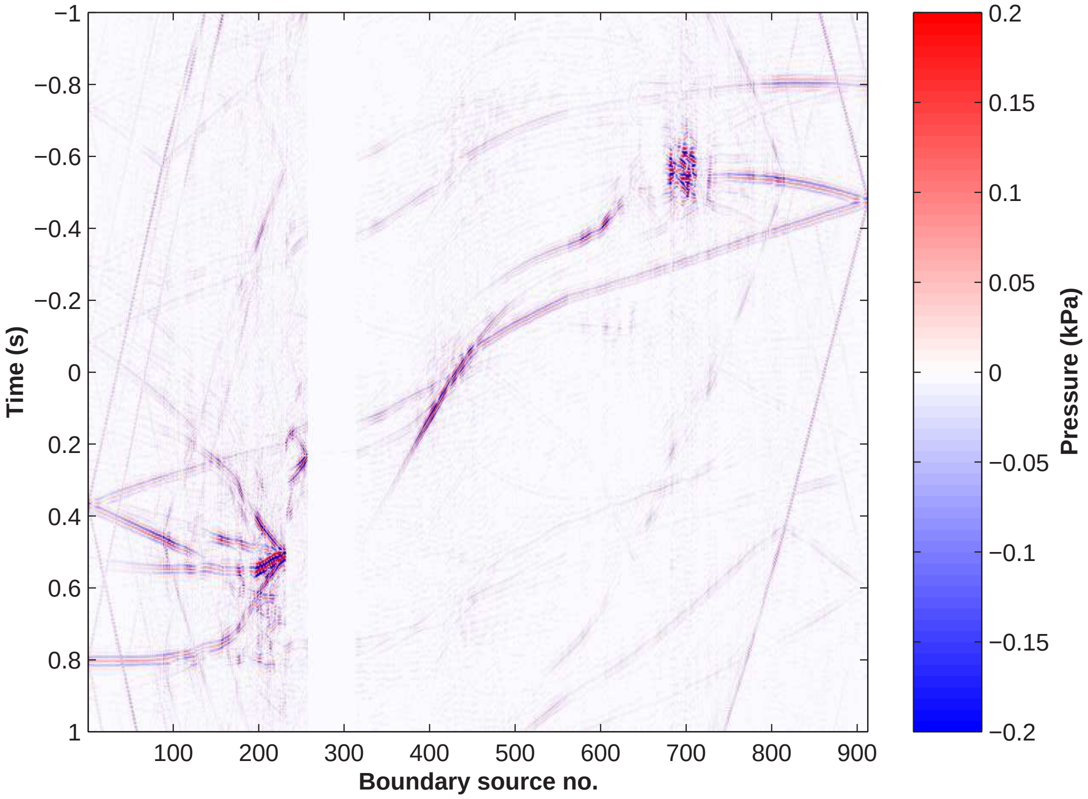

**Figure 2.2:** Green's function inter-correlation gather (weighted) for the two points shown in Fig. 2.1. The low correlation amplitude for boundary sources 250-310 corresponds to the shadow of the salt body.

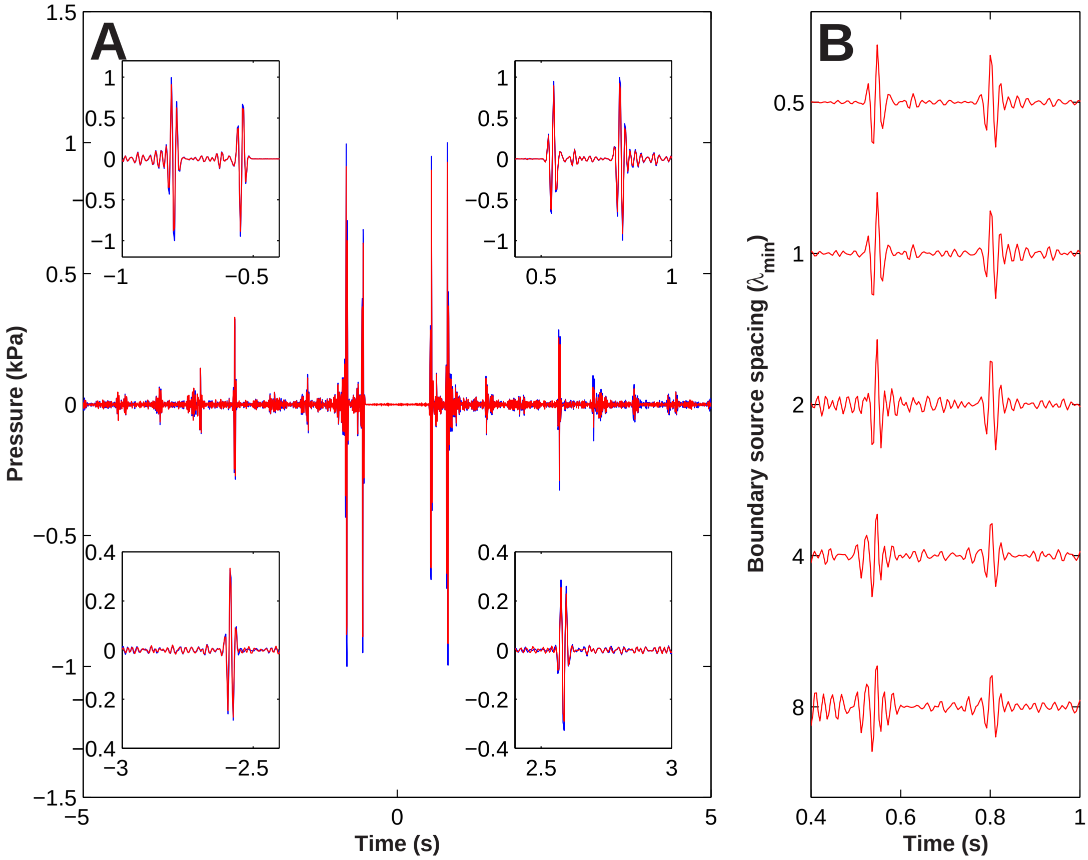

**Figure 2.3:** (A) Waveform computed by summation of the weighted inter-correlation gather shown in Fig. 2.2 (red) compared to a conventional FD computation (blue). Inserts show particular events in the time-series. (B) Waveform computed after successive subsampling of the inter-correlation gather.

parts of the path are eliminated in the cross-correlation and the remaining part corresponds to an event in the Green's function from $\mathbf{x}_1$ to $\mathbf{x}_2$. Similarly, some waves emitted from $\mathbf{x}_2$ may travel to the boundary source location via $\mathbf{x}_1$ and have a common section of path between $\mathbf{x}_1$ and the boundary source. Again traveltime on the common section will be eliminated and give rise to the same event in the Green's function from $\mathbf{x}_1$ to $\mathbf{x}_2$ at negative (a-causal) times. Note that the wavenumbers involved for positive and negative times are in general not parallel since they are related to the background structure of the whole model (one or other may not exist for the same boundary source). Hence, waves at positive and negative times are reconstructed differently. All cross-correlations involving energy that does not pass through $\mathbf{x}_2$ are eliminated by destructive interference by summation of the columns (Snieder, 2004).

The new method is particularly attractive in applications where Green's functions are desired between a large number of points interior to a medium, but where there are no common source or receiver points. No other existing method could offer full waveforms at comparable computational cost. The method also offers great flexibility where the exact interior points are not known in advance since Green's functions can be computed on an "as needed" basis from Green's functions between points on the surrounding surface and its interior. We have shown how the latter Green's functions constitute a common component of all Green's functions in the medium through Eq. 2.4. In the example above, this common component is stored compressed by a factor of 50 compared to explicitly storing all desired Green's functions between pairs of interior points.

Whereas traditional approximate modelling methods typically impose restrictions with respect to the degree of heterogeneity in the medium of propagation or neglect high-order scattering, the new time-reversal modelling methodology allows us instead to compromise on noise level while maintaining high-order scattering and full heterogeneity in the medium. Recent experimental and theoretical work indicates that time-reversed imaging is robust with respect to perturbations in the boundary conditions (Derode *et al.*, 2003; Snieder and Scales, 1998). For cases where the wave propagation is heavily dominated by multiple scattering even a single source may be sufficient to refocus essential parts of a time-reversed signal (Draeger and Fink, 1999). Also for more deterministic models, such as the one in the example, it is possible to substantially reduce the number of sources and still recover essential parts of the signal. In Fig. 2.3B we show the part of the signal corresponding to the insert in the upper right corner of Fig. 2.3A as we reduce the number of sources around the boundary. Even for as few as one sixteenth of the original number of sources we are able to reproduce amplitude and phase of an arrival of interest fairly accurately, but with an increased noise level. Clearly, the required number of sources will depend on the application. Our numerical experiments thus confirm the robustness of the methodology with respect to variations in parameters such as location and discretization of integration surfaces.

We also experimented with exciting the boundary sources simultaneously by encoding the source signals using pseudo-noise sequences (Fan and Darnell, 2003) and with simultaneous sources distributed randomly in the medium (Derode *et al.*, 2003) as two alternative ways to reduce the number of sources. There is a well known limit to the quality of separation of such sequences of a given length when emitted simultaneously (Welch, 1974). Insufficient separation of sequences again is manifest in an increased noise level in the final Green's functions. In all cases, the limits of separation caused relatively high noise levels compared to the equivalent FD effort using the method described above, but for many applications, the possibility to trade-off signal-to-noise ratio to CPU time without compromising on medium complexity or high-order scattering will be another attractive property of the new method.

Thus, we have shown how recent insights into the relationship between Green's theorem and time-reversal can be extended to modelling of wave propagation by invoking reciprocity. We expect that this may significantly change the way we approach modelling and inversion of the wave equation in future.

# *Chapter 3*

# Interferometric modeling of wave propagation in inhomogeneous elastic media using time-reversal and reciprocity[1]

Time-reversal of arbitrary elastodynamic wavefields in partially open media can be achieved by measuring the wavefield on a surface surrounding the medium and applying the time-reverse of those measurements as a boundary condition. We use a representation theorem to derive an expression for the time-reversed wavefield at arbitrary points in the interior. When this expression is used to compute, in a second point, the time-reversed wavefield originating from a point source, the time-reversed Green's function between the two points is observed. By invoking reciprocity we obtain an expression that is suitable for modeling and from this we develop an efficient and flexible two-stage modeling scheme. In the initial phase, the model is systematically illuminated from a surface surrounding the medium using a sequence of conventional forward modeling runs. Full waveforms are stored for as many points in the interior as possible.

---

[1] This chapter has been published as: van Manen, D., Curtis, A., and Robertsson, J.O.A., 2006, Interferometric modeling of wave propagation in inhomogeneous elastic media using time-reversal and reciprocity, Geophysics, Volume 71, Issue 4, pp. SI47-SI60 (July-August 2006).

In the second phase, Green's functions between arbitrary points in the volume can be computed by crosscorrelation and summation of data computed in the initial phase. We illustrate the method with a simple acoustic example and then apply it to a complex region of the elastic Pluto model. It is particularly efficient when Green's functions are desired between a large number of points but where there are no common source or receiver points. The method relies on interference of multiply scattered waves but is stable. We show that encoding the boundary sources using pseudo-noise sequences and exciting them simultaneously, akin to daylight imaging, is inefficient and in all explored cases leads to relatively high noise levels.

## 3.1 Introduction

Many applications in diverse fields such as communications analysis, waveform inversion, imaging, survey and experimental design, and industrial design, require a large number of modeled solutions of the wave equation in different media. The most complete methods of solution, such as finite differences (FD), which accurately model all high-order interactions between scatterers in a medium, typically become prohibitively expensive for realistically complete descriptions of the medium and geometries of sources and receivers, and hence for solving realistic problems based on the wave equation. In chapter 2 (van Manen *et al.*, 2005) I showed that the key to breaking this apparent paradigm lies in combining a basic reciprocity argument with contemporary theoretical advances in the fields of time-reversed acoustics (Derode *et al.*, 2003) and seismic interferometry (Schuster, 2001; Weaver and Lobkis, 2001; Wapenaar *et al.*, 2004).

In time-reversed acoustics, the invariance of the wave equation to time-reversal is exploited to focus a wavefield through a highly scattering medium on an original source point (Derode *et al.*, 1995). Cassereau and Fink (1992, 1993) realized that an acoustic representation theorem can be used to time-reverse a wavefield in a volume by creating secondary sources on a surface surrounding the medium such that the boundary conditions correspond to the time-reversed components of a wavefield measured there. These secondary sources give rise to the back-propagating, time-reversed wavefield inside the medium that collapses onto itself at the original source location. Note that since there is no source term absorbing the converging wavefield, the size of the focal spot is limited to half a (dominant) wavelength in accordance with diffraction theory (Cassereau and Fink, 1992). The diffraction limit was overcome experimentally by de Rosny and Fink (2002) by introducing the concept of an "acoustic sink".

In interferometry, waves recorded at two receiver locations are correlated to find the Green's function between the locations. Interferometry has been successfully applied to helioseismology (Rickett and Claerbout, 2000), ultrasonics (Weaver and Lobkis, 2001) and exploration seismics (Wapenaar *et al.*, 2004; Bakulin and Calvert, 2004, 2006). Recently it was shown that there exists a close link between the time-reversed acoustics and interferometry disciplines when Derode *et al.* (2003) analyzed the emergence of the Green's function from field-field correlations in an open scattering medium in terms of time-reversal symmetry. The Green's function can be recovered as long as the sources in the medium are distributed forming a perfect time-reversal device.

Here, we extend the interferometric modeling introduced in chapter 2 (van Manen *et al.*, 2005) to elastic media and show how the "theorem" by Derode *et al.* (2003) can be derived from an elastodynamic representation theorem. We emphasize the connection with the Porter-Bojarski equation in the field of generalized holography in optics (Porter, 1969, 1970; Bojarski, 1983) and reciprocity theorems of the correlation type (de Hoop, 1988; Fokkema and van den Berg, 1993; de Hoop, 1995; Wapenaar *et al.*, 2004). More specifically, we show how the elastodynamic representation theorem can be used to time-reverse a wavefield in a volume and how, using the appropriate sets of Green's functions, the time-reversed wavefield can be computed at any point in the interior. Note that the elastodynamic Kirchhoff integral has previously been used as a boundary condition in reverse-time finite-difference migration (Mittet, 1994; Hokstad *et al.*, 1998) and in the finite-difference injection method proposed by Robertsson and Chapman (2000) to efficiently compute FD seismograms after model alterations. By applying a simple reciprocity argument it is shown how the elastodynamic Green's tensor between arbitrary points in a volume can be computed using only crosscorrelations and numerical integration once the Green's tensors from sources on the surrounding surface to these points are known. It is argued that illuminating a model from the outside leads to a flexible and efficient modeling algorithm.

The method is first illustrated using a simple acoustic model consisting of isotropic point scatterers embedded in a homogeneous background medium. This is followed by an example for a more complicated inhomogeneous elastic medium and a detailed discussion of computational aspects. The limits of using pseudo-noise sources on the boundary and exciting them simultaneously are also discussed. Finally, we speculate about reducing the number of sources on the surrounding surface as a way of approximate modeling that maintains high-order scattering and suggest possible synergies with methods of inversion for medium properties.

In the next section the interferometric modeling method will be derived from the elastodynamic representation theorem, closely following the physically intuitive reasoning of Derode *et al.* (2003). However, to fully understand the relation between time-reversal, interferometry and generalized holography it is useful to briefly review reciprocity first.

## 3.2 Reciprocity and the representation theorem

A reciprocity theorem relates two independent acoustic, electromagnetic or elastodynamic states that can occur in the same spatio-temporal domain, where a state simply means a combination of material parameters, field quantities, source distributions, boundary conditions and initial conditions that satisfy the relevant wave equation. In its most general form it relates a specific combination of field quantities from both states on a surface surrounding a volume, to differences in source distributions, medium parameters, boundary conditions or even flow velocities (in cases where the material is moving) throughout the volume (Fokkema and van den Berg, 1993; de Hoop, 1995; Wapenaar *et al.*, 2004).

Here we consider a special case of elastodynamic reciprocity where the medium in both states is identical and non-flowing. In that case, states (A) and (B) are simply characterized by the following wave equations (in the space-frequency domain):

$$\rho\omega^2 u_i^{(A)} + \partial_j \left( c_{ijkl} \partial_k u_l^{(A)} \right) = -f_i^{(A)}, \tag{3.1}$$

$$\rho\omega^2 u_i^{(B)} + \partial_j \left( c_{ijkl} \partial_k u_l^{(B)} \right) = -f_i^{(B)}, \tag{3.2}$$

where $u_i^{(A)}$ and $u_i^{(B)}$ denote the components of particle displacement for state (A) and (B), respectively, generated by the components of body force density $f_i^{(A)}$ and $f_i^{(B)}$ and where $c_{ijkl}(\mathbf{x})$ and $\rho(\mathbf{x})$ are the stiffness tensor and mass density, respectively, at location $\mathbf{x}$ in the medium. Note that Einstein's summation convention for repeated indices is used. The Betti-Rayleigh reciprocity theorem can be derived by multiplying the first equation by $u_i^{(B)}$ and the second by $u_i^{(A)}$, subtracting the results, integrating over a volume $V$ and using Gauss' theorem to convert volume integrals to surface integrals. This gives (Snieder, 2002)

$$\int_S \left\{ u_i^{(B)} n_j c_{ijkl} \partial_k u_l^{(A)} - n_j c_{ijkl} \partial_k u_l^{(B)} u_i^{(A)} \right\} \mathrm{d}S = - \int_V \left\{ f_i^{(A)} u_i^{(B)} - f_i^{(B)} u_i^{(A)} \right\} \mathrm{d}V. \tag{3.3}$$

Equation 3.3 is called a reciprocity theorem of the convolution type because the displacement and traction from the two states multiply each other (Bojarski, 1983; de Hoop, 1988). A Betti-Rayleigh reciprocity theorem of the correlation type can be derived by taking the complex conjugate of both sides of equation 3.1:

$$\rho\omega^2 u_i^{*(A)} + \partial_j \left( c_{ijkl} \partial_k u_l^{*(A)} \right) = -f_i^{*(A)}, \tag{3.4}$$

where a star $^*$ denotes complex conjugation, and following the same procedure that led up to equation 3.3. This gives

$$\int_S \left\{ u_i^{(B)} n_j c_{ijkl} \partial_k u_l^{*(A)} - n_j c_{ijkl} \partial_k u_l^{(B)} u_i^{*(A)} \right\} \mathrm{d}S = - \int_V \left\{ f_i^{*(A)} u_i^{(B)} - f_i^{(B)} u_i^{*(A)} \right\} \mathrm{d}V, \tag{3.5}$$

where now the quantities from both states occur in pairs that correspond to crosscorrelation in the time-domain. At this stage, however, the physical significance of a reciprocity theorem of the correlation type is not clear intuitively.

A representation integral can be derived from equation 3.3 by identifying one state with a mathematical or Green's state (i.e., a state where the source is a unidirectional point force and the resulting particle displacement is called the elastodynamic Green's function) and the other with a physical state that can be any wavefield resulting from an arbitrary source distribution. Thus, we arbitrarily choose state (B) to be the Green's state and take $\mathbf{f}^{(B)}$ a unit point force at location $\mathbf{x}'$ in the $n$ direction: $f_i^{(B)}(\mathbf{x}) = \delta_{in}\delta(\mathbf{x} - \mathbf{x}')$, where $\delta_{in}$ and $\delta(\mathbf{x})$ denote the Kronecker symbol and Dirac distribution, respectively, and the wavefield $u_i^{(B)}(\mathbf{x})$ becomes the Green tensor: $u_i^{(B)}(\mathbf{x}) = G_{in}(\mathbf{x}, \mathbf{x}')$. We leave state (A) unspecified. Inserting these expressions, carrying out the volume integral, dropping the superscripts for state (A) and making no assumptions about the boundary conditions we arrive at

$$\begin{aligned} u_n(\mathbf{x}') = & \int_V G_{in}(\mathbf{x}, \mathbf{x}') f_i(\mathbf{x}) \, \mathrm{d}V \\ + & \int_S \left\{ G_{in}(\mathbf{x}, \mathbf{x}') n_j c_{ijkl} \partial_k u_l(\mathbf{x}) - n_j c_{ijkl} \partial_k G_{ln}(\mathbf{x}, \mathbf{x}') u_i(\mathbf{x}) \right\} \, \mathrm{d}S. \end{aligned} \tag{3.6}$$

Finally, applying reciprocity to the Green's tensor and exchanging the coordinates $\mathbf{x} \leftrightarrow \mathbf{x}'$ and indices $i \leftrightarrow n$ we arrive at the elastodynamic representation theorem (Snieder, 2002)

$$\begin{aligned} u_i(\mathbf{x}) = & \int_V G_{in}(\mathbf{x}, \mathbf{x}') f_n(\mathbf{x}') \, \mathrm{d}V' \\ + & \int_S \left\{ G_{in}(\mathbf{x}, \mathbf{x}') n_j c_{njkl} \partial'_k u_l(\mathbf{x}') - n_j c_{njkl} \partial'_k G_{il}(\mathbf{x}, \mathbf{x}') u_n(\mathbf{x}') \right\} \, \mathrm{d}S', \end{aligned} \tag{3.7}$$

where $\partial'_k G_{il}(\mathbf{x}, \mathbf{x}')$ denotes the partial derivative of the Green's tensor in the $k$ direction with respect to primed coordinates and $\mathbf{n}$ denotes the normal to the boundary. Thus, the wavefield $u_i(\mathbf{x})$ can be computed everywhere inside the volume $V$ once the exciting force $f_n(\mathbf{x}')$ inside the volume and the displacement $u_n(\mathbf{x}')$ and the associated traction $n_j c_{ijkl} \partial'_k u_l(\mathbf{x}')$ on the surrounding surface $S$ are known.

## 3.3 Time-reversal using the representation theorem

To time-reverse a wavefield in a volume $V$, one possibility would be to reverse the particle velocity at every point inside the volume simultaneously. However, Cassereau and Fink (1992) noted that for open systems (i.e., with outgoing boundary conditions on at least part of the surrounding surface $S$) time-reversal can also be achieved by measuring the wavefield and its gradient on the enclosing surface, time-reversing those measurements and letting them act as a time-varying boundary condition on the surface $S$. Their approach directly follows from an application of Green's theorem (or the Kirchhoff-Helmholtz integral) and is easily extended to elastodynamic wave propagation using equation 3.7 derived above. Thus, to time-reverse any wavefield $u_i(\mathbf{x})$, due to an arbitrary source distribution $f_n(\mathbf{x})$, we substitute the complex conjugate of the wavefield (phase-conjugation being equivalent to time-reversal), its gradient and its sources into the elastodynamic representation theorem (equation 3.7). This gives

$$\begin{aligned} u_i^*(\mathbf{x}) = & \int_V G_{in}(\mathbf{x},\mathbf{x}') f_n^*(\mathbf{x}')\, \mathrm{d}V' \\ + & \int_S \{ G_{in}(\mathbf{x},\mathbf{x}') n_j c_{njkl} \partial_k' u_l^*(\mathbf{x}') - n_j c_{njkl} \partial_k' G_{il}(\mathbf{x},\mathbf{x}') u_n^*(\mathbf{x}') \}\, \mathrm{d}S'. \end{aligned} \tag{3.8}$$

Equation 3.8 can be used to compute the back-propagating wavefield (including all high-order interactions) at any location, not just at an original source location. It can also be confirmed that equation 3.8 is a valid representation for the time-reversed wavefield by substituting two forward Green's states into the equivalent Betti-Rayleigh reciprocity theorem of the correlation type (equation 3.5).

In order for the time-reversal to be complete, the energy converging at the original source locations should be absorbed. Thus, the volume integral in the right-hand side of equation 3.8 corresponds to the wavefield generated by a distribution of "elastic sinks" (de Rosny and Fink, 2002) which destructively interferes with the time-reversed wavefield that propagates through the foci.

Now, say that the wavefield $u_i(\mathbf{x})$ was also originally set up by a point force source excitation, but at location $\mathbf{x}''$ and in the $m$-direction (i.e., $f_i(\mathbf{x}) = \delta_{im}\delta(\mathbf{x}-$

$\mathbf{x}''$) and $u_i(\mathbf{x})$ is a Green's tensor: $u_i(\mathbf{x}) = G_{im}(\mathbf{x},\mathbf{x}'')$). Thus, if we compare equations 3.7 and 3.8, it is clear that effectively we are taking the unspecified state to be a time-reversed Green's state which satisfies the conjugated wave equation $\rho\omega^2 G^*_{im} + \partial_j\left(c_{ijkl}\partial_k G^*_{lm}\right) = -\delta_{im}\delta(\mathbf{x}-\mathbf{x}'')$ (cf. equation 3.4). Inserting these expressions in equation 3.8 and carrying out the volume integration gives

$$\begin{aligned} G^*_{im}(\mathbf{x},\mathbf{x}'') = G_{im}(\mathbf{x},\mathbf{x}'') \quad &+ \quad \int_S \{G_{in}(\mathbf{x},\mathbf{x}')n_j c_{njkl}\partial'_k G^*_{lm}(\mathbf{x}',\mathbf{x}'') \\ &- \quad n_j c_{njkl}\partial'_k G_{il}(\mathbf{x},\mathbf{x}')G^*_{nm}(\mathbf{x}',\mathbf{x}'')\}\ \mathrm{d}S'. \qquad (3.9) \end{aligned}$$

Equation 3.9 relates the time-advanced and time-retarded elastodynamic Green's functions. In the field of generalized holography in optics an equation of this type is often referred to as the Porter-Bojarski equation after the work by Porter (1969, 1970) and Bojarski (1983) who previously derived it for the scalar inhomogeneous Helmholtz wave equation and electric and magnetic vector wavefields.

Note that the time-retarded Green's function $G_{im}(\mathbf{x},\mathbf{x}'')$ in the right-hand side now corresponds to the wavefield generated by the point force elastic sink. In the following, the elastic sink will not be modeled – only the integral term in equation 3.9 will be calculated. Physically, this means that the converging wavefield will immediately start diverging again after focusing. Mathematically, the time-retarded Green's function has to be subtracted from both sides of equation 3.9 and the homogeneous Green's function, $G^h_{im}(\mathbf{x},\mathbf{x}'') \equiv G^*_{im}(\mathbf{x},\mathbf{x}'') - G_{im}(\mathbf{x},\mathbf{x}'')$, will be obtained: the time-reversed wavefield is a solution to the homogeneous wave equation (i.e., without a source term). The latter also follows immediately when subtracting the wave equations for the forward and time-reversed states (Oristaglio, 1989; Cassereau and Fink, 1992).

Equation 3.9 states that by measuring or computing the time-reversed wavefield at location $\mathbf{x}$ for a source originally at location $\mathbf{x}''$, the Green's function and its time-reverse between the source point $\mathbf{x}''$ and point $\mathbf{x}$ are observed. This agrees with other recent experimental and theoretical observations (Derode *et al.*, 2003; Wapenaar, 2004). Using reciprocity: $G_{ij}(\mathbf{x}',\mathbf{x}) = G_{ji}(\mathbf{x},\mathbf{x}')$, we can rewrite equation 3.9 so that it involves only sources on the boundary enclosing the medium:

$$
\begin{aligned}
G^*_{im}(\mathbf{x},\mathbf{x}'') - G_{im}(\mathbf{x},\mathbf{x}'') &= \int\limits_S \{G_{in}(\mathbf{x},\mathbf{x}') n_j c_{njkl} \partial'_k G^*_{ml}(\mathbf{x}'',\mathbf{x}') \\
&- n_j c_{njkl} \partial'_k G_{il}(\mathbf{x},\mathbf{x}') G^*_{mn}(\mathbf{x}'',\mathbf{x}')\} \, \mathrm{d}S'. \quad (3.10)
\end{aligned}
$$

Hence, Green's function between two points $\mathbf{x}$ and $\mathbf{x}''$ in a partially open elastic medium can be calculated once the Green's functions between the enclosing boundary and each of these points are known. In the following, we refer to equation 3.10 as the interferometric modeling equation.

## 3.4 Interferometric modeling

A highly efficient two-stage modeling strategy follows from equation 3.10: first, the Green's function terms $G_{im}(\mathbf{x},\mathbf{x}')$ and $n_j c_{ijkl} \partial'_k G_{lm}(\mathbf{x},\mathbf{x}')$ under the integral sign are calculated from boundary locations to internal points in a conventional forward modeling phase; in a second, intercorrelation phase, the integral is calculated requiring only crosscorrelations and numerical integration. Since the computational cost of typical forward modeling algorithms (e.g., FD) does not significantly depend on the number of receiver locations but mainly on the number of source locations, efficiency and flexibility are achieved because sources need only be placed around the bounding surface, not throughout the volume. The modeled wavefield should be stored for each of the boundary sources in as many points as possible throughout the medium. To calculate the components of the Green's tensor between two points the appropriate components of the displacement vector in the first point, due to deformation rate tensor type sources on the boundary, are crosscorrelated with the appropriate components of the Green's tensor in the second point, due to the point force sources from the same location on the boundary. The resulting crosscorrelation gathers are subtracted and numerically integrated over the boundary of source locations. Unprecedented flexibility follows from the fact that Green's functions can be calculated between all pairs of points that were defined up front and stored in the initial boundary source modeling phase. Thus, we calculate a partial modeling solution that is common to all Green's functions, then a bespoke component for each Green's function. A flowchart of the interferometric modeling method is given in Figure 3.1 and discussed in detail below for an acoustic isotropic point scattering example.

### 3.4.1 Boundary conditions

Note that because of the symmetry of the terms in the integrand in equation 3.10, no sources are required along the Earth's free surface, or any interface with homogeneous boundary conditions (e.g., with vanishing traction or vanishing particle displacement). Intuitively, this can be understood from a method of imaging argument: since such interfaces act as perfect mirrors, reflecting all energy back into the volume, an equivalent medium can be constructed which consists of the original medium combined with its mirror in the homogeneous boundary and the homogeneous boundary absent. Since the original boundary with source locations is mirrored as well, the new boundary does completely surround this hypothetical medium and therefore, the sources constitute a perfect time-reversal mirror. Note that when the free surface has topography, although the method of imaging argument breaks down, this property still holds.

According to equation 3.10 derivatives of the Green's function with respect to the source location on the boundary also have to be computed. As mentioned above, these terms correspond to the response due to special (deformation rate tensor type) sources on the boundary and seem to require additional modeling with such special sources before Green's functions can be computed using the new method. However, using reciprocity, these terms can also be interpreted as the traction measured on the enclosing boundary due to point forces at a particular point of interest (cf. equation 3.8). Crosscorrelation of components of particle displacement with components of traction ensures that waves that are incoming and outgoing at the surrounding boundary are correctly separated in the correlation process (Wapenaar and Haimé, 1990; Mittet, 1994).

When part of the surface surrounding the medium has outgoing boundary conditions (i.e., no energy crosses the surface as ingoing wave), the displacement and the corresponding traction are directly related (Holvik and Amundsen, 2005). In Appendix A, it is explained in detail how these properties can be exploited to avoid the need for additional direct modeling. When the boundary sources are embedded in a medium that is homogeneous along the source array, the components of the particle displacement in a particular point of interest gather are simply Fourier transformed into the frequency-wavenumber domain, matrix multiplied with an analytical expression and inverse transformed back to the space-time domain. This directly gives the corresponding components of traction. When the boundary is curved or the medium is inhomogeneous along the source array, spatially compact filter approximations can be designed to filter the data in the space-frequency domain using space-variant convolution. Such an approach is commonly used to decompose multi-component seismic data into up- and downgoing waves in the shot domain and is described in detail in, e.g., Robertsson and Curtis (2002); Robertsson and Kragh (2002); van Manen *et al.* (2004) and Amundsen *et al.* (2005).

Recently, Wapenaar *et al.* (2005) have shown, for the acoustic case, that when the surface surrounding the medium has outgoing boundary conditions, the two terms under the integral in the interferometric modeling equation (equation 3.10) are approximately equal, but have opposite sign. In addition, when the surrounding surface has large enough radius such that Fraunhofer far-field conditions (Fokkema and van den Berg, 1993) apply, only monopole sources are required to compute (time-integrated) Green's functions.

### 3.4.2 Special case: interferometric modeling of acoustic waves

The interferometric modeling formula for acoustic waves can be derived similarly, as discussed in detail in chapter 2 (van Manen *et al.*, 2005). Here, we simply restate the result, valid for partially open acoustic media (i.e., with outgoing, radiation or absorbing boundary conditions on at least part of the surrounding surface):

$$\begin{aligned} G^*(\mathbf{x},\mathbf{x}'') - G(\mathbf{x},\mathbf{x}'') &= \int_S \frac{1}{\rho(\mathbf{x}')} \left\{ n_j \partial_j' G(\mathbf{x},\mathbf{x}') G^*(\mathbf{x}'',\mathbf{x}') \right. \\ &- \left. G(\mathbf{x},\mathbf{x}') n_j \partial_j' G^*(\mathbf{x}'',\mathbf{x}') \right\} \mathrm{d}S', \qquad (3.11) \end{aligned}$$

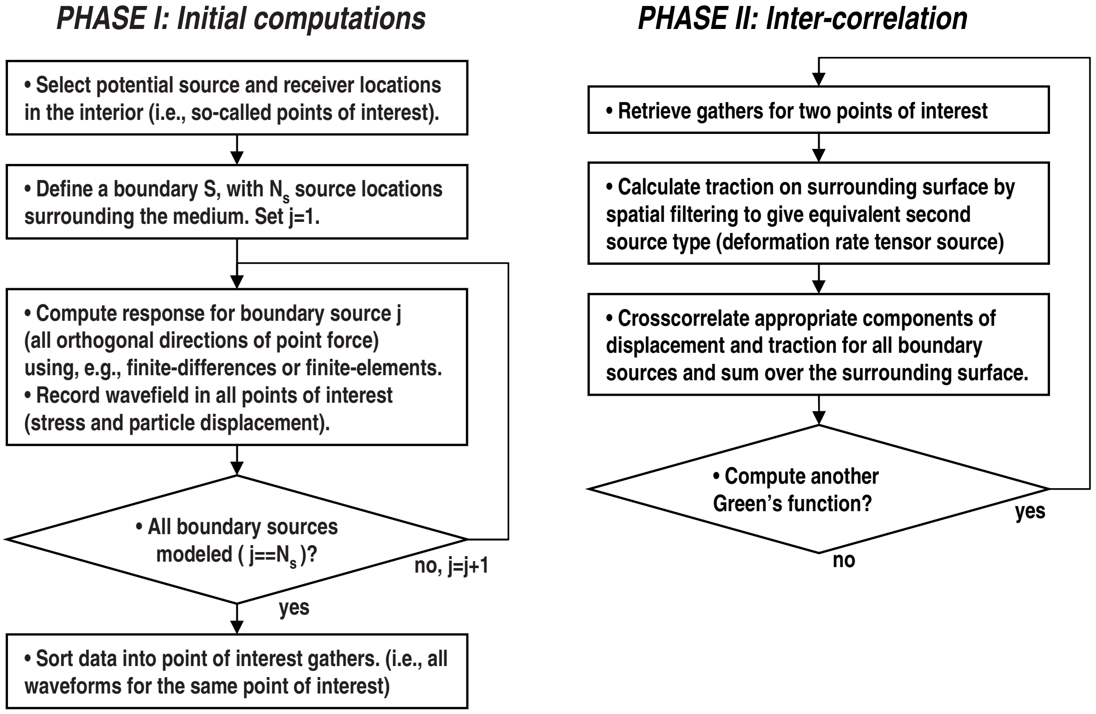

**Figure 3.1:** Flowchart of the proposed modeling method. The method consists of two main phases: an initial phase that creates a partial modeling solution that is common to all Green's functions (computed only once using a conventional forward modeling algorithm), followed by a second phase where desired Green's functions are computed from the partial modeling solution using only crosscorrelation and summation, without the need for additional modeling.

where $G(\mathbf{x}, \mathbf{x}'')$ denotes the Green's function for the pressure at location $\mathbf{x}$ due to a point source of volume injection at location $\mathbf{x}''$ and $n_j \partial'_j G(\mathbf{x}, \mathbf{x}')$ denotes the normal derivative of Green's function with respect to primed coordinates. Thus, the pressure Green's function $G(\mathbf{x}, \mathbf{x}'')$ between two points $\mathbf{x}$ and $\mathbf{x}''$ can be calculated once the Green's functions between the enclosing boundary and these points are known. Note that the terms $G(\mathbf{x}, \mathbf{x}')$ correspond to simple monopole sources on the surrounding surface whereas the terms $n_j \partial'_j G(\mathbf{x}, \mathbf{x}')$ correspond to dipole sources. This formula will be used in the next section to compute the Green's function between points in a 2D acoustic model with three isotropic point scatterers embedded in a homogeneous background medium.

## 3.5 Example I: 2D acoustic isotropic point scattering

The methodology described above is now explained in more detail using a simple 2D acoustic example. A more realistic elastic model, including strong heterogeneity and interfaces with homogeneous boundary conditions, is discussed in a later section. In Figure 3.2, three isotropic point-scatterers are shown, embedded in a homogeneous background medium of infinite extent (background velocity $v_0 = 750$ m/s). The point-scatterers are indicated by large black dots. The new method is used to model full waveform Green's functions between arbitrary source and receiver locations in the medium.

As indicated in the flowchart in Figure 3.1, in the first step a boundary enclosing the medium is defined and spanned by source locations. A large number of so-called "points of interest" are also specified. In Figure 3.2, every second boundary source location is marked with a star. The boundary sources should be spaced according to local Nyquist criteria. The grid of small points are the points where we may be interested in placing a source or receiver later. The number of points of interest should be chosen as large as possible, the only limitation being the waveform data storage capacity. In Figure 3.2, the triangles denote some particular points of interest that we will be looking at later.

In the second step of the initial phase, separate conventional forward modeling runs are carried out for each source on the boundary and the wavefield is stored at all points of interest. In this example, we have used a deterministic variant of Foldy's method (Foldy, 1945; Groenenboom and Snieder, 1995; Snieder and Scales, 1998) to compute the multiply scattered wavefield for each boundary source. This method naturally incorporates radiation boundary conditions. Note that we could have used any method that accurately models multiple scattering (e.g., FD). Our methodology is not restricted to any particular forward modeling method or code. Also, since multiplication with a complex conjugate in the frequency domain corresponds to crosscorrelation in the time domain, the method is not limited to a frequency-domain implementation. In the following, the examples are computed using the time-domain equivalent of equation 3.11.

In Figure 3.2, a snapshot of the early stages of the wavefield is shown for the

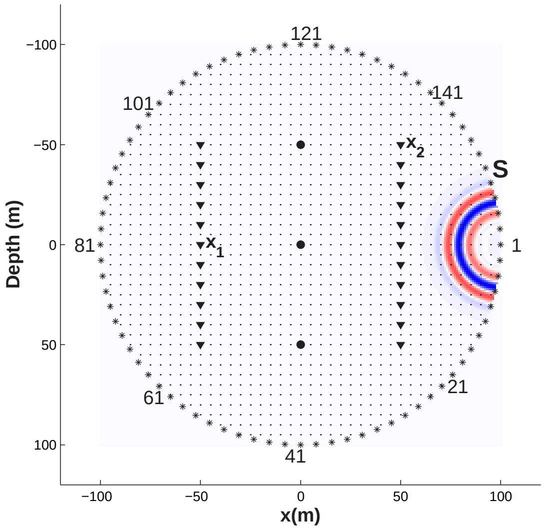

**Figure 3.2:** 2D acoustic model and snapshot of the first boundary source wavefield: Three isotropic point scatterers (large black dots) embedded in a homogeneous background medium $v_0 = 750$ m/s of infinite extent. Stars (*) mark every second source location on a surface enclosing the medium. Particular sources are numbered for reference with Figure 3.3a-f. Small dots (.) mark potential source and receiver locations (so-called points of interest) for Green's function intercorrelation. Triangles mark one of many cross-well source/receiver configurations that can be evaluated using the new method. In the initial phase, the wavefield is computed for all boundary sources separately and stored in all points of interest.

first source on the enclosing surface. Thus, in the second step, the interior of the model is systematically illuminated from the surrounding surface. During or after the simulations for all boundary sources, it is convenient to sort the data into so-called point-of-interest gathers comprising data from all boundary sources recorded at each point of interest. These constitute a common component of all Green's functions involving that point of interest.

In the second, intercorrelation phase, we may now calculate the Green's function between any pair of points that were defined beforehand by crosscorrelation and summation of boundary source recordings. In Figure 3.2, the triangles denote a subset of points that we could be interested in as part of, e.g., a cross-well survey design experiment.

In Figure 3.3, panels (a) and (d), the modeled wavefield due to each monopole source on the boundary is shown for two of the points of interest $\mathbf{x}_1$ and $\mathbf{x}_2$ (with coordinates [-50,0] and [50,-50], respectively). Note that, even though there are only three isotropic point scatterers, several multiply scattered waves can easily be identified. Also note the flat event at approximately $t = 0.2$ s. This is the incident wave from each boundary source, scattered isotropically in the direction of the two points of interest by the central scatterer (which is equidistant from each boundary source). In panels (b) and (c), the normal derivative with respect to the boundary has been computed by spatial filtering of the point of interest gathers (a) and (d), respectively, to simulate the response due to dipole sources on the boundary. This is possible since we have outgoing (i.e., absorbing or radiation) boundary conditions on the surrounding surface and hence the pressure and its gradient are directly related (see section 3.4.1 on boundary conditions and Appendix A for details). Calculation of the normal derivative with respect to the boundary source location is completely equivalent to measuring the response due to a dipole source so, alternatively, we could have modeled the required gradient using a second dipole source type. Typically, however, direct modeling would be computationally much more expensive.

Panels (e) and (f) show the trace-by-trace crosscorrelation of panels (a) and (c) and (b) and (d), respectively. Thus, they form the two terms in the integrand of the time-domain equivalent of equation 3.11. It is difficult to make a straightforward interpretation of the crosscorrelation gathers: although equation 3.11 predicts that the waveform resulting from summation of these crosscorrelations for all boundary sources will be anti-symmetric in time, panels (e) and (f) clearly are not. This is because, at this stage, we still have not carried through the Huygens' summation which provides the delicate (but stable!) constructive and destructive interference of the back-propagating wavefield. It can be seen, as predicted by Wapenaar *et al.* (2005) and discussed in the section on boundary conditions, that panels (e) and (f) are approximately equal, but have opposite sign. A more thorough analysis of the features of such crosscorrelation gathers is presented for the second example.

In the final step, crosscorrelation gathers (e) and (f) are weighted by $\rho^{-1}$, subtracted and numerically integrated (summed) over all source locations. The resulting intercorrelation Green's function and a directly computed reference solution are shown in Figure 3.3(g). The insets show particular events in the waveform in detail.

To further illustrate the new modeling method, the intercorrelation phase

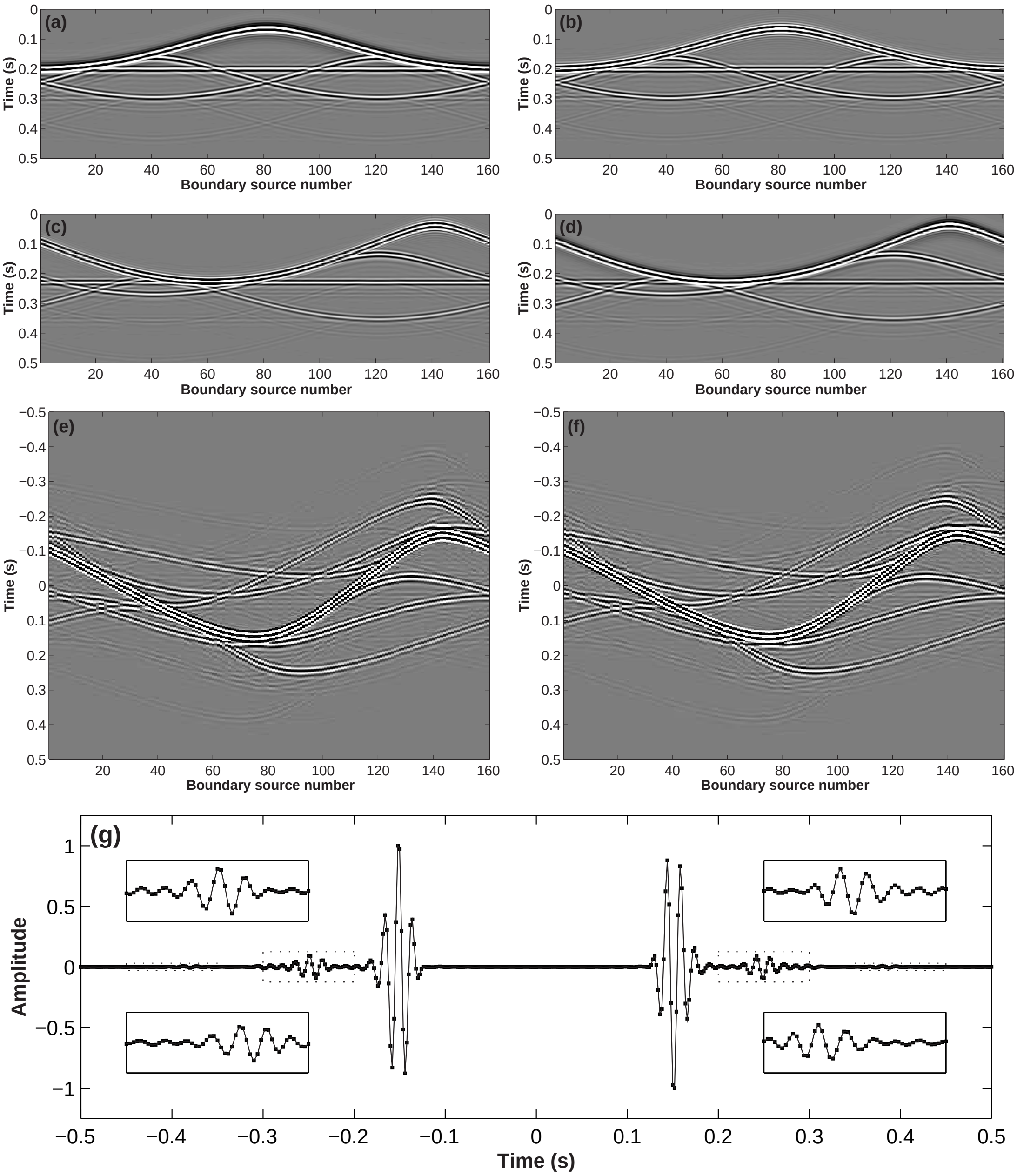

**Figure 3.3:** Modeled waveforms for all boundary sources in two points of interest and their crosscorrelation: **(a)** Monopole response in point $\mathbf{x}_1$ and **(b)** corresponding dipole response computed by spatial filtering (see text for details). **(c)** Dipole response in point $\mathbf{x}_2$ computed by spatial filtering and **(d)** corresponding monopole response. **(e)** Crosscorrelation of (a) and (c). **(f)** Crosscorrelation of (b) and (d). The difference between gathers (e) and (f), weighted by $\rho^{-1}$, forms the integrand of equation 3.11. **(g)** Intercorrelation Green's function (solid line) and a directly computed reference solution (squares). Insets show details of the signals in time-intervals bounded by dashed boxes. Note the anti-symmetry of the intercorrelation Green's function across $t = 0$ s, as predicted by equation 3.11.

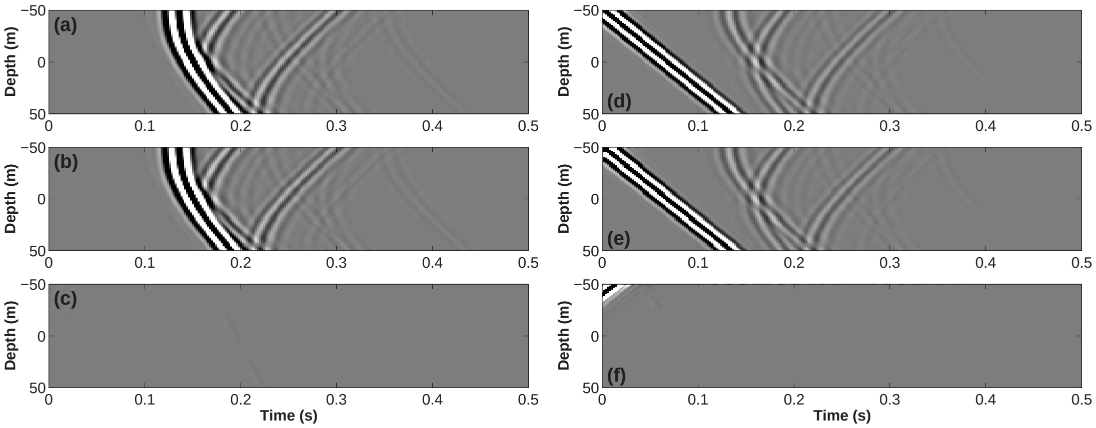

**Figure 3.4:** Comparison of Green's functions computed with the interferometric modeling method and a reference solution for the cross-well transmission and reflection setting in Figure 3.2 with a single source fixed at [-50,-50]. **(a)** Reference solution (transmission), **(b)** interferometric solution (transmission), and **(c)** difference ($\times 10$). **(d)** Reference solution (reflection), **(e)** interferometric solution (reflection), and **(f)** difference ($\times 10$). Note the mismatch in **(f)** for coincident source-receiver, this is because the interferometric solution is diffraction limited.

is now applied repeatedly to look-up Green's functions for a simple cross-well transmission and reflection seismic experiment shown in Figure 3.2 (source and receiver locations are indicated by triangles). Note that this does not require any additional conventional forward modeling but instead uses the same data modeled in the initial phase. Also note that we could consider a completely different well location, for any combination of point-of-interests (indicated by small dots in Figure 3.2) as long as they were defined beforehand and the wavefield was stored in those points during the initial modeling phase.

In Figure 3.4, panels (a) and (b), Green's functions computed using a conventional forward modeling method and the new method are shown, respectively. These Green's functions correspond to the transmission experiment shown in Figure 3.2 (source at [-50,-50], receivers distributed vertically from [50,50] to [50,-50] at 1 m spacing). Note that the amplitudes have been scaled up to show the weak, multiply scattered events. In panel (c), the difference between the Green's functions computed with the two methods is shown and the amplitude differences have been scaled up by a factor 10 to emphasize the match. Similarly, in panels (d),(e) and (f), Green's functions computed using the new method are compared to a reference solution for the reflection setting shown in Figure 3.2

(source at [-50,-50], receivers distributed vertically from [-50,50] to [-50,-50] at 1 m spacing). Again, amplitude differences have been scaled up by a factor 10. Note the mismatch in the Green's function for the direct wave close to the original source location. This error results from the missing acoustic sink and the bandlimited nature of the synthetics and agrees with the theory which predicts that the homogeneous Green's function will be retrieved.

## 3.6 Example II: 2D elastic Pluto model

In the second example we apply the method to an elastic model that is more relevant to the exploration seismic setting. In Figure 3.5, the compressional wave velocity in a 4.6 x 4.6 km region of the elastic Pluto model (Stoughton *et al.*, 2001) is shown. This model is often used to benchmark marine seismic imaging algorithms. A high velocity (4500 m/s) salt body on the right represents a common imaging challenge. In black, two particular points of interest, $\mathbf{x}_1$ and $\mathbf{x}_2$, are shown (offset 1 km). The solid line $S$ denotes the boundary with source locations. Every twentieth source location is marked by a square and selected source locations are numbered. These should be distributed with sufficient density such that the wavefields are not aliased after sorting the data into point-of-interest gathers. Outgoing (i.e., radiation or absorbing) boundary conditions (Clayton and Engquist, 1977) are applied right outside the surface enclosing the points of interest to truncate the computational domain.

Forward simulations were carried out for all of the source locations on the boundary using an elastic FD code (Robertsson *et al.*, 1994) and the waveforms stored at a large number of points distributed regularly throughout the model. Since we are dealing with the 2D elastodynamic wave equation, at least two forward simulations have to be carried out for each source location: one for each point force source in mutually orthogonal directions. Here, we also directly computed the response for the special deformation rate tensor type sources, but the equivalent traction data could also have been obtained by spatial filtering of the particle velocity point-of-interest gathers (see section 3.4.1 on boundary conditions and Appendix A for details). Since the FD modeling code is based on a velocity-stress formulation, in the following particle velocity Green's tensors

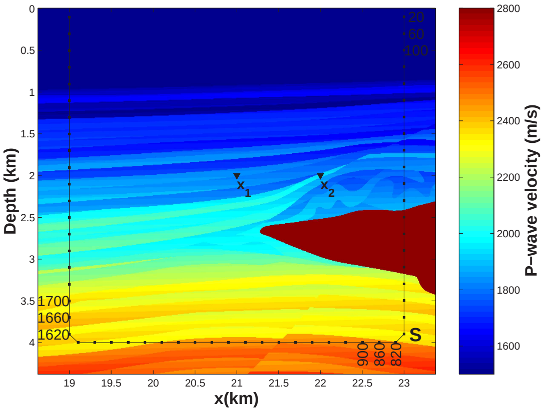

**Figure 3.5:** P-wave velocity of a 2D elastic marine seismic model. The color scale is clipped to display weak velocity contrasts (P-wave velocity of salt is 4500 m/s). The model is bounded by a free surface on top and by absorbing boundary conditions on the remaining sides. Every twentieth source on the surrounding surface $S$ is marked by a dot.

are used and the interferometric Green's functions computed after taking the time-derivative of the interferometric modeling equation (equation 3.10). Again, results are shown in the time domain.

Figure 3.6 shows the first 4 seconds of $\dot{g}_{11}(\mathbf{x}_1, \mathbf{x}')$ (i.e., the horizontal component of particle velocity in $\mathbf{x}_1$ due a horizontal point-force sources at location $\mathbf{x}'$ on the boundary) for all boundary sources. For reference, several sources on the boundary have been numbered in Figure 3.5 (the numbering increases clockwise from just below the free surface on the right). As explained in section 3.4.1, no sources are required along the free surface.

An interesting feature of the data, to which we will return later, occurs approximately between sources 200-475, and between sources 1800-2200. These sources are located in the near-surface of the sedimentary column, just beneath the water layer. The Pluto model includes many randomly positioned, near-surface scatterers, representing complex near-surface heterogeneity that is often observed in nature. Within these two source ranges it is clear that all coherent arrivals are followed by complicated codas that are superposed, resulting in a multiply-scattered signal that builds with time.

When all components of the Green's tensor and the equivalent traction data have been retrieved for the two points of interest $\mathbf{x}_1$ and $\mathbf{x}_2$, the gathers are crosscorrelated and summed according to the equivalent interferometric modeling equation for particle velocity. Note that even before numerical integration

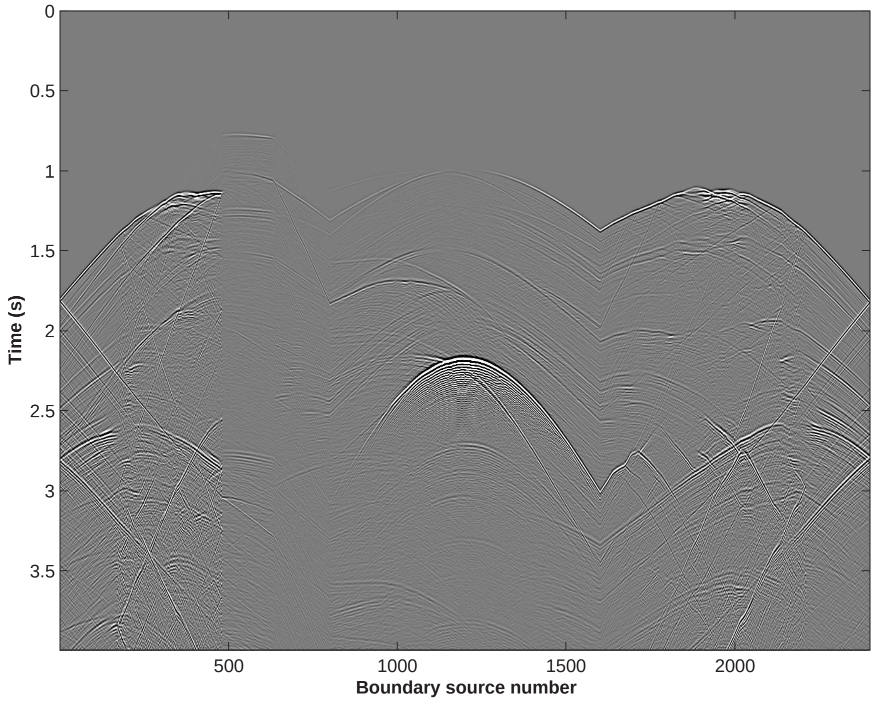

**Figure 3.6:** Point-of-interest gather for the left point in Figure 3.5 showing $\dot{g}_{11}(\mathbf{x}_1, \mathbf{x}')$, the horizontal component of particle velocity in the point of interest due to individual horizontal point force sources on the boundary. This is one of four required particle velocity Green's function gathers, computed in the initial phase, needed in the construction of all Green's functions involving that point.

this requires summation of crosscorrelation gathers since Einstein's summation convention for repeated indices is used.

Figure 3.7(a) shows the integrand of the interferometric modeling equation for particle velocity (in the time-domain) for the $\dot{g}_{11}(\mathbf{x}_2, \mathbf{x}_1)$ component of Green's tensor between the two points of interest $\mathbf{x}_1$ and $\mathbf{x}_2$. Note how the strongly scattered coda previously identified in Figure 3.6 affects both negative and positive time-lags in the crosscorrelation. In Figure 3.7(b), the Green's function $\dot{g}_{11}(\mathbf{x}_2, \mathbf{x}_1)$ resulting from direct summation of the crosscorrelation traces in panel (a) along the horizontal direction is shown. Note the emergence of the time-symmetry (across $t = 0$ s) from the non-symmetric crosscorrelations. The intercorrelation Green's function is time-symmetric instead of anti-symmetric, as predicted by equation 3.10, because particle velocity Green's functions were used in the example instead of particle displacement Green's functions.

In Figure 3.8, the four components of the particle velocity Green's tensor

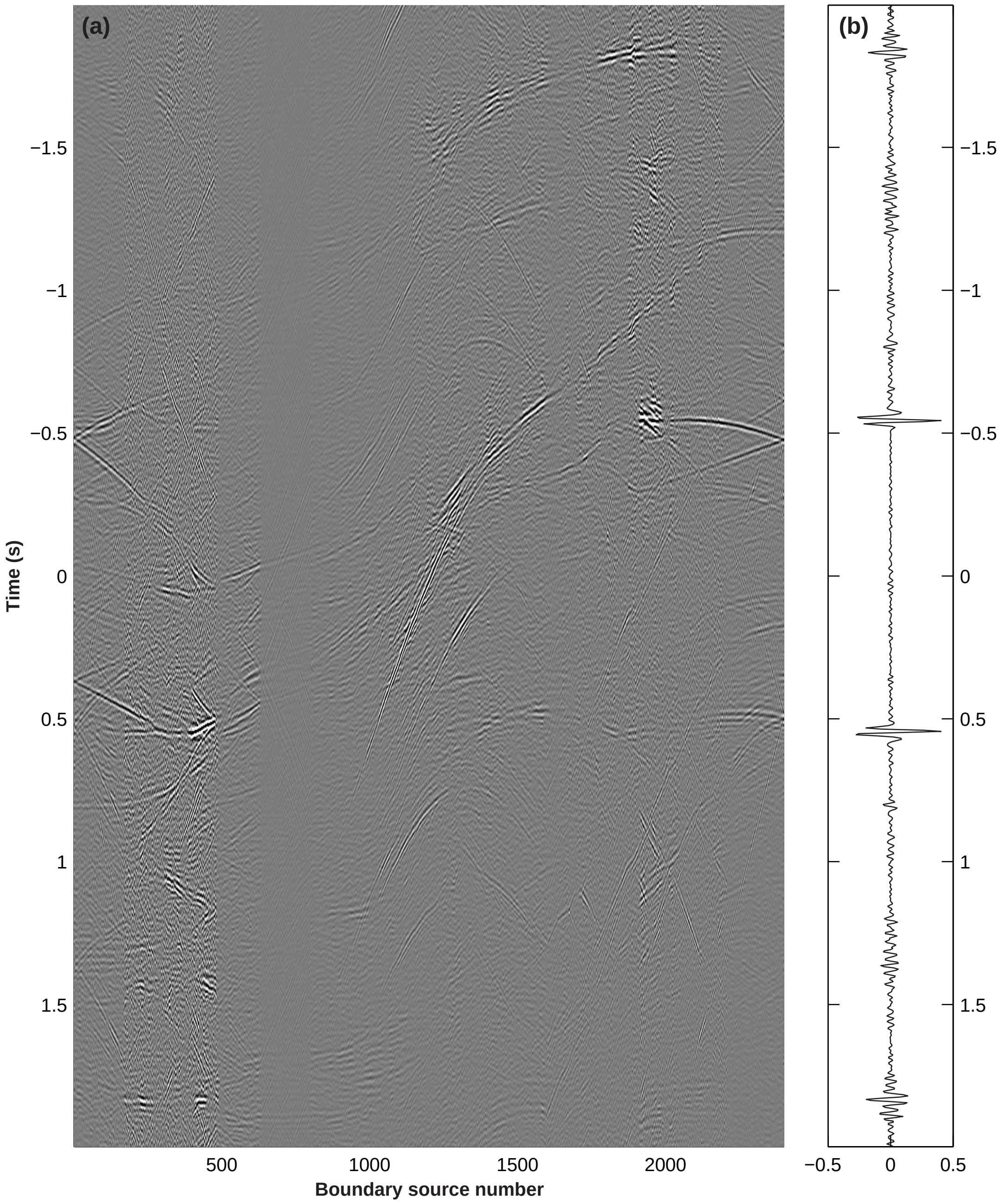

**Figure 3.7:** **(a)** Green's function intercorrelation gather (weighted) for the two points shown in Figure 3.5. The low correlation amplitude for boundary sources 620-800 corresponds to the shadow of the salt body. **(b)** Interferometric Green's function, $\dot{g}_{11}(\mathbf{x}_1, \mathbf{x}_2, -t) + \dot{g}_{11}(\mathbf{x}_1, \mathbf{x}_2, t)$, computed by direct summation of the crosscorrelations in panel (a) along the horizontal direction. Note the emergence of time-symmetry from the a-symmetric crosscorrelations. The reconstructed Green's function is symmetric, rather than anti-symmetric (as predicted by equation 3.10) because particle velocity Green's functions were used instead of particle displacement as in the theory.

computed using the new method (in blue) are compared to a directly computed reference solution (in green). The $\dot{g}_{11}(\mathbf{x}_2, \mathbf{x}_1)$ component in panel (a) was already shown in Figure 3.7(b). Note the good match between the directly computed reference solutions and the Green's functions computed using the new method, even at late times. The waveforms have been scaled and clipped to show the match in more detail. Some numerical noise at a-causal time-lags (i.e., before arrival of the direct wave) can clearly be seen. This noise is probably due to a slight undersampling of the shear wavefield as the computational parameters have been set rather tightly to minimize computational cost. Note how the different source radiation patterns are reproduced accurately by the new modeling method; panels (a) and (b) show more P-wave energy (e.g., the first significant arrival), which is consistent with a point force source in the horizontal direction and the second point of interest at the same depth level, whereas panels (c) and (d) show more S-wave energy because of the maximum in S-wave radiation in the horizontal direction by a point force excitation in the vertical direction.

## 3.7 Interpretation of the crosscorrelation gather

The time-series in Figure 3.7 bear little resemblance to the final Green's function in Figure 3.8. Equation 3.10 sums signals such as those in Figure 3.7 along the horizontal axis and hence relies on the delicate constructive and destructive interference of time-reversed waves back-propagating through the medium, recombining and undoing the scattering at every discontinuity to produce the Green's function. In Figure 3.7, each column represents the set of all waves propagating from point $\mathbf{x}_1$ to a particular location on the boundary, correlated with the Green's functions from a source at that location to $\mathbf{x}_2$. Thus, each column represents the Huygens' contribution of a particular boundary source to point $\mathbf{x}_2$, when the time-reversed wavefield is applied as a boundary condition. Some of the energy propagating from $\mathbf{x}_1$ to this boundary source may pass through $\mathbf{x}_2$ before being recorded and therefore has part of its path in common with waves emitted from $\mathbf{x}_2$ in the same direction. The traveltimes associated with such identical parts of the path are eliminated in the crosscorrelation and the remaining traveltime corresponds to an event in the Green's function from $\mathbf{x}_1$ to $\mathbf{x}_2$. Similarly,

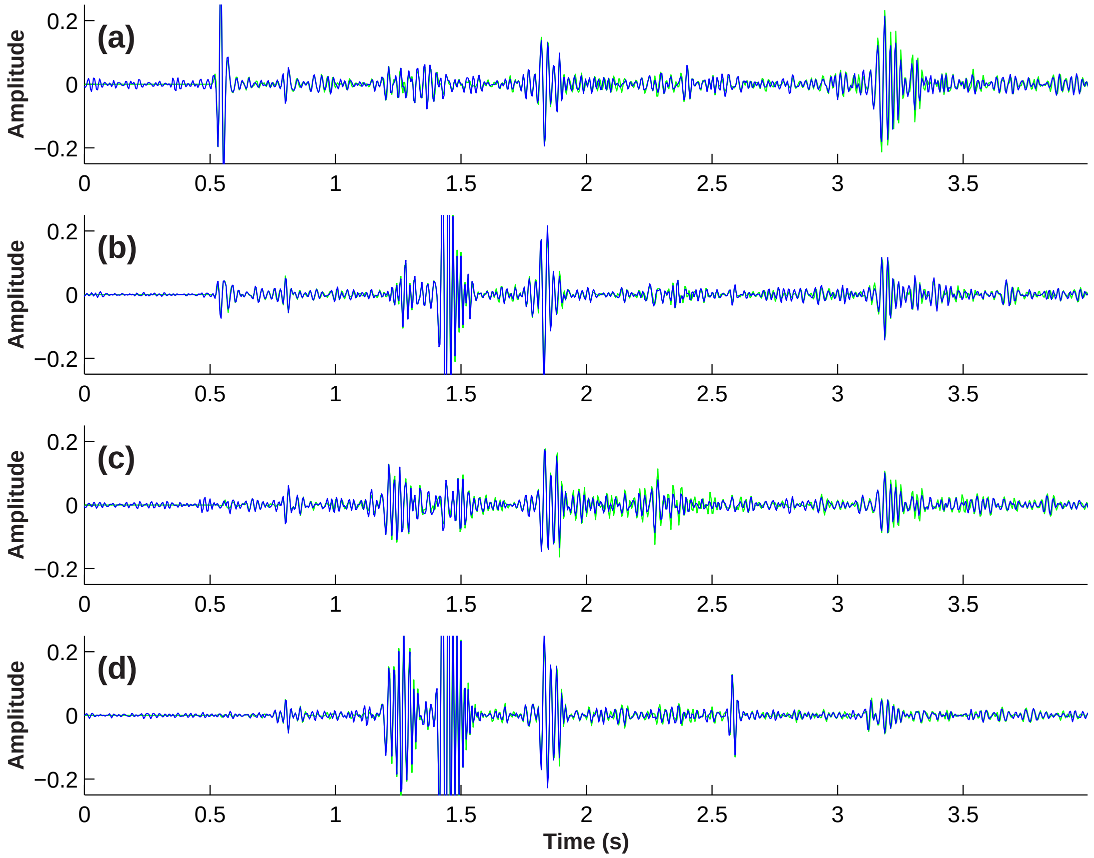

**Figure 3.8:** Components of the particle velocity Green's tensor $\dot{\mathbf{g}}(\mathbf{x}_2, \mathbf{x}_1)$ computed by summation of weighted intercorrelation gathers using the new method (blue) compared to reference solutions computed using a conventional FD method (green). **(a)** $\dot{g}_{11}(\mathbf{x}_2, \mathbf{x}_1)$, **(b)** $\dot{g}_{12}(\mathbf{x}_2, \mathbf{x}_1)$, **(c)** $\dot{g}_{21}(\mathbf{x}_2, \mathbf{x}_1)$, **(d)** $\dot{g}_{22}(\mathbf{x}_2, \mathbf{x}_1)$. For details see text.

some waves emitted from $\mathbf{x}_2$ may travel to the boundary source location via $\mathbf{x}_1$ and have a common section of path between $\mathbf{x}_1$ and the boundary source. Again traveltime on the common section will be eliminated and give rise to the same event in the Green's function from $\mathbf{x}_1$ to $\mathbf{x}_2$ but at negative times. Note that the directions involved with such overlapping paths for positive and negative times in general are not parallel since they are related to propagation of energy to the boundary through the background structure of the whole model (hence, one or other may not even exist for the same boundary source). Hence, waves at positive and negative times are reconstructed differently, even though the final Green's function constructed is identical. All energy in the crosscorrelations corresponding to waves that do not pass from $\mathbf{x}_1$ through $\mathbf{x}_2$ or vice-versa is eliminated by destructive interference through summation of the columns. This process of constructive and destructive interference is discussed in detail by Snieder (2004) and Snieder *et al.* (2006) using the method of stationary phase.

## 3.8 Computational aspects

We now discuss some computational aspects of the new modeling method. First, an estimate of the number of floating point operations (flops) is derived for both the initial and intercorrelation phase and compared to the cost of a sequence of conventional finite-difference computations. Then memory and storage implications are highlighted. In Table 3.1, parameters and variables mentioned in the computational discussion are summarized.

In the following, we ignore the cost of modeling the response to the second source type (i.e., the dipole or deformation rate tensor type sources). As explained in detail in Appendix A, the gradient (or traction) can be computed from the pressure (or particle velocity) through a spatial filtering procedure as applied to the point-of-interest gathers. The cost of this type of spatial filtering is typically insignificant compared to the FD simulations.

### 3.8.1 The cost of the initial phase and direct computation

Both direct computation and the initial phase of the new method, while consisting of a sequence of conventional finite-difference simulations have a computational

| parameter | description | |
|---|---|---|
| $a$ | number of operations to evaluate the discrete temporal and spatial derivatives | flops |
| $c$ | number of crosscorrelations for a single component of Green's tensor | dimensionless |
| $d$ | dimension of the modeling | dimensionless |
| $q$ | number of source components | dimensionless |
| $C_{FD}$ | cost of a single finite-difference run | flops |
| $C_{FFT}$ | cost of a combined FFT of two, padded real-valued traces | flops |
| $C_{GREEN}$ | cost of a single Green's function intercorrelation | flops |
| $C_{INIT}$ | cost of the initial phase in the new method | flops |
| $C_{CONV}$ | cost of a conventional sequence of FD simulations | flops |
| $C_{NEW}$ | cost using the new methodology to compute Green's functions | flops |
| $N_X$ | number of gridpoints along a typical dimension | dimensionless |
| $N_T$ | number of timesteps in the initial FD computations | dimensionless |
| $N_{T'}$ | number of timesteps in the intercorrelation phase | dimensionless |
| $N_S$ | number of source locations on the boundary | dimensionless |
| $N_{GF}$ | number of Green's function intercorrelations | dimensionless |
| $N_M$ | minimum number of conventional sources or receivers | dimensionless |

**Table 3.1:** Description of all parameters and variables mentioned in the computational discussion

cost that is directly proportional to the cost of a single FD simulation, $C_{FD}$. Typically, $C_{FD} \sim aN_T N_X^d$, where $N_T$ is the number of timesteps, $N_X$ the number of gridpoints in each of $d$ dimensions and $a$ is the number of flops required for the evaluation of the discrete temporal and spatial derivatives (e.g., $a = 22$ for a typical acoustic 2D FD code). When the data are computed directly, on the order of $N_M$ FD simulations are required (where $N_M$ is the minimum of the number of source and receiver locations considered in the modeling) whereas in the initial phase of the new method at least $N_S$ FD runs need to be carried out (where $N_S$ is the number of source locations on the boundary).

For the new modeling method, however, the simulation time $T$ has to be longer than in a conventional FD simulation: energy that is time-reversed has to be recorded on the surrounding surface (in the equivalent reciprocal experiment). In the following we assume that this doubles the simulation time for the new method. Defining a quantity $q$, where $q = 1$ for acoustic and $q = d$ for elastodynamic problems, and in the typical case that we are interested in all the components of the Green's tensor we find for direct computation and the initial phase of the new method:

$$
\begin{aligned}
C_{CONV} &= qN_M C_{FD}, && (3.12)\\
C_{INIT} &= 2qN_S C_{FD}. && (3.13)
\end{aligned}
$$

## 3.8.2 The cost of looking up a Green's function

Although the initial phase constitutes the bulk of the computations, the cost of "looking up" a Green's function cannot simply be ignored, especially when the number of Green's functions that are looked up is large. For each Green's function at least $N_S$ crosscorrelations and summations have to be computed and often more.

On the other hand, in the second, intercorrelation phase of the new method, the strict spatio-temporal sampling requirements of a typical full waveform modeling method [as governed by numerical accuracy and the Courant criterion (Robertsson *et al.*, 1994)] can be relaxed to Nyquist criteria. For a typical acoustic 2D finite-difference code with 2nd order accuracy in time and 4th order accuracy in space it can be shown that the ratio of the number of samples $N_T$ in the initial phase to the number of samples $N_{T'}$ in the intercorrelation phase can be as large as 30. Thus, the cost of looking up a Green's function in the intercorrelation phase is substantially reduced by abandoning the oversampling.

In addition, waveforms modeled in the initial phase are stored in the frequency domain in anticipation of the crosscorrelations in the intercorrelation phase. This avoids having to recompute the Fourier transform of point of interest gathers when computing several Green's functions involving the same point of interest. To avoid end effects, the traces are padded with $N_{T'}$ zeros. Transforming a waveform to the frequency domain using an FFT therefore takes on the order of

$$C_{FFT} \approx N_{T'} \log_2(N_{T'} + 1) \tag{3.14}$$

flops, where $N_{T'}$ is twice the number of time samples in the desired (one-sided) final seismogram and we have made use of the fact that the FFT of two real traces can be computed at once.

The number of crosscorrelations, $c$, that need to be computed for a boundary source location depends on the the type of wave equation (i.e., scalar or vector) and the spatial dimensionality of the problem, $d$. For an acoustic problem there is only a single, scalar quantity and this does not increase with the spatial dimensionality. Therefore, $c = 2$, the number of terms in the integrand in equation 3.11. For an elastic problem, the implicit Einstein summation (for repeated indices) in equation 3.10 and the two terms in the integrand lead to $c = 2d$. The acoustic and elastic cases can be written in the same form using the quantity $q$ defined above: $c = 2q$. Complex multiplication of the positive frequencies for all source locations on the boundary and the $c$ crosscorrelations takes $6cN_S N_{T'}$ operations. Complex addition of the $c$ crosscorrelation gathers takes $2(c-1)N_S N_{T'}$ operations. Multiplying the crosscorrelation gathers with the (varying) weighting factor along the boundary takes $2N_S N_{T'}$ operations. Summing the weighted crosscorrelations for all source locations takes $2(N_S - 1)N_{T'}$ flops. Thus, the total number of flops required for the intercorrelation of a single component of Green's tensor is approximately

$$C_{GREEN} \approx (8c + 2)N_S N_{T'} + C_{FFT}, \tag{3.15}$$

where $C_{FFT}$ relates to the final inverse FFT. Note that $C_{FFT}$ can typically be neglected since in most cases of interest $(8c+2)N_S \gg \log_2(N_{T'}+1)$. In Table 3.2, $c$ is computed for two- and three-dimensional acoustic and elastic modeling.

### 3.8.3 Comparison of direct computation and the new method

To make an exact comparison between direct computation and the new method means that one has already chosen a particular source and receiver geometry. In a lot of cases, such as survey evaluation and design and full waveform seismic inversion, this is simply not possible and therefore the new method enables the full potential of such applications. In other applications, such as straightforward simulation of synthetic data, one intrinsically limits the uses of the data by deciding on a geometry upfront (e.g, by choosing the source or receiver depth(s) when generating a towed marine synthetic seismic data set). Nevertheless, it is instructive to assess the relative efficiency of the two methods when a given set of Green's functions has to be computed.

Assuming that we are interested in all $d^2$ components of the Green's tensor and that $N_{GF}$ Green's functions are looked-up, the cost of the new method compared to a sequence of conventional finite-difference simulations follows directly from equations 3.12, 3.13 and 3.15:

$$C_{CONV} = qN_M C_{FD}, \tag{3.16}$$

$$C_{NEW} = 2qN_S C_{FD} + q^2 N_{GF} C_{GREEN}. \tag{3.17}$$

From these equations it is not immediately clear that the new method is always more efficient than direct computation. For instance, in the case, 1, that one is interested in only Green's functions between a single point and a set of other points, the initial computational burden clearly makes the new method inefficient. In the other extreme case, 2, where one is interested in all combinations of Green's functions between a large number of points, $N_M$, the new method is also less efficient because the number of Green's functions to be looked up, $N_{GF}$, is proportional to the square of $N_M$. In such a case, equations 3.16 and 3.17 are a straight line through zero and a vertically offset parabola, as a function of $N_M$,

| | Acoustic | | Elastic | |
|---|---|---|---|---|
| parameter | 2D | 3D | 2D | 3D |
| $a$ | 22 | 32 | 50 | 102 |
| $q$ | 1 | 1 | $d(=2)$ | $d(=3)$ |
| $c(=2q)$ | 2 | 2 | 4 | 6 |

**Table 3.2:** Values for the different parameters in 2D and 3D acoustic and elastic modeling

respectively and, at best, there may be a region where the new method is more computationally efficient.

On the other hand, in applications, 3, where Green's functions between a large number of points interior to a medium are desired, but where there are no common source or receiver points, the upfront value of the new method is obvious. In such a case, a separate conventional FD simulation is required for each Green's tensor and hence, $N_{GF} = N_M$. In this case, equations 3.16 and 3.17 are a straight line through zero and a vertically offset straight line, as a function of $N_M$, respectively and the new method becomes more efficient beyond the intersection point of the two lines. No other existing method offers full waveforms at comparable computational cost.

The three cases described above (denoted 1,2,3) are illustrated in figure 3.9 for a 2D acoustic finite-difference code. The chosen parameters are: $N_T = N_X = 1000$, $d = 2$, $a = 22$, $N_S = 1000$ (number of sources on the boundary), $q = 1$, and $N_{T'} = N_T/30$ for a range of number of Green's functions to be looked-up $N_{GF}$. The computational cost of conventional FD modeling (in flops) is shown in blue. Note that both cases 1 and 3 for interferometric FD modeling, in red, are governed by the same equations. However, case 1 relates to the unefficient application where few Green's functions are computed for single source and many receivers (the left part of the figure), while case 3 relates to the efficient application where many Green's functions are computed but where there are no common source or receiver points. In Green the cost of interferometric FD modeling is shown when Green's functions between all pairs of points are required. It can be seen that there is a region where the interferometric modeling method is more efficient.

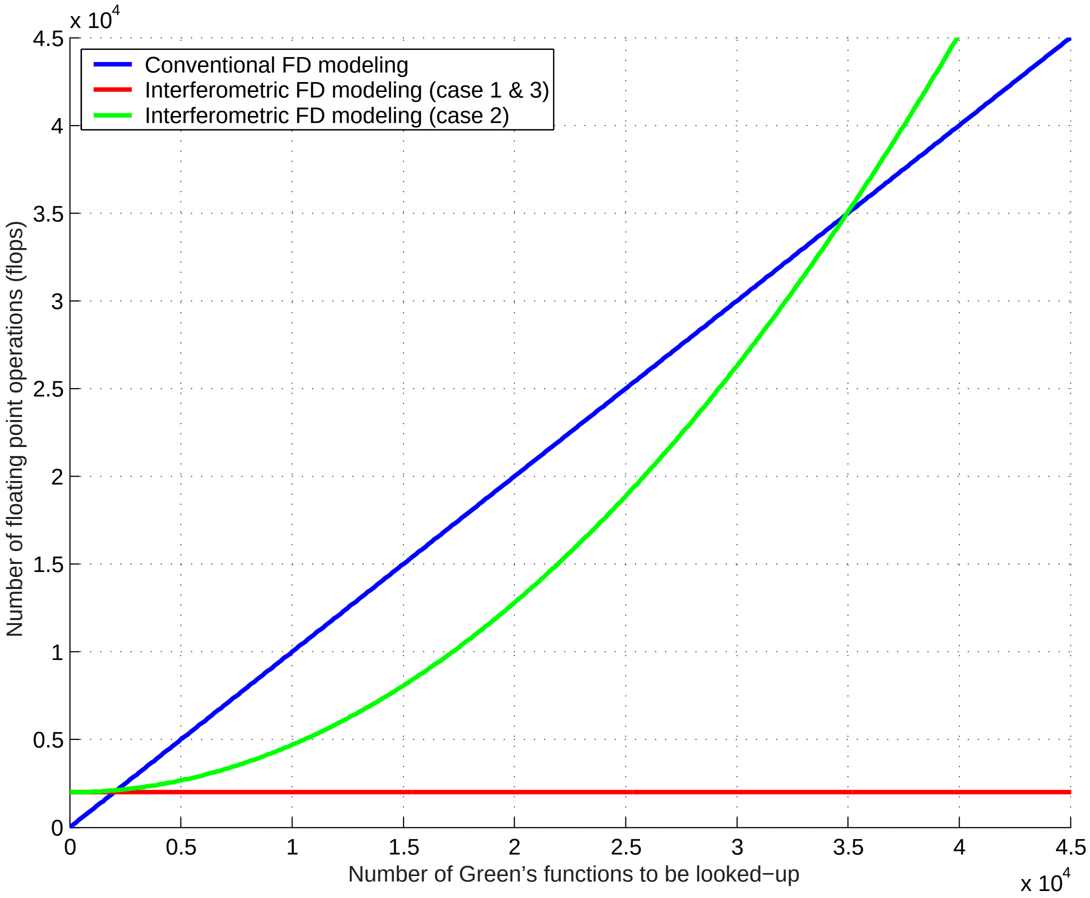

**Figure 3.9:** Computational cost of conventional versus interferometric modeling for a 2D acoustic FD code. The cost of conventional FD modeling is shown in blue. The cost of interferometric FD modeling for scenarios 1 and 3 (described in the main text) is shown in red, and the cost of interferometric FD modeling for scenario 2 is shown in green. Note that the interferometric modeling method is not always more efficient then conventional FD modeling.

### 3.8.4 Memory and storage

Assuming that a standard isotropic elastic FD method is used (e.g., not relying on domain decomposition), the amount of run-time memory required for storage of the $(d/2)(d+3)$ field quantities (e.g., $v_i$ and $\sigma_{ij}$) and 3 medium parameters (e.g., $\rho$, $\lambda$ and $\mu$) is at least $4[(d/2)(d+3)+3]N_X^d$ bytes (for a heterogeneous medium and calculations carried out in single precision). We note that for a medium size of $N_X = 1000$, a 3D elastic problem will require on the order of 45 Gbytes of primary memory. This number grows considerably for even more complex media (e.g., anisotropic), and the computations therefore typically rely on large shared memory machines or heavily parallelized algorithms running on clusters with high-performance connections. Using our methodology we compute a table of all point of interest gathers using high-end computational resources. The computations in the intercorrelation phase, on the other hand, are performed on much smaller machines as they require a substantially smaller amount of primary memory and because they require only a subset of the intercorrelation table to be exported. We have shown how the point of interest gathers with Green's functions constitute a common component of all Green's functions in the medium through equation 3.10.

## 3.9 Simultaneous sources: limits of encoding and decoding

We also investigated exciting the boundary sources simultaneously by encoding the source signals using pseudo-noise sequences (Fan and Darnell, 2003) and with simultaneous sources distributed randomly in the medium (Derode *et al.*, 2003) as two alternative ways to reduce the number of sources, and hence, the computational cost of the initial forward modeling phase. Such approaches have been investigated in attempts to speed-up conventional finite-difference simulations, although in surprisingly few published studies. Recent experimental evidence in passive imaging, however, using techniques based on interferometry and time-reversal, seems to suggest that such an approach would be highly feasible for the new modeling method. For instance, Wapenaar and Fokkema (2004) and Derode *et al.* (2003) show that, when the sources surrounding and inside the medium consist of uncorrelated noise sequences, their autocorrelation tends to a delta function and terms involving crosscorrelations between the different noise sequences can be ignored. However, it is well known in the field of communications analysis that Welch's bound (Welch, 1974) poses a fundamental limit to the quality of separation of such pseudo-noise sequences of a given length, when emitted simultaneously. In Appendix B it is shown that, when making no assumptions about the Green's function, the signal-to-interference (from the unwanted crosscorrelations between the encoding sequences) ratio in the final modeled seismogram is proportional to $\sim \sqrt{N}$, where $N$ is the length of the sequences. Thus, the signal-to-interference ratio only improves as the square-root of the sequence length. Note that the number of sequences required, the so-called family size $M$ (equal to the number of boundary sources: $M = N_S$), does not influence the signal-to-interference ratio. A similar expression was recently derived by Snieder (2004) using a statistical approach to explain the emergence of the ballistic (direct wave) Green's function through an ensemble of scatterers with uncorrelated positions.

Although in principle, and in real-life experiments, it is possible to reduce such interference by time/event averaging, where data are "modeled" for free and all we have to do is listen longer (Snieder, 2004), in synthetic modeling of Green's functions it is exactly the modeling itself that is expensive and therefore the use of pseudo-noise sequences for the purpose of interferometric, simultaneous source FD modeling is probably limited. In all explored cases, the limits of separation caused relatively high noise levels compared to the equivalent FD effort using the direct method described above.

## 3.10 Discussion and conclusion

Whereas traditional approximate modeling methods typically impose restrictions with respect to the degree of heterogeneity in the medium of propagation or neglect high-order scattering, the new time-reversal modeling methodology allows us instead to compromise on noise level while maintaining high-order scattering and full heterogeneity in the medium. Recent experimental and theoretical work indicates that time-reversed imaging is robust with respect to perturbations in the boundary conditions (Snieder and Scales, 1998; Derode *et al.*, 2003). For cases where the wave propagation is heavily dominated by multiple scattering even a single source may be sufficient to excite all wavenumbers in the model, and hence to refocus essential parts of a time-reversed signal (Draeger and Fink, 1999). Even when not all wavenumbers are excited by a single source, such as in the examples above, it may be possible to substantially reduce the number of sources and still recover essential parts of the signal. In chapter 2 (van Manen *et al.*, 2005) we showed that even for as few as one sixteenth of the original number of sources they were able to reproduce amplitude and phase of an arrival of interest fairly accurately, but with an increased noise level. Clearly, the required number of sources will depend on the application. For many applications, the possibility to trade-off signal-to-noise ratio to CPU time without compromising on medium complexity or high-order scattering will be another attractive property of the new method.

We anticipate that the new methodology will also have a significant impact on inversion. For example, Oristaglio (1989) has shown that the Porter-Bojarski equation (similar to equation 3.10) forms the basis for an inverse scattering formula that uses all the data. He proved that a three step imaging procedure, consisting of backpropagation of receiver and source arrays followed by temporal filtering, gives the scattering potential within the Born approximation. His formula relies on complete illumination of a (three-dimensional) scattering object from a surface surrounding the object, as our modeling method does. Interestingly, the method provides exactly those Green's functions required for direct evaluation of higher-order terms in the Neumann series solution to multiple scattering. Consider perturbing an inhomogeneous background model (e.g., by adding multiple isotropic point scatterers). In such a case, computation of the Green's functions in the background medium may not be trivial and the new method provides such Green's functions efficiently and flexibly. Note that we do not even have to specify beforehand which regions of the model we want to perturb or add the scatterers to. Rose (2002) argues that focusing, combined with time-reversal is the physical basis of exact inverse scattering and derives the Newton-Marchenko equation from these two principles.

The new method also provides a flexible way to compute spatial derivatives of the intercorrelation Green's functions with respect to both source and receiver coordinates for any region in the model, provided the points of interest are spaced closely enough in the initial modeling phase. This makes it straightforward to consider other types of sources and receivers, such as pure P- and S-wave sources and receivers (see e.g. Wapenaar and Haimé, 1990; Robertsson and Curtis, 2002; Wapenaar *et al.*, 2004). Alternatively, in cases the medium is relatively well known, but where the objective is to track some kind of non-stationary source or receiver within the volume, computationally cheap spatial derivatives may also be a significant advantage.

Thus, we have shown how the elastodynamic representation theorem can be used to time-reverse a wavefield in a volume, and how, using a second set of Green's functions, the time-reversed wavefield may be computed at any point in the interior. We emphasized the relationship between time-reversal, interferometry, holography and reciprocity theorems of the correlation type. By invoking reciprocity, we arrived at an expression that is suitable for interferometric modeling of wave propagation and suggested an efficient two-stage modeling scheme whereby in an initial phase the model is illuminated from the outside using a sequence of conventional forward modeling runs and in a second phase Green's functions between arbitrary points in the volume can be computed using only crosscorrelations and summation (numerical integration). The method was illustrated in detail using an acoustic isotropic point scattering example and applied to a region of the elastic Pluto model. A physical description of the crosscorrelation gathers was given and the computational aspects discussed. The limits of encoding and decoding were also discussed. Finally, implications for modeling and inversion were suggested. We expect that the new method may significantly change the way we approach modeling and inversion of the wave equation in future.

# Chapter 4

# An exact boundary condition for interior scattering problems involving arbitrarily large model perturbations

An exact boundary condition for scattering problems involving arbitrarily large model perturbations in generally inhomogeneous media (e.g., acoustic, elastic, electro-magnetic) is presented. The boundary condition decouples the wave propagation on a perturbed domain while maintaining all interactions with the background model, thus eliminating the need to regenerate the response on the full model. The method, which is explicit, relies on a Kirchhoff-integral extrapolation approach to update the boundary condition at every time-step of, for example, a finite-difference calculation. The Green's functions required for extrapolation through the background model are computed efficiently using interferometry.

## 4.1 Introduction

Many problems involving wave scattering such as waveform inversion, experimental and industrial design, and non-destructive testing, require evaluation of the wavefield response for a suite of closely related models. While model changes may be restricted to small subvolumes, realistic strong multiple scattering often rules out a Born approximation, making repeated full waveform simulations for the entire model a necessity. We show that this paradigm may be broken by combining a Kirchhoff-integral extrapolation approach with recent advances in interferometry, resulting in an exact boundary condition for arbitrarily large model perturbations.

Non-reflecting boundary conditions based on the Kirchhoff integral were first proposed by Ting and Miksis (1986). By extrapolating the wavefield from an artificial surface surrounding a scatterer to the boundary of the computational domain, exact boundary conditions are found, such that the computational domain can be truncated without generating spurious reflections. The boundary condition was implemented and tested by Givoli and Cohen (1995). Teng (2003), exploring the limiting case where the extrapolation surface coincides with the boundary condition, obtained a boundary integral equation that can be solved in conjunction with the finite-difference scheme on the subgrid. However, in each case, only exterior wave problems were considered, i.e., with non-reflecting boundary conditions outside the scatterer.

On the other hand, in locally perturbed scattering problems the boundary condition should treat both incoming and outgoing waves correctly. Schuster (1985) proposed a hybrid boundary integral equation + Born series modeling scheme in which he perturbed a system of surface boundary integral equations for a multibody scattering problem into a part corresponding to the long-range interactions of the perturbation with itself, which could be relatively easily inverted, and a part between the perturbations, which he solved using a Born series. However, he only homogeneous background models and interiors.

Robertsson and Chapman (2000) describe a method to “inject” on a perturbed interior computational domain a wavefield recorded during an initial simulation on the full domain. The injection thus drives the computation on the perturbed interior domain. Their boundary condition accounts for all orders of interactions of the wavefield on the subvolume and for the first-order interaction between the subvolume and the unperturbed background model, both of which can be arbitrarily inhomogeneous. The only part of the wavefield missing is that resulting from those interactions of the altered wavefield with the unaltered model outside the subvolume which propagates back into the subvolume and interacts with the perturbations again: so-called, high-order, long-range interactions.

The exact boundary condition presented here combines elements from the “injection” and Kirchhoff extrapolation approaches: it uses an incident wavefield as a boundary condition to drive the simulation on a subvolume, but accurately models all high-order, long-range interactions between the perturbed region and the background medium by continuously updating the boundary condition through the evaluation of a Kirchhoff convolution integral involving full waveform Green’s functions. The Green’s functions required for extrapolation through the background model can be computed efficiently and flexibly using interferometry: by illuminating the model from a surrounding surface with a sequence of conventional forward modeling runs, exact Green’s functions between any pair of points can be computed using only crosscorrelations and summations (chapters 2 and 3).

Thus, computationally, the new method differs from the original “injection” approach by Robertsson and Chapman (2000) in at least two important ways: (1) no additional absorbing boundary conditions are required outside the injection surface as the new boundary condition *does* truncate the perturbed computational domain, and, (2) the boundary condition is updated during every timestep of the finite-difference computation to account for the higher-order long-range interactions whereas the original injection approach was not. It generalises the non-reflecting boundary conditions based on the Kirchhoff integral to arbitrary exterior scattering configurations.

Note that even though we propose to use *crosscorrelation* based methods (interferometry) to compute the full waveform Green’s function required for extrapolation through the background model, the method is still based on evaluating a discrete, causal *convolution* integral. Therefore, the link with time-reversal that was strong in chapters 2 and 3 is much weaker here. Nevertheless, the efficiency and flexibility resulting from the use of interferometry to compute the Green’s functions for the background model are crucial in making the proposed exact boundary condition practical.

## 4.2 Scattering by an arbitrary inhomogeneous object

It is well known (Fokkema and van den Berg, 1993; de Hoop, 1995) how the wavefield scattered by an object with material properties $\rho^s(\mathbf{x})$, $\kappa^s(\mathbf{x})$, different from the inhomogeneous medium within which it is embedded, with properties $\rho(\mathbf{x})$, $\kappa(\mathbf{x})$, originates from the contrast in the material properties [note that $\kappa(\mathbf{x}) = K^{-1}(\mathbf{x})$]. Defining the scattered wavefield $\{p^{sct}, v_k^{sct}\}$ as the difference between the total wavefield $\{p, v_k\}$, propagating in the perturbed model, and the incident wavefield $\{p^{inc}, v_k^{inc}\}$, propagating in the background model, it is straightforward to show that the scattered wavefield quantities satisfy (figure 4.1):

$$\partial_k p^{sct} + \rho\partial_t v_k^{sct} = (\rho - \rho^s)\partial_t v_k \quad \mathbf{x} \in D_{sct}, \tag{4.1}$$

$$\partial_k v_k^{sct} + \kappa\partial_t p^{sct} = (\kappa - \kappa^s)\partial_t p \quad \mathbf{x} \in D_{sct}. \tag{4.2}$$

Equations 4.1 and 4.2, show how the scattered wavefield originates from body force sources, $(\rho - \rho^s)\partial_t v_k$, and volume injection sources, $(\kappa - \kappa^s)\partial_t p$, acting in the *background* medium. However, the simplicity of equations 4.1 and 4.2 is deceptive since the source terms on the right-hand side depend on the unknown total wavefield quantities $p$ and $v_k$ inside $D_{sct}$. Nevertheless, if the scattered wavefield is known on a surface surrounding the scatterer, S, equations 4.1 and 4.2 constitute an acoustic radiation problem and we have the following representation for the scattered pressure at any point, $\mathbf{x}^R$, outside $D_{sct}$:

$$\begin{aligned} p^{sct}(\mathbf{x}^R, \tau) &= \int_0^\tau \int_S \big[G^q(\mathbf{x}^R|\mathbf{x}, \tau - t)v_k^{sct}(\mathbf{x}, t) \\ &+ \Gamma_k^q(\mathbf{x}^R|\mathbf{x}, \tau - t)p^{sct}(\mathbf{x}, t)\big]\, n_k \mathrm{dSdt}, \end{aligned} \tag{4.3}$$

where $G^q(\mathbf{x}^R|\mathbf{x}, \tau - t)$ and $\Gamma_k^q(\mathbf{x}^R|\mathbf{x}, \tau - t)$ are the Green's functions for pressure due to point sources of volume injection and body force, respectively, in the *background* medium. Note that even though equation 4.3 contains the scattered wavefield quantities in the right-hand side, this equation is also valid for the total wavefield quantities as it can be shown that the corresponding integral over the incident wavefield quantities vanishes. This is because the incident wavefield,

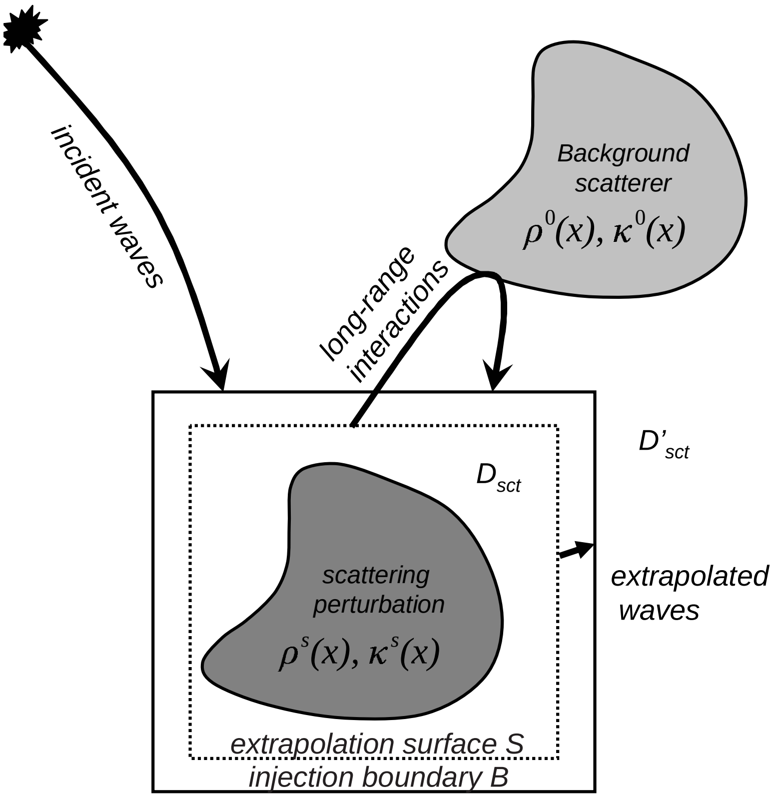

**Figure 4.1:** Definition of the extrapolation surface and injection boundary. Note that three events will contribute to the boundary condition: the incident wavefield propagating in the background medium, the extrapolated waves that are outgoing at the boundary (these will complement the corresponding waves propagating on the subgrid), and the extrapolated waves that are incoming at the boundary and which radiate onto the subgrid, providing long-range interaction.

which propagates in the background medium, is source-free in the subvolume $D_{sct}$ [see figure 4.1 and (Fokkema and van den Berg, 1993)].

Ting and Miksis (1986) have shown how equation 4.3 can be used to predict outgoing waves arriving at the boundary, B, of a computational domain by extrapolating the scattered wavefield from an auxiliary surface surrounding the scatterer through free space. This involves substituting free-space Green's functions and evaluating equation 4.3 at time-retarded values $t - r/c$ (with $r/c$ the traveltime between the extrapolation surface and the boundary). Because the waves arriving at the edge of the computational domain are matched by the Kirchhoff extrapolated waves, the differences involved in the finitely discretised equations of motion are exactly as they would be in the case of outgoing boundary conditions, and hence the boundary is non-reflecting.

## 4.3 Exact boundary conditions for perturbed scattering problems

If the scatterer occupies just a small part of the background model and the medium is inhomogeneous outside the extrapolation surface, S, ingoing waves resulting from interaction of the scattered wavefield with the background model will be present and the above approach no longer yields the correct boundary data required to truncate the computational domain at B. However, equation 4.3 may still be used to extrapolate the wavefield to any point outside the extrapolation surface, S, as long as the exact, full waveform Green's functions for the inhomogeneous background model are used instead of free-space Green's functions. Moreover, the boundary data at B can no longer be calculated by evaluating equation 4.3 *only* at time-retarded values since multiple scattering between the perturbed region and the inhomogeneous background model may affect the boundary data at all later times[1]. For modeling purposes, we can write equation 4.3 recursively to make the contribution of scattered wavefield at time $t$ to all later times explicit. After discretizing the convolution integral in time this gives:

$$\begin{aligned}
\hat{p}^{sct}(\mathbf{x}^R, l, n) &= \hat{p}^{sct}(\mathbf{x}^R, l, n-1) \\
&+ \int\limits_S \Big[\hat{G}^q(\mathbf{x}^R|\mathbf{x}, l-n)\hat{v}_k(\mathbf{x}, n) \\
&+ \hat{\Gamma}^q_k(\mathbf{x}^R|\mathbf{x}, l-n)\hat{p}(\mathbf{x}, n)\Big] n_k \mathrm{dS},
\end{aligned} \tag{4.4}$$

---

[1] Thus, one difference between the present exact boundary condition and the work by Ting and Miksis (1986) is that their method is looking backward in time from the boundary (i.e., relying on previously computed values on the extrapolation surface or even the surface of the scatterer) since because of the simplicity of the model they know exactly at which single (retarded) time to look. In contrast, our method is looking forward in time from the extrapolation surface, keeping track of which points on the boundary will be *causally* influenced by what is happening on the extrapolation surface at the current time.

where ˆ is used to differentiate between continuous time and sampled quantities. Thus, to update the scattered wavefield $\hat{p}^{sct}(\mathbf{x}^R, l, n-1)$ at $\mathbf{x}^R$ at timestep $n$ of the computation for all future time steps $l > n$, one has to scale the Green's functions $\hat{G}^q(\mathbf{x}^R|\mathbf{x}, l-n)$ and $n_k\hat{\Gamma}^q_k(\mathbf{x}^R|\mathbf{x}, l-n)$ by the current value of the normal component of particle velocity $\hat{v}_k(\mathbf{x}, n)n_k$ and the pressure $\hat{p}(\mathbf{x}, n)$ on the extrapolation surface and add this to the previously computed boundary values. Equation 4.4 needs to be complemented by the incident wavefield $\hat{p}^{inc}(\mathbf{x}^R, n)$ to give the total wavefield at $\mathbf{x}^R$ on B.

The resulting boundary condition is exact and equivalent to the Neumann series solution to the scattering problem (Snieder and Scales, 1998). It includes all orders of interactions between the background model and the perturbations. We now show how to compute the Green's functions in equation 4.4 required for extrapolation efficiently.

## 4.4 Interferometry

In the interferometric paradigm, waves at two receiver locations are correlated to find the Green's function between them. As shown in chapters 2 and 3 and Wapenaar and Fokkema (2006), there is a strong link between interferometry and reciprocity. Consider the acoustic reciprocity theorem of the correlation type (Fokkema and van den Berg, 1993):

$$\begin{aligned}\int_S \left[C_t\left\{p^A, v_k^B\right\} \right. &+ \left. C_t\left\{v_k^A, p^B\right\}\right] n_k \mathrm{dS} = \\ \int_V \left[C_t\left\{f_k^A, v_k^B\right\} \right. &+ C_t\left\{p^A, q^B\right\} \\ +C_t\left\{v_k^A, f_k^B\right\} &+ \left. C_t\left\{q^A, p^B\right\}\right] \mathrm{dV}, \end{aligned} \tag{4.5}$$

where $C_t\{f, g\}$ denotes the temporal crosscorrelation of functions $f$ and $g$, $S$ is a surface surrounding a volume $V$ with radiation conditions on at least part of the surface, and $n_k$ are the components of the normal to the surface $S$. An interferometric representation for the pressure due to a point source of volume injection, $G^q(\mathbf{x}^A|\mathbf{x}^B, t)$, between points $\mathbf{x}^A$ and $\mathbf{x}^B$, can be derived by taking state A to be the wavefield generated by a point source of volume injection at $\mathbf{x}^A$:

$\left\{p^A, v_k^A\right\}(\mathbf{x}, t) = \{G^q, \Gamma_k^q\}(\mathbf{x}|\mathbf{x}^A, t)$ and $\left\{q^A, f_k^A\right\}(\mathbf{x}, t) = \left\{\delta(t)\delta(\mathbf{x}-\mathbf{x}^A), 0\right\}$ and state B to be the wavefield generated by a point source of volume injection at $\mathbf{x}^B$: $\left\{p^B, v_k^B\right\}(\mathbf{x}, t) = \{G^q, \Gamma_k^q\}(\mathbf{x}|\mathbf{x}^B, t)$ and $\left\{q^B, f_k^B\right\}(\mathbf{x}, t) = \left\{\delta(t)\delta(\mathbf{x}-\mathbf{x}^B), 0\right\}$. Inserting these expressions into equation 4.5, performing the volume integrations and using reciprocity we find:

$$\begin{aligned} G^q(\mathbf{x}^B|\mathbf{x}^A, t) &+ G^q(\mathbf{x}^B|\mathbf{x}^A, -t) = \\ \int_{\mathbf{x}\in S} \big[G^q(\mathbf{x}^A|\mathbf{x}, t) &* G_k^f(\mathbf{x}^B|\mathbf{x}, -t) \\ +G_k^f(\mathbf{x}^A|\mathbf{x}, t) &* G^q(\mathbf{x}^B|\mathbf{x}, -t)\big]\, n_k \mathrm{dS}, \end{aligned} \tag{4.6}$$

where * denotes temporal convolution. Similarly, an interferometric representation for the pressure due to a point force source can be derived. By systematically illuminating the model from the surrounding surface, while storing the wavefield in as many points in the interior as possible, full waveform Green's functions can be computed for any pair of points using only crosscorrelation and numerical integration [see chapters 2 and 3 and van Manen *et al.* (2005, 2006) for details]. This allows the Green's functions $\hat{G}^q$ and $\hat{\Gamma}_k^q$ required to update the boundary condition in equation 4.4 to be computed efficiently.

## 4.5 1D Example

The exact boundary condition is demonstrated in an example using a staggered finite-difference approximation of the 1D acoustic wave-equation. The model consists of single scattering layer (propagation velocity $c_s = 1750\ m/s$, mass density $\rho_s = 1250\ kg/m^3$) embedded in a homogeneous background medium between 130 m and 170 m depth ($c_0 = 2000\ m/s$, $\rho_0 = 1000\ kg/m^3$) and with a free surface at the top.

Since the model is one-dimensional and bounded by a free-surface at the top, a single source at the bottom of the well is sufficient to illuminate the model completely (see section 3.4.1 for details). Thus, only two conventional forward modeling runs were performed (one for each source type) and the data stored at every gridpoint. Non-reflecting boundary conditions were used just below the source to truncate the computational domain. Given the data of these two

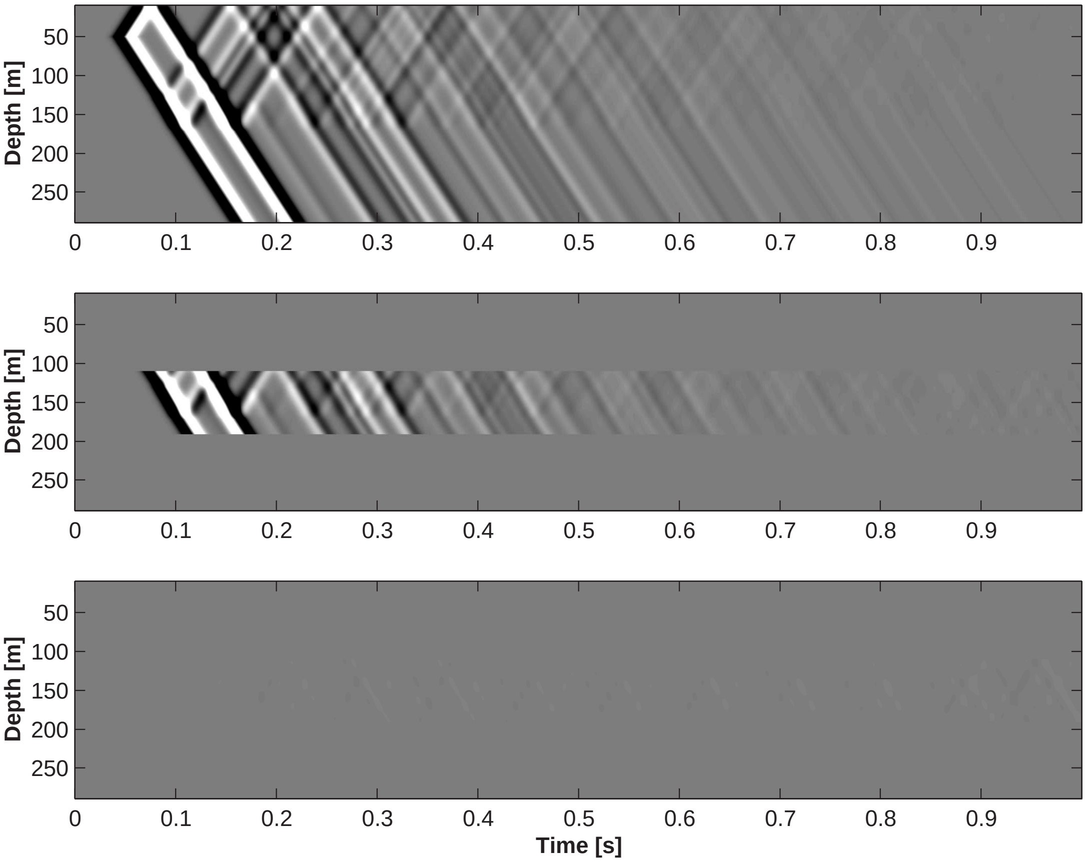

**Figure 4.2:** Comparison of the proposed exact boundary condition with a directly computed reference. (top) Pressure, directly computed for the perturbed model by FD on the full grid. (middle) Pressure, computed using the new method and FD on the subgrid. (bottom) Difference between (top) and (middle) for the extent of the subgrid (110-190 m).

initial simulations, Green's functions between arbitrary points in the well can be computed.

An incident wavefield was calculated using interferometry, for a volume injection source at 50 m depth, and receivers collocated with the pressure points at the planned edge of the truncated computational domain. Since the finite-difference calculations are done on a staggered grid, whereas the Kirchhoff integral (and also the integral in the interferometric construction) is evaluated for the pressure and particle velocity quantities collocated in space and time, care should be taken that the required pressure and particle velocities are linearly interpolated to the same location and time.

Auxiliary extrapolation "surfaces" were defined just above and below the scattering layer at 125 m and 175 m depth. Next, the model was strongly

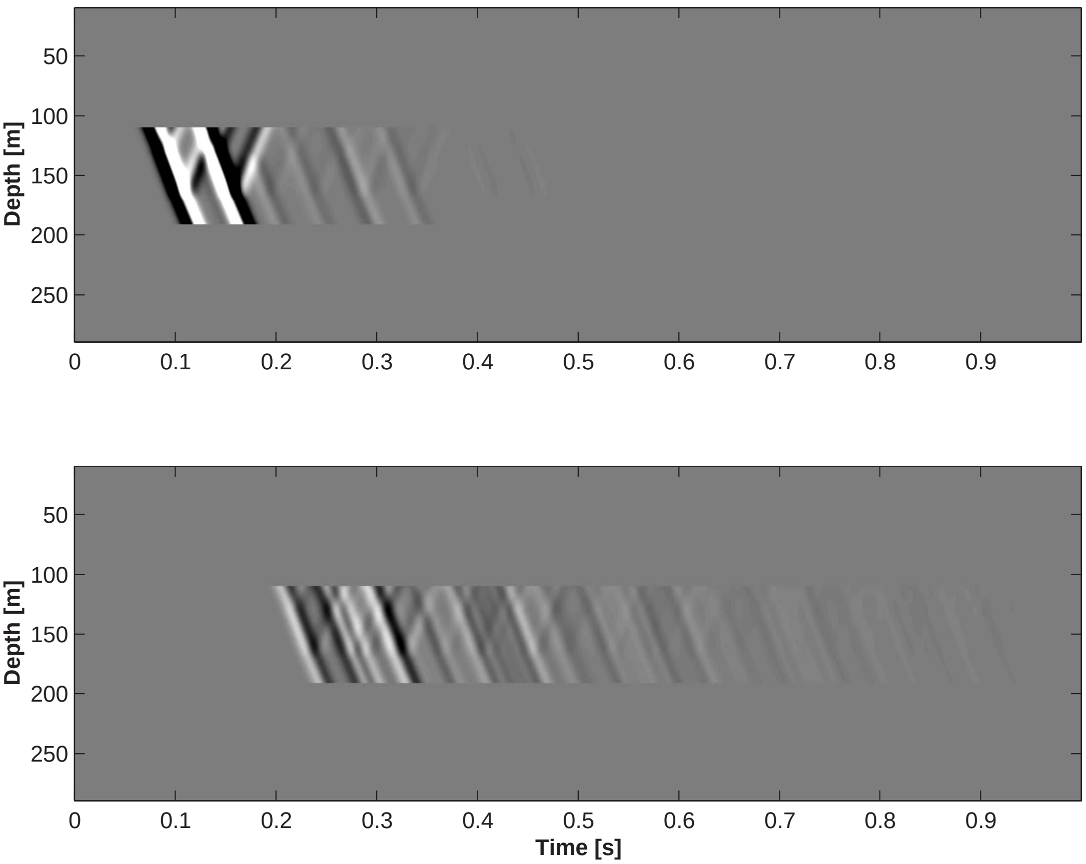

**Figure 4.3:** Comparison of conventional FD-injection with a directly computed reference. (top) Pressure, computed using conventional FD-injection. (bottom) Difference between (top) and a directly computed reference for the extent of the subgrid (110-190 m).

perturbed by increasing the velocity by 500 $m/s$ and the density by 250 $kg/m^3$ in the scatterer. Since there is a free surface, waves scattering off the perturbation will reflect at the free surface and repeatedly interact with the perturbation. Thus, high-order, long-range interactions will be present, ruling out a Born approximation or conventional finite-difference injection to compute the response on the perturbed model.

To compute the response using the new methodology, the computational domain was truncated 15 m above and below the extrapolation points (at 110 m and 190 m depth, respectively). The offset of 15 m between the extrapolation surface and the boundary of the truncated domain was chosen to prevent errors due to the diffraction limit inherent in the interferometric Green's functions (de Rosny and Fink, 2002). Without loss of generality, we opted for a pressure

(Dirichlet) boundary condition at the edge of the truncated computational domain and collocated the evaluation points of the Kirchhoff integral with the (staggered) FD pressure points at the edge of the grid. Thus, Green's functions for extrapolation through the background model need to be computed between all combination of points with one point on the extrapolation and one point on the "injection" surface (i.e., between 125 m and 110 m, 125 m and 190 m, 175 m and 125 m, and 175 m and 190 m) and for both pressure-to-pressure and particle velocity-to-pressure interactions, giving a total of 8 extrapolation Green's functions for this simple 1D example.

In practice, the Kirchhoff extrapolation (equation 4.4) is evaluated for every time-step of the finite-difference simulation on the truncated perturbed domain and the resulting seismograms are added to a buffer of future boundary values. The next sample from the buffer is then used as the boundary condition for the subsequent time-step in the FD calculation. The wavefield on the perturbed grid resulting from the new boundary condition is shown in figure 4.2 (middle panel). Note that no additional absorbing boundary conditions were used outside the new exact boundary condition. The resulting pressure wavefield can be compared to a reference wavefield in figure 4.2 (top panel). In the bottom panel, the difference between the top and middle panel is shown for the extent of the subgrid (110-190 m). The first high-order long-range interactions start between 0.2 s and 0.24 s (depending on the depth). Thus, the high-order long-range interactions are reproduced exactly.

For reference, in figure 4.3, the wavefield computed using conventional FD-injection (Robertsson and Chapman, 2000) (top panel) and the difference with a directly computed reference solution are shown (bottom panel), again for the extent of the subgrid (110-190 m). Note that already at 0.2 s, when the second-order long-range interactions start, conventional FD-injection breaks down. In such a case, we have no alternative but to compute all high-order long-range interactions using a different method, such as the one presented here.

## 4.6 Leading order CPU estimate

To assess the impact of the presented exact boundary condition, I now estimate the computational cost to the leading order. Three main parts can be identified in the methodology outlined above:

1. Interferometry to compute the extrapolation Green's functions,
2. Regular finite-difference update on the subgrid, and,
3. Extrapolation of the wavefield to the injection boundary.

The first step is performed only once for each subvolume and does not have to be repeated when considering multiple perturbations (or incident wavefields) of the same subvolume (see also below). Steps 2 and 3 are repeated for different perturbations. We now discuss the cost of each of the three steps in detail.

**Step 1: Interferometry to compute the extrapolation Green's functions** Let $N_Z$ and $N_D$ denote the original model size and the reduced size, respectively, and $N_T$ the number of time-steps for which the model is to be run[2].

The construction of a single interferometric Green's function requires cross-correlation of on the order of $N_Z$ traces (i.e., the number of points is of the same order as one of the sides of the model). The construction can be done efficiently by multiplication in the frequency domain (data stored as FFT) and results in on the order of $N_Z N_T$ operations (for details, see chapter 3). The number of points on the extrapolation surface and the injection boundary is of order $N_D^{m-1}$, i.e., one dimension less than the model dimensionality. Extrapolation Green's functions have to be constructed between any pair of those, resulting in $N_D^{2(m-1)}$ of them. Combining the cost of a single interferometric Green's function and the number of extrapolation Green's functions, we get for the total cost of computing the extrapolation Green's function: $N_Z N_T N_D^{2(m-1)}$.

---

[2] We use lowercase letters to denote the physical requirements and uppercase letters the simulation requirements. For example, $N_z$ is the number of depth points required to describe the physical model, whereas $N_Z$ is the number that may be required in the simulation model. Often $N_Z \gg N_z$. E.g., in finite-difference calculations: $N_Z \sim \frac{\omega_{\max}}{v_{\min}} \gg N_z$.

| | 1D (m=1) | 2D (m=2) | 3D (m=3) |
|---|---|---|---|
| Finite-difference full grid | $N_Z^2$ | $N_Z^3$ | $N_Z^4$ |
| Finite-difference subgrid | $N_D N_Z$ | $N_D^2 N_Z$ | $N_D^3 N_Z$ |
| Kirchhoff extrapolation | $N_Z^2$ | $N_D^2 N_Z^2$ | $N_D^4 N_Z^2$ |

**Table 4.1:** Leading order number of floating point operations for the exact boundary condition. Note that for simplicity we have assumed that the number of timesteps, $N_T$ is of the same order as the number of depth points in the simulation model, $N_Z$.

**Step 2: Regular finite-difference update on the subgrid** This step is proportional to $N_D^m N_T$, the length of the subgrid raised to the dimensionality of the model, times the number of timesteps.

**Step 3: Extrapolation of the wavefield to the injection boundary** After each timestep of the regular FD update (i.e., step 2), all $N_D^{2(m-1)}$ extrapolation Green's functions (of length $N_T$) must be scaled by the field values at the extrapolation surface and integrated. This takes on the order of $N_D^{2(m-1)} N_T$ operations each timestep, and $N_D^{2(m-1)} N_T^2$ for the whole simulation.

Note that we have not included the initial cost of systematically illuminating the model from the outside since this is done only once and does not have to be repeated when considering multiple arbitrary model perturbations. We only include such steps that need to be recomputed when considering perturbations in another subvolume, so that we can explicitly compare against the cost of a single finite-difference run on the full grid for the perturbed model.

To proceed further, we assume that the number of timesteps, $N_T$, is of the same order as the number of depth points in the simulation model, $N_Z$. In table 4.1, the computational cost of the different steps is summarized for one, two, and three dimensions. Note that the cost of the finite-difference update on the subgrid is typically insignificant compared to the cost of repeated evaluation of the Kirchhoff extrapolation integral and therefore is neglected in the following. Thus, in order for the exact boundary condition to be more efficient than direct finite-difference computation on the full grid, we find the following inequalities:

$$\begin{aligned} \text{1D:} \quad & N_Z^2 \leq N_Z^2 \\ \text{2D:} \quad & N_D^2 \leq N_Z \\ \text{3D:} \quad & N_D^4 \leq N_Z^2. \end{aligned}$$

Thus, for 1D, since $N_D$ does not enter the equations (the number of extrapolation and injection points is just two regardless of the size of the enclosed perturbation), the cost is roughly of the same order as direct finite-differences on the subgrid. For 2D and 3D, we get the same condition, namely that the length of the subgrid should be smaller than the square-root of the number of depth points in the full grid.

At this point it should be mentioned that some of the multiplying constants ignored in the leading order estimate are quite large and therefore one should be cautious not to draw too many conclusions from the above leading order estimate. The main point of the calculation is to show that, although the number of points on the extrapolation surface surrounding the subgrid is small, since the extrapolation needs to be done between all pairs of points and is repeated at every timestep of the finite-difference calculation on the subgrid, some of the immediate advantages of the presented exact boundary condition disappear[3].

Finally, note that, although the number of floating point operations for the exact boundary condition may be comparable to direct computation on a full grid, the *nature* of the calculations *is* different. Evaluation of the Kirchhoff integral only requires scaling and summation of extrapolation Green's functions and hence is highly suitable for vectorization/parallelization. Moreover, there are likely to be significant advantages in terms of memory as well.

## 4.7 Discussion

The presented method is exact and includes all second and higher-order long range interactions with the background model that were missing in conventional

---

[3] Note that, it may be possible to significantly increase the time interval between successive extrapolations by subsampling the extrapolation Green's functions to the Nyquist frequency of the output data, provided proper temporal stabilization (e.g., by averaging in time) is in place.

FD-injection (Robertsson and Chapman, 2000). This accuracy, however, comes at a price: the cost estimate in the previous section suggests that the new method is not always more efficient than computing the wavefield for the perturbed medium on the full grid directly.

It is an open question whether an *exact* method to update full waveforms after localized model perturbations that includes all interactions with the background model *can* be more efficient than, e.g., direct finite-differences on the full grid. Since the perturbed wavefield will interact with all parts of the background model, in a way that is impossible to predict in advance, such interactions need to be computed somehow. The keyword here, obviously, is *somehow*, as it implies that there may be no way to circumvent this cost.

Nevertheless the other keyword in the previous paragraph, *exact*, allows more room for improvement than suggested above. Suppose we are only interested in long-range interactions with the background medium up to a certain pre-defined order. Surely we should be able to do better than direct full waveform modeling on the full grid! Thus, the question of a Neumann series for the exact boundary condition arises and a closer look at the hybrid boundary integral equation + Born series modeling scheme by Schuster (1985) seems warranted.

### 4.7.1 A Born (Neumann) series representation for the exact boundary condition

In the following we refer to a Born series as a series between surfaces of scattering regions rather than between individual point scatterers. This terminology is inspired by the work of Schuster (1985) on the Generalized Born Series (GBS). The GBS is based upon perturbing a surface boundary integral equation (SBIE) matrix for a multi-body scattering problem into a part to be easily inverted, called the self-interaction operator, and a part not to be inverted at all, called the extrapolation operator. By applying the inverse of the self-interaction operator to the surface boundary integral equations, Schuster (1985) obtained a new integral equation which can be solved efficiently with a Born-like series using the extrapolation operator.

More specifically, what Schuster (1985) calls a self-interaction operator, S, is the set of boundary integral equations (BIE) for a single volume scatterer (or perturbed region) in a background medium. It is possible to arrive at a similar set of equations for the exact boundary condition presented here by collocating the extrapolation and injection surfaces and by substituting a Kirchhoff integral representation for the propagation on the interior of the perturbed region[4]. The integral representation for the exterior remains unchanged and uses the interferometric Green's functions computed for the background medium. The resulting system can then be solved by a pure BIE method. Alternatively, the self-interaction operator can be solved by collocating the extrapolation and injection surfaces and solving the extrapolation in conjunction with FD on the perturbed grid. The latter approach was used by Teng (2003) for homogeneous background models. Note that both approaches require dealing with singularities arising from the collocation of the extrapolation and injection surfaces.

The upshot of all this is that, notwithstanding subtle mathematical differences, inverting the self-interaction operator is equivalent to computing the long-range interactions between a perturbed region *in isolation* and the background model using the exact boundary condition. Moreover, the long-range interactions *between scatterers* in the generalized Born series are taken into account by using the extrapolation operator to iteratively extrapolate the full reflection response computed for each individual scatterer in what amounts to a Born-like series.

Notice that if we formally want to demonstrate that the exact boundary condition can be written as a Born like series we still need to explain what happens to the scattered wavefield from an isolated first perturbation when injected into other perturbed regions. Since such scattered wavefields already contain all interactions with the background model (because the exact, full waveform Green's functions are used), it is non-trivial that subsequent injection and extrapolation doesn't *double* the contribution from the background model.

Clearly, the support of the wavefield scattered off a first perturbation *in isolation* does not extend beyond the perturbation itself. Therefore, the scattered wavefield propagating *in the background medium* is source-free everywhere else, including inside the other perturbed regions. As a result, the part of the scattered

---

[4] Note that it is not immediately clear which Green's functions should be used for this interior Kirchhoff integral. Intuitively, Green's functions for the perturbed region with outgoing boundary conditions should be used. In practice, this would require FD computations for sources distributed on the surface surrounding the truncated perturbed region, with absorbing boundary conditions outside. It would be quite costly, but by no means impossible.

wavefield propagating in the background medium does not contribute to the Kirchhoff-Helmholtz integral when evaluated for the other perturbed regions and we are left with the interaction of the scattered wavefield with the other perturbations[5].

This means that we can apply the same iterative procedure as Schuster (1985) and solve for the second- and higher-order long-range interactions between the scattering regions using a Born (Neumann) series:

1. First we compute the self-interaction of each perturbed region with the background model in isolation using the new exact boundary condition while storing the resulting scattered wavefield at the receivers and at all other injection surfaces.
2. Next for each perturbed region we superpose the scattered wavefields due to all the other perturbed regions (computed separately in step 1) as injection wavefield and compute the self-interaction again for each perturbed region in isolation while storing the resulting scattered wavefield at the receivers and all other injection surfaces.

This process is repeated until the desired order of long-range interactions has been computed. The Neumann series is explained in figure 4.4. At this point I should like conclude this section with the following remarks:

- While at first sight it appears that we have succeeded in deriving a Neumann series representation for the exact boundary condition and hence have found a way of trading accuracy for efficiency, this is not the case. We have presented a different Neumann series, namely for the high-order interactions *between volume scatterers*, and not for high-order interactions *between the volume scatterer and the background medium* as desired. This is a different Neumann series and should be clearly distinguished. An analysis of the latter Neumann series is beyond the scope of this thesis.
- In practice, we would probably not calculate the response for the different volume scatterers in isolation, but instead run the finite-differences on the

---

[5] Note that this reasoning is completely analogous to the reasoning in section 4.2, demonstrating that the incident wavefield vanishes when integrated over the surrounding surface of a single perturbation.

perturbed subgrids simultaneously and continuously update the boundaries of the subgrids by Kirchhoff extrapolation at each timestep and hence compute the long-range interactions between the volume scatterers on the fly.

- The presented Neumann series for long-range interactions between volume scatterers can also be applied easily to conventional FD-injection techniques (Robertsson and Chapman, 2000). The scattered wavefield leaking out the perturbed region (missing the second- and higher-order long-range interactions with the background model) is extrapolated through the background medium to the other perturbed regions and injected in the usual fashion. This leads to another set of scattered wavefields which can then be re-injected in the original perturbed region to obtain the long-range interactions between the perturbed regions.

### 4.7.2 Hybrid modeling

Note that although interferometry provides the required full waveform Green's functions for extrapolation through the background medium cheaply and accurately, interferometry is not strictly required for the exact boundary condition. In principle, the Green's functions can be computed by direct finite-differences or any other full waveform forward modeling method, although generally at a higher computational cost.

However, in some cases where part of the (background) medium is particularly simple or satisfies certain symmetry properties, it may be more efficient to compute the Green's functions for the background medium using a different (non-interferometric) method. For example, if the background medium is horizontally layered, a reflectivity method (Kennett, 1983) is the obvious method of choice. Thus, the exact boundary condition makes it possible to consider, for example, an inhomogeneous layer embedded between two horizontally layered halfspaces (stacks).

Similarly, when considering scattering from a set of irregularly shaped inhomogeneous objects embedded in a homogeneous background medium, analytic free-space Green's functions can be used to connect the subgrids for full waveform

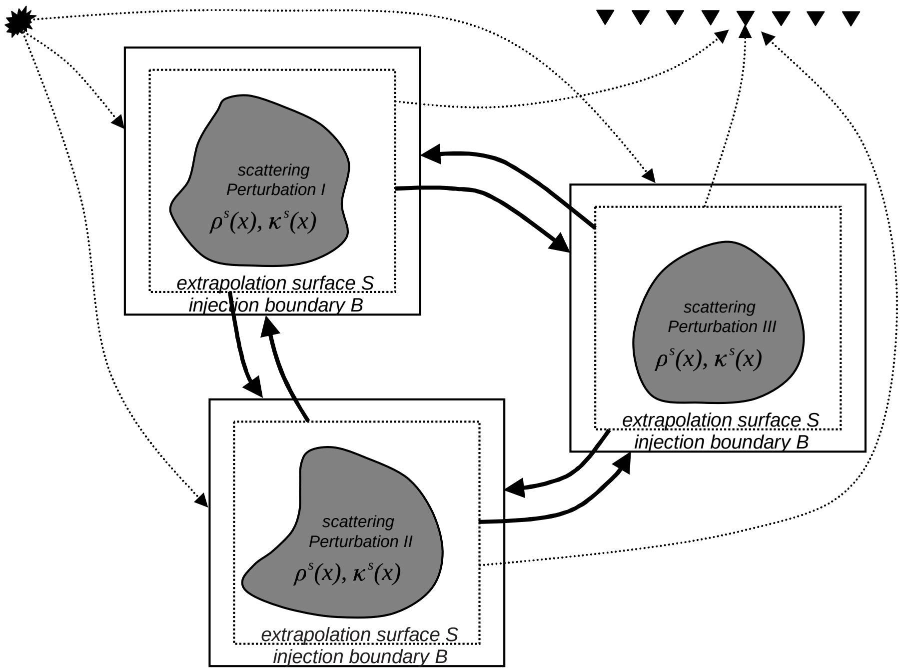

**Figure 4.4:** Long-range interactions between volume scatterers in the presented exact boundary condition. Note that the extrapolation from one volume scatterer's extrapolation surface to the other scatterer's injection surfaces through the background model is equivalent to application of Schuster's (1986) extrapolation operator. Similarly, computation of the full response for one volume scatterer *in isolation*, including all high-order long-range interactions with the background model, is equivalent to inverting Schuster's (1986) self-interaction operator. For details see text.

modeling. In this way, the expensive part of the modeling (e.g. finite-differences) is only applied locally, whereas the extrapolation from one scatterer to the others is done using free-space Green's functions. The exact boundary condition ensures that all orders of interactions between the scatterers are included in the calculation.

Thus, the exact boundary condition teaches us how to couple the results of typically expensive full waveform modeling applications, as applied locally, to inexpensive global modeling methods, so that all orders of interactions between the complicated volume scatterers and the less complicated (but potentially still inhomogeneous) background medium are modeled correctly. Combined with significant advantages in terms of memory, this makes the exact boundary condition an essential ingredient for future hybrid modeling methods.

### 4.7.3 Absorbing Boundary Conditions

Besides the generalized Born series and hybrid modeling, the exact boundary condition also finds application as an absorbing boundary condition. Provided the full waveform Green's functions (one-way) are available to extrapolate the wavefield from an auxiliary surface surrounding the domain of interest to the boundary of the computational domain several gridpoints outside, the computational domain can be truncated by using the integral representation of the exact boundary condition to extrapolate the (outgoing) wavefield to the edge of the computational domain and match the waves propagating on the grid there. This is very similar to the original application proposed by Ting and Miksis, who were also interested in truncating the domain of calculation for an exterior scattering problem. The main difference here is the realization that the method can be applied beyond the homogeneous embedding.

## 4.8 Conclusion

The presented boundary condition is exact and can be used to compute the response, including all higher-order long-range interactions, to multiple arbitrary perturbations in inhomogeneous models. There are no restrictions on the medium between the extrapolation surface and the boundary of the truncated computational domain as long as it is exactly the same as in the background model. No additional absorbing boundaries are necessary and no special functions or singular integrals need to be evaluated. Although the computational cost of the new method is roughly of the same order as direct computation on the full grid, the nature of the computations make it an ideal candidate for parallelization and efficient memory implementations. When multiple perturbed volume scatterers are present, the interaction between the volume scatters can be written explicitly as a Neumann series. A similar Neumann series for the interaction between the background model and individual volume scatterers may provide a way to trade-off accuracy for computational cost. It is expected that the exact boundary condition will have a significant impact on hybrid and full waveform modeling.

# *Chapter 5*

# Receiver functions

## 5.1 Introduction

A receiver function is a time- or frequency-domain trace resulting from a particular combination, usually deconvolution, of P- and S-wave seismograms. The aim of receiver function calculation is to produce a trace which isolates propagation effects due to structure close to the receiver. By exploiting mode-conversions of the wavefield close to the receiver, features common to the waveforms of the converted and unconverted waves are divided out in the deconvolution, and the imprint of the source and of bulk propagation effects are removed.

The receiver function method has its origin in earthquake seismology where often, after registration of a teleseismic P-wave on the vertical component seismogram, a strong trailing coda was observed on the horizontal components. This coda was found to consist of shear waves, resulting from mode-conversion at intra-crustal and upper-mantle discontinuities. Phinney (1964) initially proposed calculating spectral ratios of the vertical divided by the horizontal component to isolate and invert the crustal coda for structure close to the receiver, but it was only after Langston (1979) and Vinnik (1977) independently made two minor modifications to the spectral ratio method that one can really speak of receiver functions. Both researchers proposed dividing the horizontal components by the vertical and worked in the time-domain instead of the frequency-domain. This had two advantages: first, since the P-wave was recorded almost unperturbed on the vertical component, its complicated spectrum could be removed successfully from the horizontal component trace. More importantly, the arrival times of all mode-converted waves were shifted in time relative to the arrival of the P-wave. The resulting time-domain trace was more easily interpretable than Phinney's amplitude spectra and the implicit removal of the source signature effectively made it possible to compare and stack receiver functions for different earthquakes with varying depth and source mechanism.

More recently, van Manen (2001) and van Manen *et al.* (2003) have shown that the receiver function method can also be applied to multi-component seabed seismic data and that the resulting receiver functions provide information about the shear-wave static time-delays arising from low-velocity unconsolidated sediments close to the receiver. Their approach relied on deconvolution and stacking of receiver functions in the common receiver domain and is reproduced in figure 5.1. For a typical line of multi-component seismic data, on the order of 200 receiver functions were stacked into a single trace per receiver, producing a profile of receiver functions with high signal-to-noise ratio. Events in such a profile, corresponding to shallow mode-converted waves, constrained the shear-wave statics. However, in contrast to the seismological setting, they concluded that the main converted wave energy in the receiver functions originates from mode-conversion upon *reflection* rather than *transmission*.

In this chapter, I investigate whether the receiver function approach by van Manen *et al.* (2003) can be applied more generally to exploration and production seismic data. The result is a comprehensive treatment of receiver function processing, with specific application to multi-component reflection data in mind. In the first part (sections 5.4 to 5.6), I discuss three different ways of receiver function calculation and focus on their subsequent kinematic interpretation. Starting with the usual slowness domain implementation in section 5.4, I show that the recent work in the seismological community on moveout correction and stacking of receiver functions (e.g., Gurrola *et al.*, 1994; Ryberg and Weber, 2000) can be extended significantly, building on relevant results from the exploration and production seismic community. Results include a series expansion for the traveltime difference in generally horizontally layered media and a so-called Dix-Krey-type velocity inversion formula. This is followed in section 5.5 by a new approach, dubbed space-time domain (2D) deconvolution, which treats

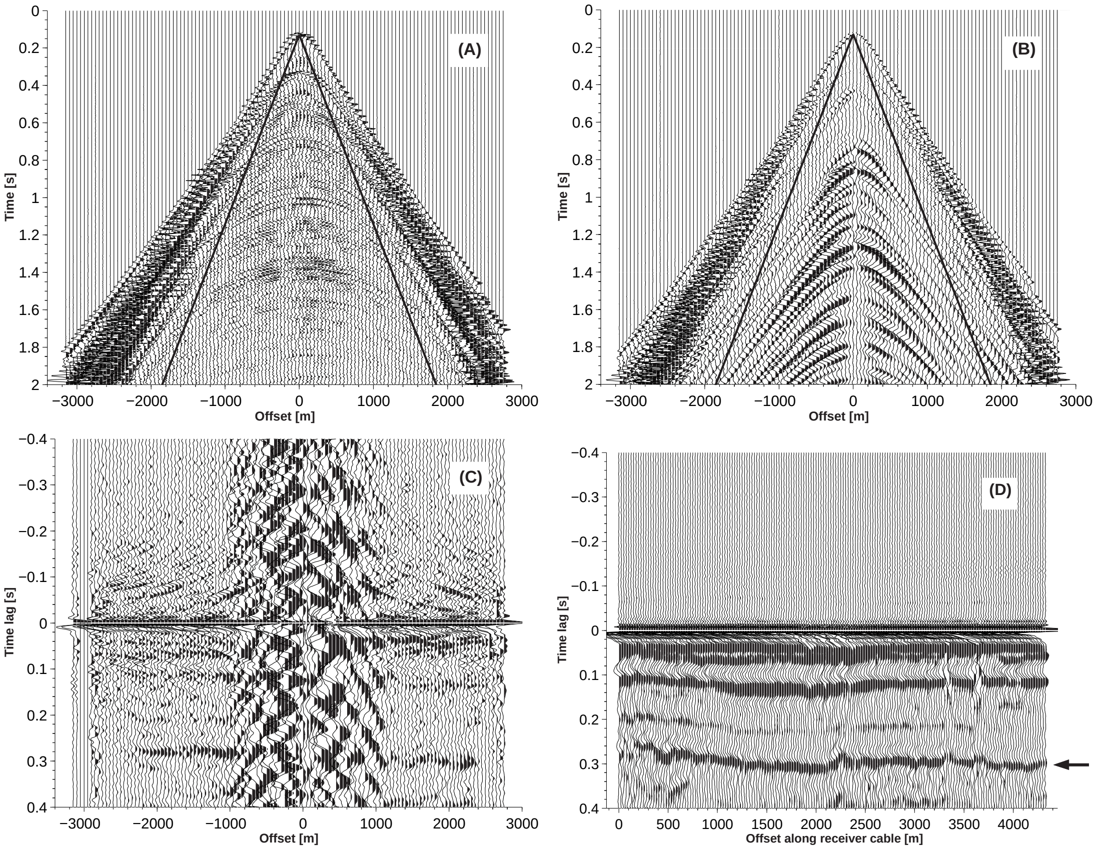

**Figure 5.1:** Shear-wave statics using receiver functions (after van Manen *et al.*, 2003). (A) Typical common receiver gather of hydrophone data. (B) Corresponding gather of inline horizontal component data. (C) Receiver functions calculated by stabilised deconvolution of the pressure from the respective horizontal component traces. Note the complicated behaviour in the centre of the gather. The receiver functions are subsequently stacked to form a single trace and this process is repeated for all receivers. (D) Profile of stacked receiver functions. The arrow denotes the shallow P-S mode-converted wave constraining the shear-wave statics. Note that to obtain this profile the pressure and horizontal component data in (A) and (B) were muted below the black solid lines. This suggests that the mode-conversion takes place upon reflection rather than transmission.

the spatial aspects of mode-conversion completely analogously to the temporal aspects. Thus, the receiver function becomes a two-dimensional transfer function, which shows how far the P-waves have to be shifted in space and delayed in time to match the corresponding PS-converted waves. Again, a series expansion of the traveltime difference leads naturally to a two-term moveout approximation and a Dix-Krey-type velocity inversion formula, but this time as a function of the difference in horizontal travel-distance rather than slowness. The first part is concluded in section 5.6 with a method of receiver function calculation (and processing) that is model independent. By matching the slowness of the PP-reflected and PS-converted waves on the source-side, and exploiting the fact that the traveltime difference is stationary for the PP- and PS-wave, reflected and mode-converted at the same subsurface point, the complete downgoing P-wave leg (and all propagation effects associated with it!) can be removed in arbitrary inhomogeneous models, without any knowledge of the subsurface. A simple method for pre-stack migration of the resulting model-independent receiver functions in homogeneous media is also discussed. Finally, the power of the model-independent approach is illustrated with an example of a case where increased attenuation suffered in the down-going P-wave leg is removed by the deconvolution.

In the second part of the chapter (section 5.7), dynamic aspects of receiver function processing are discussed as these naturally arise when examining the differences between receiver function calculation in a reflection and a transmission setting. It is shown that even for a two-layer reflection seismic example, there no longer exists a simple transfer function connecting the two pairs of PP-reflected and PS-converted waves. By developing a non-stationary filter model for the receiver function, it is then shown that the receiver function no longer is a function but is a matrix in the reflection setting. Finally, I end the chapter with some conclusions.

First, however, I briefly review the main observations and assumptions underpinning the receiver function method and highlight wavefield decomposition as a necessary pre-processing step, before returning to the roots of the receiver function method with the slowness domain implementation.

## 5.2 A first model for receiver functions

The concept of a receiver function would not be useful if there were not some underlying physical reality in which the vertical and horizontal components of teleseismic body wave data are simply related and share some common convolutional components. In other words, a receiver function derives its meaning, not from its definition in terms of a mathematical operation such as deconvolution, but from observational facts. They are worth repeating here for teleseismic transmission data, as they may or may not be valid when applying the receiver function method to reflection seismic data:

1. the P-waves are recorded dominantly on the vertical component, and
2. they are not affected much by the intra-crustal discontinuities, whereas
3. the S-waves are recorded dominantly on the horizontal components, and
4. they are the result of P-S conversion at intra-crustal discontinuities.

Based on these observations, seismologists like Phinney and Langston have formulated models that explain and predict, for realistic crustal and upper-mantle models, which combination of converted and unconverted waves will be present in the receiver function. Such models have helped them to see which information about the structure close to the receiver is isolated in the receiver functions, and how to extract it. The initial model they adopted was based on the following assumptions (figure 5.3):

- Pure-mode transmission coefficients (e.g., $T_{pp1}$, $T_{pp2}$, $T_{ss1}$, etc.) are close to unity and can be neglected as the teleseismic P-waves are near-vertically incident on the crust from below.
- Multiple mode-conversions can be neglected as their amplitude depends on the power of a number that is typically much smaller than one.
- Internal and free-surface related multiples are neglected (i.e., only primary reflected and converted waves are recorded).
- The earth, to first approximation, is horizontally layered.

The last two assumptions are also very common in exploration and production seismology, especially in the early stages of velocity model building. Under these assumptions, as will be discussed in detail in section 5.7.1, the transmission receiver function, $H_t(t)$, in an $n$-layered model, has the following simple form:

$$H_t(t) \approx \sum_{k=1}^{n} Tps_k \cdot \delta(t - dtps_k), \tag{5.1}$$

where $Tps_k$ is the upward P-S transmission coefficient at layer $k$ and $dtps_k = \sum_{i=1}^{k} ts_i - tp_i$ with $ts_i$ and $tp_i$ the one-way P- and S-wave traveltimes through layer $i$, respectively. Hence, the transmission receiver function contains a single event per interface, related to mode-conversion at that interface. Note that the time difference between a PP-transmitted and PS-converted wave from a particular interface is summed (integrated) for all the layers above that converting interface and the amplitude of the event is, to first order, the PS-conversion coefficient of that interface. This extremely simple model preserves the two main features of receiver functions mentioned in the introduction: deconvolution of the source signature (i.e., the original source wavelet has been removed and replaced by a delta-function), and shifting of the converted waves relative in time to the arrival time of the main, unconverted wave. At this point it is still an open question whether such a simple model exists for reflection seismic receiver functions.

Obviously, even for a horizontally layered medium, the traveltimes $ts_i$ and $tp_i$ depend on the slowness of the incident wave and any model, whether for transmission or reflection receiver functions, should take this into account. This is discussed in detail in section 5.4.2. In section 5.4.3 we show how to extract the information that is present, in temporally integrated form, in receiver functions calculated for horizontally layered models. But first I show that wavefield decomposition is a necessary pre-processing step before calculating receiver functions in the slowness domain when observations 1 and 3 above are no longer met.

## 5.3 Receiver function pre-processing: wavefield decomposition

In figure 5.2 (top), synthetic space-time domain data for the six-layer model in table 5.1 is shown. The data was modeled using a two-dimensional (2D) reflectivity code (Kennett, 1983) and will be used to illustrate the processing steps involved with receiver function calculation in a reflection setting. On the left, the modeled vertical component of particle velocity is shown and on the right, the horizontal component. Note that the natural separation of P-waves on the vertical and S-waves on the horizontal is not complete and that significant amounts of P- and S-wave energy are projected onto the other component.

As was already mentioned in the introduction, the goal of receiver function calculation is to calculate some kind of transfer function between P- and S-waves which isolates propagation effects close to the receiver. When the P-waves are recorded dominantly on the vertical component and S-waves on the horizontal, this can be achieved by direct deconvolution of the vertical component out of the horizontal. However, when significant amounts of energy are projected on the other component due to increased angles of incidence – as is often the case in reflection seismics – a better approach is to decompose the wavefield into P- and S-waves before calculating receiver functions.

Wavefield decomposition of land multi-component seismic data has been discussed by many authors, including Dankbaar (1985), Wapenaar and Haimé (1990) and Robertsson and Curtis (2002). Wavefield decomposition of seabed seismic data is discussed by Amundsen and Reitan (1995), Donati and Stewart (1996) and Schalkwijk *et al.* (1999). A complete review of wavefield decomposition techniques is beyond the scope of this thesis. However, we discuss here briefly the decomposition of two-component land seismic data, as proposed by Dankbaar (1985), as this technique is used in our subsequent examples.

Let $\overline{Z}(k,\omega)$ and $\overline{X}(k,\omega)$ denote the vertical and horizontal components of particle velocity in the frequency-wavenumber domain, respectively[1]. Dankbaar (1985) has shown that upgoing P- and S-waves, $\overline{P}_{up}$ and $\overline{S}_{up}$, may be obtained

---

[1] It is convenient to decompose the data into plane waves by transforming the data to the frequency-wavenumber domain as the wavefield decomposition filters (to be introduced shortly) are a function of frequency and horizontal wavenumber (or slowness).

| Layer | $V_P$ (m/s) | $V_S$ (m/s) | h (m) |
|---|---|---|---|
| 1 | 1650 | 400 | 50 |
| 2 | 1775 | 700 | 75 |
| 3 | 1900 | 950 | 100 |
| 4 | 2000 | 1000 | 200 |
| 5 | 2250 | 1125 | 275 |
| 6 | 2750 | 1375 | 600 |
| 7 | 3000 | 1500 | $\infty$ |

**Table 5.1:** Medium properties of the six-layer over a halfspace model used to generate the reflectivity data in figure 5.2. $V_P$, $V_S$ and $h$ denote the P-wave velocity, S-wave velocity and thickness of the layers, respectively.

from $\overline{Z}$ and $\overline{X}$ as follows:

$$\overline{P}_{up}(k,\omega) = F_Z^P(k,\omega)\overline{Z}(k,\omega) + F_X^P(k,\omega)\overline{X}(k,\omega) \tag{5.2}$$

$$\overline{S}_{up}(k,\omega) = F_Z^S(k,\omega)\overline{Z}(k,\omega) + F_X^S(k,\omega)\overline{X}(k,\omega) \tag{5.3}$$

where the decomposition filters, $F$, acting on the vertical and horizontal components are:

$$F_Z^P(p) = \frac{(1-2V_S^2p^2)}{2V_P\left(V_P^{-2}-p^2\right)^{\frac{1}{2}}}, \tag{5.4}$$

$$F_X^P(p) = V_S^2p/V_P, \tag{5.5}$$

$$F_Z^S(p) = V_Sp, \tag{5.6}$$

$$F_X^S(p) = \frac{(1-2V_S^2p^2)}{2V_S\left(V_S^{-2}-p^2\right)^{\frac{1}{2}}}, \tag{5.7}$$

and $V_P$, $V_S$, and $p$ are the P- and S-wave velocities of the medium at the receiver array and the horizontal slowness, respectively. Note that the decomposition filters are independent of frequency.

In figure 5.2 (bottom), the result of applying wavefield decomposition to the vertical and horizontal component data in the top panels is shown. On the left, the upgoing P-waves are shown and on the right, the upgoing S-waves. Notice that the P-wave projections preceding the arrival of the first S-waves have now disappeared. Some minor, decomposition-related artifacts can also be seen. In the following we calculate receiver functions based on the PS-separated data only.

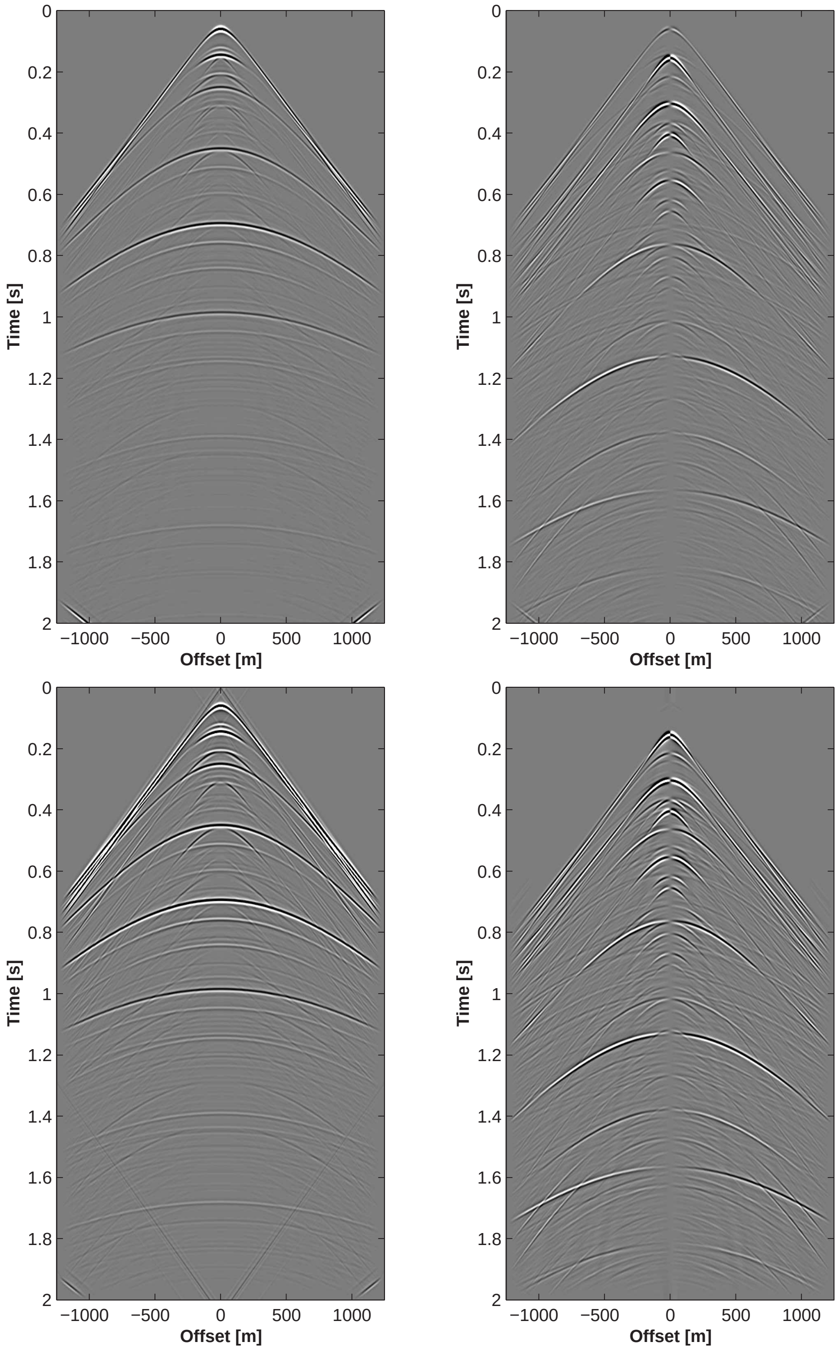

**Figure 5.2:** Space-time domain reflectivity data used in the receiver function examples. In the top panels, the vertical (left) and horizontal (right) components of particle velocity are shown. In the bottom panels, the result of applying wavefield decomposition to the data in the top panels is shown. On the left, the upgoing P-waves are shown, on the right, the upgoing S-waves. Note that the projections of the P-waves on the horizontal component and the S-waves on the vertical component have been removed.

## 5.4 Slowness domain treatment

### 5.4.1 Receiver function calculation I: 1D Deconvolution

In figure 5.3, a schematic drawing of all the raypaths and phases involved in conventional seismological receiver function calculation is shown. Because in a horizontally layered medium the horizontal slowness (henceforth referred to as just the slowness) is preserved upon refraction and mode-conversion at an interface in accordance with Snell's law, waves propagating at a first slowness do not interfere with waves propagating at a second slowness and the traveltime difference between P- and S-waves is most easily obtained as a function of slowness. Since we are looking for a transfer function between P- and S-waves from *the same wave-system*, it is natural to formulate the receiver function calculation in the slowness domain. If $\tilde{Z}(p,\omega)$, $\tilde{R}(p,\omega)$ and $\tilde{T}(p,\omega)$ denote the vertical, radial and transverse components in frequency-slowness $(\omega, p)$ domain, then the receiver functions are calculated as follows:

$$\tilde{H}_R(p,\omega) \quad = \quad \frac{\tilde{R}(p,\omega)\tilde{Z}(p,\omega)^*}{\tilde{Z}(p,\omega)\tilde{Z}(p,\omega)^* + \epsilon}, \tag{5.8}$$

$$\tilde{H}_T(p,\omega) \quad = \quad \frac{\tilde{T}(p,\omega)\tilde{Z}(p,\omega)^*}{\tilde{Z}(p,\omega)\tilde{Z}(p,\omega)^* + \epsilon}, \tag{5.9}$$

where $^*$ denotes complex conjugation and $\epsilon$ is some fraction of the maximum of the autocorrelation and is included to stabilize the division. Note that in a horizontally layered model, the P-SV system is completely decoupled from the SH system. For commonly used explosive-type sources in exploration and production seismic no SH-waves are generated and therefore we will not further discuss the tangential receiver function in the following[2]. When the vertical and horizontal component data have been separated into P- and S-waves, equation 5.8 for the radial receiver function becomes:

$$\tilde{H}_R(p,\omega) = \frac{\tilde{S}_{up}(p,\omega)\tilde{P}_{up}(p,\omega)^*}{\tilde{P}_{up}(p,\omega)\tilde{P}_{up}(p,\omega)^* + \epsilon}. \tag{5.10}$$

---

[2] The tangential receiver function plays an important role in crustal seismology in the determination of dipping layers (see e.g., Zhang and Langston, 1995) and crustal anisotropy (Levin and Park, 1997).

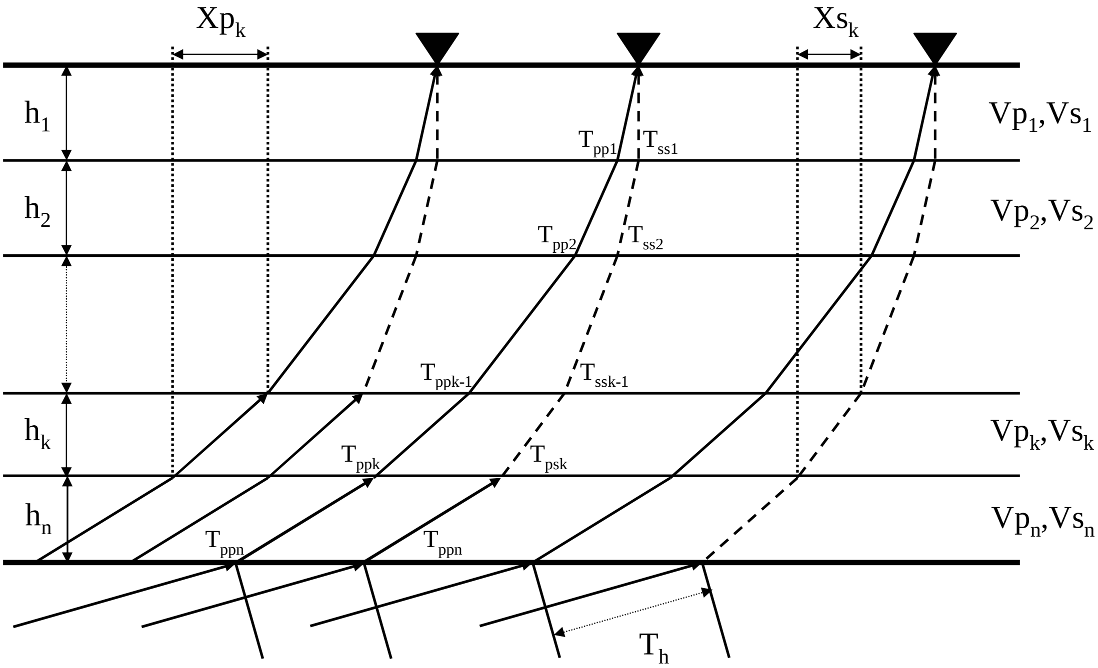

**Figure 5.3:** Schematic illustration of the phases and raypaths involved in the seismological receiver function setting. A plane P-wave is incident on a stack of n horizontal layers from below and mode-converts to shear-wave energy at discontinuities within and at the base of the stack. P- and S-waves are denoted by solid and dashed lines respectively. The data from each station are processed separately and the additional time Th is treated implicitly in the traveltime difference calculation.

In earthquake seismology, because of the large distances involved and the predominantly radially symmetric earth structure, teleseismic body waves at a receiver station are, to first approximation, planar and hence naturally separated as a function of slowness according to epicentral distance. In exploration and production seismology, the spherical nature of the reflected wavefield can not be neglected and the waves recorded along a receiver array must be decomposed into their plane wave components before equations 5.8 and 5.9 can be applied. Using the conventional definitions for the Fourier transform and $(\tau, p)$ transform we find for data $u(x,t)$ transformed into the frequency-slowness $(\omega, p)$ domain:

$$\tilde{U}(p,\omega) = \int\int_{-\infty}^{\infty} u(x,t) e^{i\omega(t-px)} dt dx, \tag{5.11}$$

$$u(x,t) = \frac{|\omega|}{(2\pi)^2} \int\int_{-\infty}^{\infty} \tilde{U}(p,\omega) e^{-i\omega(t-px)} dp d\omega, \tag{5.12}$$

where $\tau$, is related to the input time, $t$, the slowness, $p$, and offset, $x$, through $\tau = t - px$. The resulting $(\tau, p)$-domain receiver functions are found by inverse Fourier transforming equations 5.8, 5.9 and 5.10 along the frequency dimension, respectively.

In figure 5.4, the ($\tau$,p)-domain data obtained by transforming the (x,t)-domain reflectivity data from figure 5.2 are shown. In the top panels, the result of transforming the un-separated vertical and horizontal components is shown. In the bottom panels, the corresponding transformed, wavefield-separated data are shown. The left and right panels correspond to vertical and horizontal and upgoing P- and upgoing S-waves, respectively. By comparing the top and bottom panels, again it it clear that the natural separation of P-waves on the vertical and S-waves on the horizontal is not complete and that the data should be wavefield-separated before calculating the receiver functions.

In the next section a series expansion for the traveltime difference between P- and S-waves through horizontally layered models is derived and from this a general expression for the traveltime difference for PS-conversions (both upon reflection and transmission) at all layers arises.

### 5.4.2 Series expansion of the traveltime difference I: Function of slowness

Now that we know how to calculate receiver functions in the slowness domain, we need to understand better the timing of the events in the receiver functions. As mentioned above, even for a horizontally layered medium, the traveltimes $t_{pn}$ and $t_{sn}$ depend on the slowness of the incident wave. From global seismology, it is well known that the difference in traveltime $dt$ between a plane P-wave incident on a stack of $n$ horizontal layers from below and the corresponding PS-waves, converted upon transmission, can be written (Paulssen *et al.*, 1993):

$$dt = \sum_{k=1}^{n} h_k \left( \sqrt{Vs_k^{-2} - p^2} \quad - \quad \sqrt{Vp_k^{-2} - p^2} \right), \tag{5.13}$$

where $h_k$, $Vs_k$ and $Vp_k$ denote the thickness, shear- and compressional-wave velocity of layer $k$ respectively, and $p$ the slowness of the incident wave. Equation 5.13 implicitly takes into account the extra time it takes the incident wave

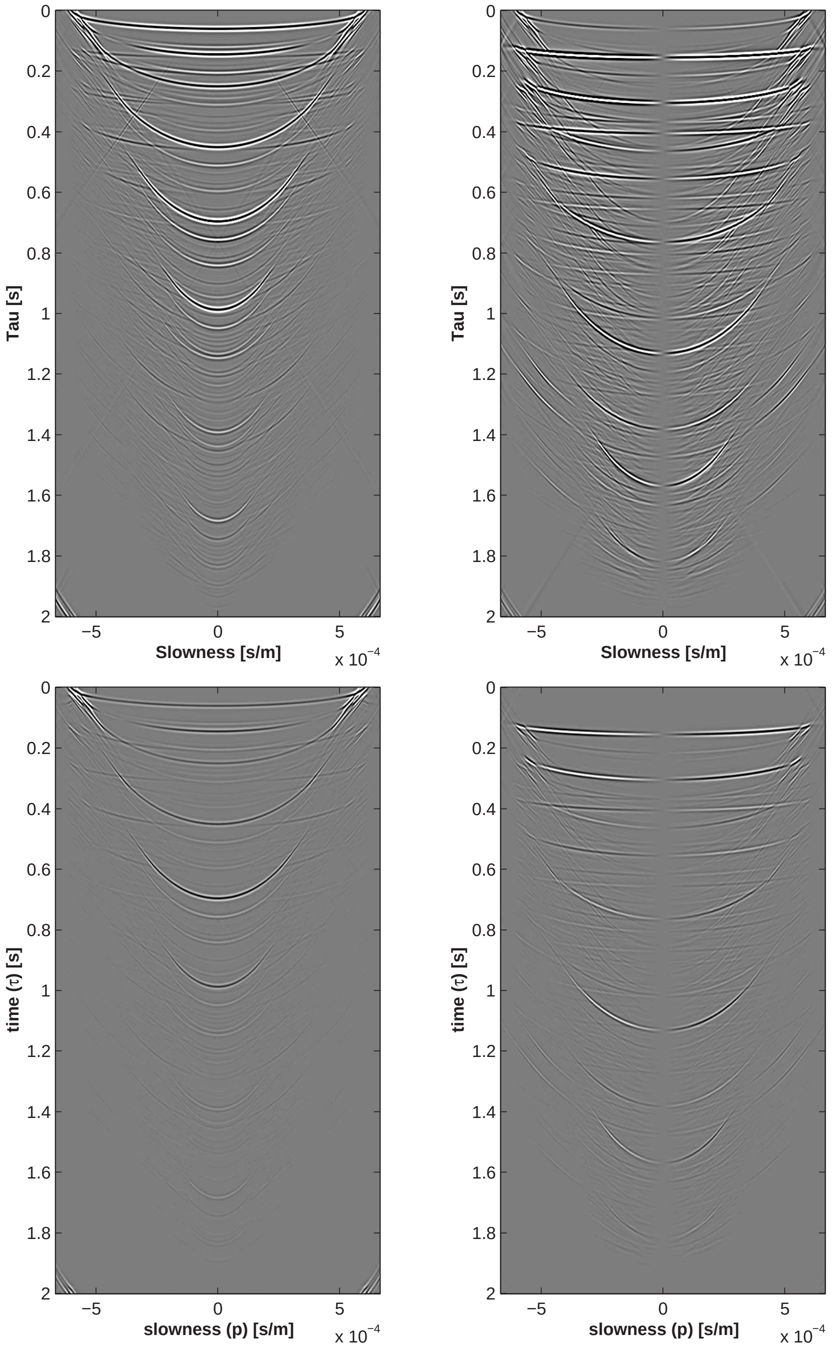

**Figure 5.4:** ($\tau$,p)-domain reflectivity data obtained by transforming the space-time domain reflectivity data from figure 5.2 using equation 5.11. In the top panels, the transformed vertical (left) and horizontal (right) components of particle velocity are shown. In the bottom panels, the transformed, upgoing P-waves (left) and upgoing S-waves (right) are shown. Notice how wavefield decomposition has removed the projections of the P-waves on the horizontal component and the S-waves on the vertical component.

to reach the horizontally offset conversion point at the base of layer $k$ and compares arrival times of PP-transmitted and PS-converted waves recorded at a *single* multi-component station (see figure 5.3). It is also valid in a reflection setting, provided the primary PP-reflected and PS-converted waves can be decomposed into their plane-wave constituents at a *single* station as discussed in the previous section.

As it stands, equation 5.13 is not very useful to model the moveout of events in receiver functions because it is a function of all unknown medium parameters above the converting interface and has a different number of terms in the right-hand side for different interfaces. Instead, it would be useful to find a representation for the traveltime difference with a form that is interface independent, consists of a small number of terms, and has a simple slowness dependence. For example, we could postulate the form: $dt = c_0 + c_1 p^2 + \cdots$. This would then allow fitting (determination of the $c_i$'s) of the observed moveout for each event in the receiver functions using the same two parameter equation and make it possible, for example, to sum the events corresponding to a particular interface along such curves to improve the signal-to-noise ratio of that event. In Appendix C it is shown that this can be achieved by expanding the square-root terms in equation 5.13 as Taylor series in the product $v^2p^2$, where $v$ can denote either P- or S-velocity. The result is:

$$dt^{smallp} = \sum_{k=1}^{n} h_k \left( Vs_k^{-1} - Vp_k^{-1} \right) + \frac{1}{2} \sum_{k=1}^{n} h_k \left( Vp_k - Vs_k \right) p^2. \tag{5.14}$$

The first term on the right of equation 5.14 is the difference in traveltime between a vertically incident P- and S-wave ($p$=0 s/m) through the stack of layers. The second term, multiplying $p^2$, is not simply interpretable since it contains products of layer thicknesses and differences in velocities and has units $[m^2/s]$. However, maintaining the analogy with normal moveout (NMO) corrections developed in exploration and production seismic, we call this the pseudo rms-velocity[3]. Thus

---

[3] In exploration and production seismic, the small-spread approximation has the form: $t^2 = C_0 + C_1 x^2$, where $C_0$ equals the square of the two-way traveltime at vertical incidence and $C_1 = (\sum_{k=1}^{n} \Delta\tau_k)/(\sum_{k=1}^{n} v_k^2 \Delta\tau_k)$, with $\Delta\tau_k \equiv h_k/v_k$ the vertical two-way traveltime through layer $k$. If we now interpret $C_1$ as the inverse of a squared velocity: $C_1 = 1/v_{\rm rms}^2$, then the small-spread approximation has the familiar hyperbolic form and the velocity becomes $v_{\rm rms} = (\sum_{k=1}^{n} v_k^2 \Delta\tau_k / \sum_{k=1} \Delta\tau_k)^{1/2}$, which, because of its form clearly merits the name rms

we have:

$$dt^{smallp} = dt_0 + \tilde{v}_{rms} p^2,$$

where

$$dt_0 \equiv \sum_{k=1}^{n} h_k \left( Vs_k^{-1} - Vp_k^{-1} \right), \tag{5.15}$$

$$\tilde{v}_{rms} = \frac{1}{2} \sum_{k=1}^{n} h_k \left( Vp_k - Vs_k \right). \tag{5.16}$$

Thus, all knowledge of the medium is implicit in the traveltime difference and pseudo rms-velocity for a particular interface (i.e., information about the medium is buried in coefficients $c_0$ and $c_1$ of the postulated two parameter curve). As hinted above, these parameters can usually be obtained from a so-called velocity spectrum stack [VSS] (see e.g., Gurrola *et al.*, 1994) by scanning over a range of realistic values for $\tilde{v}_{rms}$ at each $dt_0$ and calculating a measure of coherence of the receiver functions as a function of slowness called semblance. Using, these parameters it is thus possible to correct, for example, the moveout of an event corresponding to mode-conversion at the base of layer $k$ without *explicit* knowledge of the medium above that interface.

Note that for the special case of a single layer, the short-spread approximation reduces to the expression given by Ryberg and Weber (2000).

Slowness domain receiver functions and the two-term series approximation to the traveltime difference are illustrated in figure 5.5 for the six-layer model from table 5.1. In the top-left panel, the receiver functions resulting from stabilized deconvolution of the wavefield-separated, ($\tau$,p)-transformed data from figure 5.4 (bottom panels) are shown. Notice that only positive lag-times are shown and that the range of lag-times is restricted to 0.8 s. The receiver functions contain a myriad of events and it is not immediately clear which events relate to the PS-converted waves from each interface. To aid the interpretation, in dark blue, the exact traveltime difference as a function of slowness, obtained by raytracing trough the six-layer model, is shown. In light blue, the two-term approximation calculated using equation 5.14 and the exact vertical traveltime difference $dt_0$, and

---

velocity. Notice that at this point the resemblance between our equation 5.14 and the small-spread approximation is merely conceptual. Later on, in section 5.5 we will discuss an example where the resemblance is more acute.

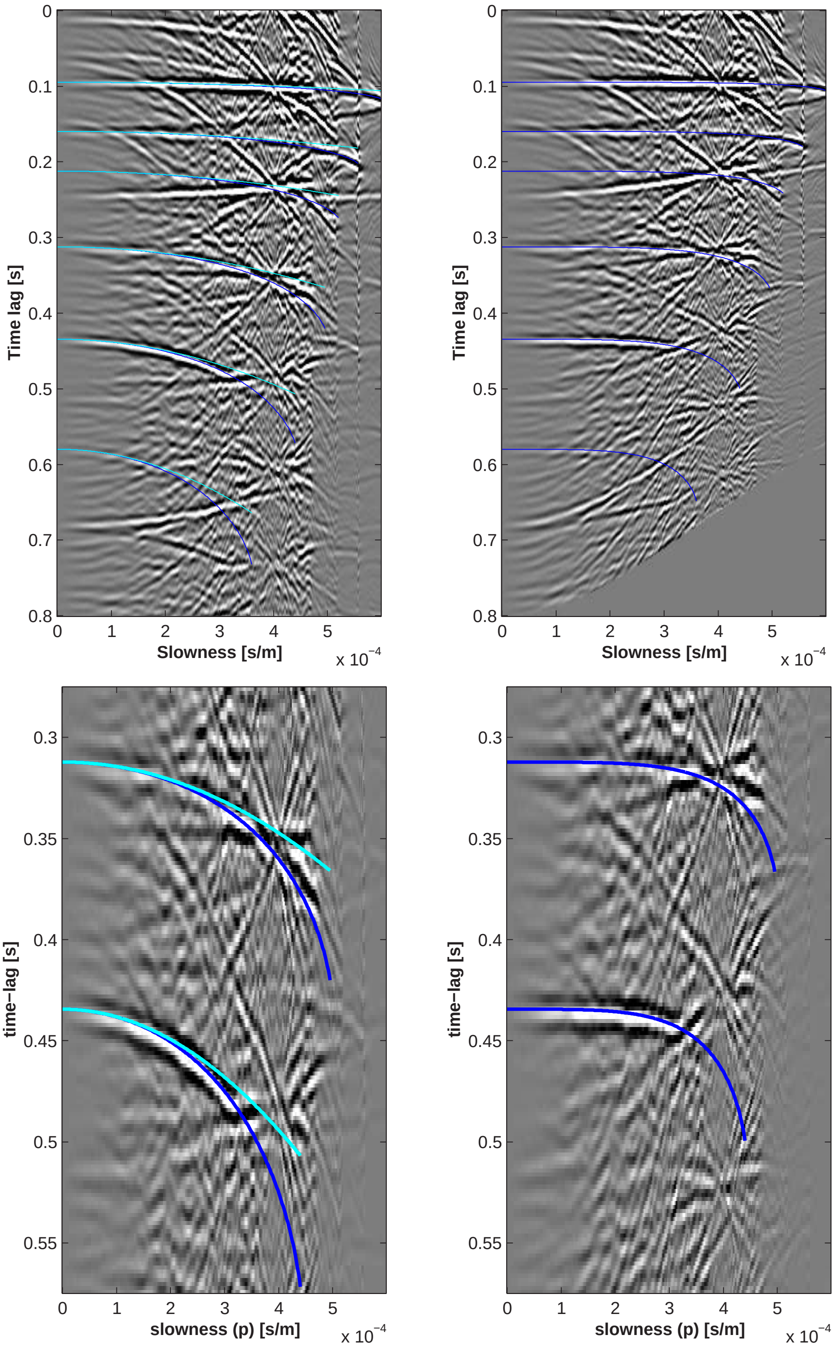

**Figure 5.5:** Slowness domain receiver functions (top-left) and their NMO correction (top-right) for the PS-separated, ($\tau$,p)-transformed reflectivity data from figure 5.4, bottom panels. In blue, the exact traveltime difference as a function of slowness, obtained by raytracing trough the six-layer model, is shown. In light blue, the two-term approximation calculated using equation 5.14 and the exact vertical traveltime difference $dt_0$, and pseudo rms-velocity $\tilde{v}_{rms}$ (equations 5.15 and 5.16) is shown. In the bottom panels, a zoom-in of the top panels is shown.

pseudo rms-velocity $\tilde{v}_{rms}$ (equations 5.15 and 5.16) is shown. Note that the two-term approximation agrees well with the exact traveltime differences for small to medium slowness. In the top-right panel, the result of applying a normal moveout correction, based on the two-term approximation, is shown. Again, exact pseudo rms-velocities were used, but initial tests indicate that these quantities indeed can be derived from semblance-based velocity analysis. In blue, the expected residual moveout is shown.

### 5.4.3 Dix-Krey relations for receiver functions I: Slowness domain expression

At this point we may ask if, given the vertical incidence traveltime differences and the pseudo rms-velocities, we can get back to the medium properties for each individual layer. In reflection seismology this problem is well known and has been solved for P-waves and PS-converted waves reflecting in a horizontally layered medium. Such “inversion” formulae are known as Dix-Krey relations after the work by Dix (1955) and Krey (1954). In Appendix D it is shown that by carrying out a similar analysis as Tessmer and Behle (1988), who derived Dix-Krey-type relations for PS-converted waves, it is straightforward to obtain:

$$Vs_n Vp_n = 2 \cdot \frac{\tilde{v}_{\mathrm{rms}}^{n} - \tilde{v}_{\mathrm{rms}}^{n-1}}{dt_0^n - dt_0^{n-1}}. \tag{5.17}$$

Equation 5.17 says that only the product of P- and S-wave interval velocities in layer $n$ can be resolved and equals twice the ratio of the differences in pseudo rms-velocities and vertical incidence traveltime differences between interface $n$ and $n-1$. Equation 5.17 can easily be checked by substituting the definitions of the vertical incidence traveltime difference and the pseudo rms-velocity (equations 5.15 and 5.16). Readers familiar with the work of Tessmer and Behle (1988) may notice that equation 5.17 has a simpler form than their relation. This is because our approximations of the traveltime difference and rms-velocities are in the slowness domain whereas Dix-Krey-type relations for PS-converted waves are based on rms-velocities in the offset domain.

This concludes the slowness domain treatment. In the next section we discuss an approach which exploits the dense sampling that is typically present in exploration and production seismic surveys and that treats the spatial aspects of mode-conversion completely analogously to the temporal aspects.

## 5.5 Space-time ($x$,$t$) domain treatment

### 5.5.1 Receiver function calculation II: 2D Deconvolution

In the previous sections, the offset between the P-wave transmission point and PS-conversion point at the base of the stack was taken into account implicitly in the derivation of the traveltime difference (equation 5.13). The main, historical reason for this is that it facilitates comparison of P- and PS-wave traveltimes *at a single* multicomponent station. However, when data are recorded on a densely spaced array of receivers (see figure 5.6), the P- and S-waves, reflected and converted at *the same location on an interface*, are recorded, although at spatially offset receiver locations. This makes it possible to treat the spatial separation between PP-reflected and PS-converted waves originating from the same location completely analogously to temporal separation and a 2D deconvolution receiver function can be defined as follows.

Expressing the two-dimensional Fourier transform of $u(x,t)$ and its inverse as

$$\bar{U}(k,\omega) = \int\int_{-\infty}^{\infty} u(x,t)e^{i(wt-kx)}dtdx, \tag{5.18}$$

$$u(x,t) = \frac{1}{(2\pi)^2}\int\int_{-\infty}^{\infty} \bar{U}(k,\omega)e^{-i(wt-kx)}d\omega dk, \tag{5.19}$$

where $k$ denotes the wavenumber along the array, and letting $\bar{Z}(p,\omega)$, $\bar{R}(p,\omega)$ and $\bar{T}(p,\omega)$ denote the vertical, radial and transverse components transformed to the frequency-wavenumber $(\omega,k)$ domain, respectively, then the 2D receiver function is calculated by spectral division as:

$$\bar{H}_R(k,\omega) = \frac{\bar{R}(k,\omega)\bar{Z}(k,\omega)^*}{\bar{Z}(k,\omega)\bar{Z}(k,\omega)^*+\epsilon}, \tag{5.20}$$

$$\bar{H}_T(k,\omega) = \frac{\bar{T}(p,\omega)\bar{Z}(k,\omega)^*}{\bar{Z}(k,\omega)\bar{Z}(k,\omega)^*+\epsilon}, \tag{5.21}$$

with a similar expression for the PS-separated input data. The corresponding $(x,t)$-domain expressions, $h_r(x,t)$ and $h_t(x,t)$, are found by two-dimensional inverse fourier transform of equations 5.20 and 5.21, respectively. Comparing equa-

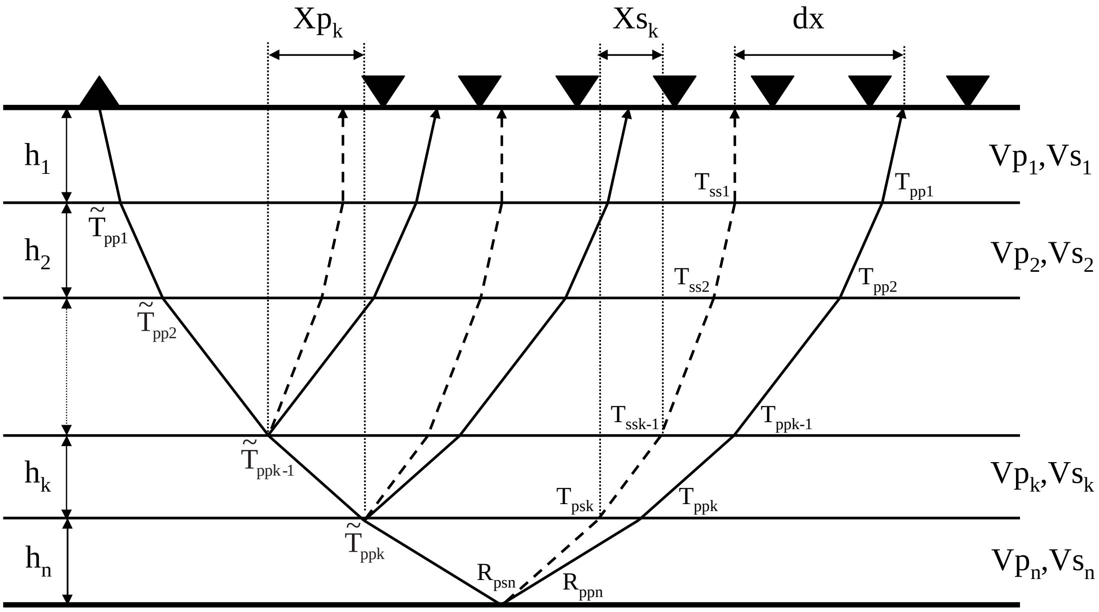

**Figure 5.6:** Schematic illustration of the phases and raypaths involved in the exploration and production seismic receiver function setting. An explosive point source generates a spherically diverging P-wave reflecting and mode-converting at each interface. The PP-reflected and PS-converted waves are recorded on a densely spaced array of receivers. P- and S-waves are denoted by solid and dashed lines respectively. The data from all receivers can be analyzed jointly and, as the PP-reflections and PS-conversions from common points on each interface are recorded at spatially and temporally offset locations, the spatial aspect of mode-conversion can be treated completely analogously to the temporal aspects.

tions 5.20 and 5.21 for the 2D deconvolution receiver functions with equations 5.8 and 5.9 and noting that for any function $\tilde{U}(\omega p, \omega) = \bar{U}(k, \omega)$ it is clear that

$$\bar{H}_R(k, \omega) = \tilde{H}_R(\omega p, \omega), \tag{5.22}$$

$$\bar{H}_T(k, \omega) = \tilde{H}_T(\omega p, \omega). \tag{5.23}$$

Thus, the 2D deconvolution receiver function equals the slowness domain deconvolution receiver function along lines of constant slowness $p = k/\omega$.

An example of a 2D deconvolution receiver function calculated using equation 5.20 is shown in figure 5.7. The events in the receiver function show how much the P-wave data should be shifted, both spatially and temporally, to match the corresponding PS-converted waves. The 2D receiver function relates the P-waves to the PS-converted waves by two-dimensional convolution.

Similar assumptions underpin the 2D receiver function as those discussed in section 5.2 for the slowness domain deconvolution receiver function and hence these will not be repeated here. To extract the information about subsurface structure from the 2D receiver function, again we need approximate expressions for the traveltime difference through a horizontally layered medium. In this case, however, the series expansions are a function of the horizontal offset between the PP-reflected and PS-converted waves instead of slowness since the 2D receiver function presents the temporal shift as a function of that quantity. This is the topic of the next section.

### 5.5.2 Series expansion of the traveltime difference II: Function of horizontal offset

Using elementary trigonometric relations and Snell's law, the explicit difference in traveltime between a plane P- and PS-wave of slowness $p$, transmitted and converted at the same location at the base of layer $n$, can be written (Figure 5.6):

$$dt = \sum_{k=1}^{n} (Ts_k - Tp_k) = \sum_{k=1}^{n} \left[ \frac{h_k}{Vs_k\sqrt{1-p^2Vs_k^2}} - \frac{h_k}{Vp_k\sqrt{1-p^2Vp_k^2}} \right]. \qquad (5.24)$$

Similarly, the offset between the recording locations of a P- and PS-wave, reflected and converted at the same point in the subsurface, can be written:

$$dx = \sum_{k=1}^{n} (Xp_k - Xs_k) = \sum_{k=1}^{n} \left[ \frac{h_k Vp_k}{\sqrt{1-p^2Vp_k^2}} - \frac{h_k Vs_k}{\sqrt{1-p^2Vs_k^2}} \right]. \qquad (5.25)$$

Again, the traveltime difference and horizontal offset in equations 5.24 and 5.25 depend on all unknown medium parameters above the reflection/conversion point. To process the 2D receiver functions in section 5.5.1, the traveltime difference $dt$ should be parameterized as a function of $dx$ with as few parameters as possible. This can be achieved by first writing equations 5.24 and 5.25 as infinite series of increasing powers of slowness by expanding terms of the form $(1-p^2v^2)^{-\frac{1}{2}}$ into

Taylor series. In Appendix E, it is shown that this gives:

$$\begin{aligned} dt &= \sum_{j=1}^{\infty} \gamma_j p^{2j-2}, & (5.26) \\ dx &= p \sum_{j=1}^{\infty} b_j p^{2j-2}, & (5.27) \end{aligned}$$

where the coefficients $b_j$ and $\gamma_j$ are determined by the layer velocities and thicknesses as follows:

$$\begin{aligned} \gamma_m &= q_m a_m., & (5.28) \\ b_m &= -q_m a_{m+1},, & (5.29) \\ a_m &= \sum_{k=1}^{n} h_k \left( Vs_k^{2m-3} - Vp^{2m-3} \right). & (5.30) \end{aligned}$$

Equations 5.26 and 5.27 have the same form as Taner and Koehler (1969) derived for the traveltime and offset of a P-wave reflection in a horizontally layered medium and as Tessmer and Behle (1988) later found for the traveltime and offset of PS-converted waves. This suggests that by applying a similar methodology, it is possible to find an expansion of the square of the traveltime difference into increasing even powers of the horizontal offset $dx$ of the form:

$$dt^2 = c_1 + c_2 \cdot dx^2 + c_3 \cdot dx^4 + c_4 \cdot dx^6 \cdots \tag{5.31}$$

In Appendix E, it is shown that this is indeed the case and it is shown that the first two coefficients of equation 5.31 can be calculated as:

$$\begin{aligned} c_1 &= \left( \sum_{k=1}^{n} h_k \left( \frac{1}{Vs_k} - \frac{1}{Vp_k} \right) \right)^2 \equiv dt_0^2, & (5.32) \\ c_2 &= \frac{\sum_{k=1}^{n} h_k \left( \frac{1}{Vs_k} - \frac{1}{Vp_k} \right)}{\sum_{k=1}^{n} h_k \left( Vs_k - Vp_k \right)} \equiv \frac{1}{v_{rms}^2}. & (5.33) \end{aligned}$$

Note that coefficient $c_1$ (equation 5.32) can be directly interpreted as the square of the difference in traveltime between the P- and PS-converted wave at vertical incidence ($p = 0$ s/m) and hence has been equated to $dt_0^2$. The coefficient $c_2$ can not be interpreted so easily, although the numerator is equal to $dt_0$, but it has the same form as was found by Tessmer and Behle (1988) for PS-converted waves and hence we have equated it to the inverse of the square of an RMS-velocity.

The series expansion of the traveltime difference as a function of the difference in horizontal travel distance is illustrated in figure 5.7 using the 2D deconvolution receiver functions computed previously for the six-layer model. In dark blue, the theoretical traveltime difference as a function of the difference in horizontal traveldistance are shown, computed for each interface using equations 5.24 and 5.25 and the slowness obtained by ray-tracing. In light blue, the two-term approximation calculated using equation 5.31 and the exact vertical traveltime difference $dt_0$, and rms-velocity $v_{rms}$ (equations 5.32 and 5.33) are shown. Note that the two-term approximation agrees well with the exact traveltime differences for small to medium horizontal offsets between the P- and S-waves. In green, successive higher-order approximations are shown. Although the higher-order approximations are more accurate than the two-term approximation, it can be seen that they tend to diverge more quickly as well.

The observed divergent behaviour was recently explained for ordinary PP-reflected waves by Ghosh and Kumar (2002), who showed that this type of series expansions, after Taner and Koehler (1969), of the traveltime (or traveltime difference) through a horizontally medium as a function of the offset (or offset difference) is divergent and hence that adding more terms does not necessarily increase the accuracy. It is astonishing that such a key result, which forms the theoretical basis for velocity analysis in all exploration and production seismic, should prove divergent and that it took more than thirty years to find out. Given the success of two- and three-term velocity analysis in the past, we shall not be discouraged here by the theoretical properties of equation 5.31 and follow a similar route to invert the rms-velocities as followed by Tessmer and Behle (1988) for PS-converted waves. This is the topic of the next section.

### 5.5.3 Dix-Krey relations for receiver functions II: Space-time domain expression

Similarly to the derivation of the Dix-Krey relation for the two-term approximation in the slowness domain, a Dix-Krey-type relation can now be derived for the two-term asymptotic truncation of the series expansion developed in the previous section. Such a relation will again provide the basis for inversion of the rms-velocities (equation 5.33) for medium properties between two consecutive interfaces. The derivation of the relation is presented in Appendix F, here we simply state the result:

$$Vp_n Vs_n = \frac{dt_0^n v_{rms,n}^2 - dt_0^{n-1} v_{rms,n-1}^2}{\left(dt_0^n - dt_0^{n-1}\right)}, \tag{5.34}$$

Equation 5.34 shows how the product of P- and S-wave interval velocities for a layer $n$, can be calculated once the rms-velocities and the vertical incidence time differences for that layer and the previous layer are known. Equation 5.34 has exactly the same form as found previously for PS-converted waves by Tessmer and Behle (1988). Note however that the vertical incidence traveltime differences and rms-velocities are defined differently in their work.

This concludes the treatment of the 2D receiver functions. The results in this and previous sections can be used to moveout-correct and stack both 1D slowness domain and 2D space-time domain receiver functions. In the next section we investigate possibilities of calculating receiver functions when the medium is no longer horizontally layered, but arbitrarily inhomogeneous.

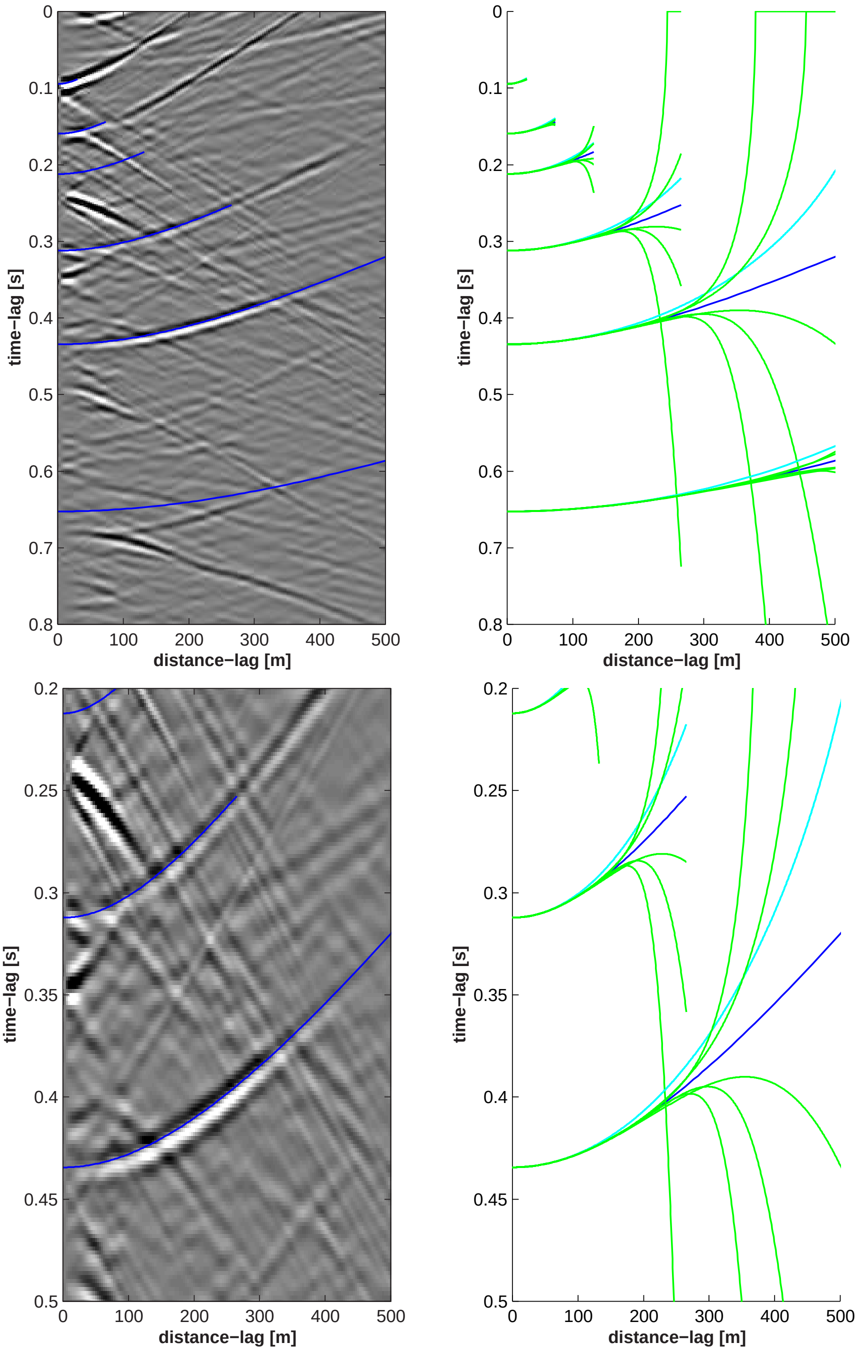

**Figure 5.7:** 2D deconvolution receiver function calculated for the PS-separated, (x,t)-domain input data from figure 5.2 (left panels) and its kinematic behaviour (right panels). In dark blue, the theoretical traveltime difference as a function of the difference in horizontal traveldistance is shown, computed for each interface using equations 5.24 and 5.25 and the slowness obtained by ray-tracing. In light blue, the two-term approximation calculated using equation 5.31 and the exact vertical traveltime difference $dt_0$, and rms-velocity $v_{rms}$ (equations 5.32 and 5.33) are shown. In green, successive higher-order approximations are shown. In the bottom panels, a zoom-in of the top panels is shown.

## 5.6 Model independent treatment

### 5.6.1 Receiver function calculation III: Model independent approach

Slowness domain deconvolution and the 2D approach discussed above work well when the medium is invariant for translation along the horizontal direction since in that case the transfer function characterizing the medium at every slowness, or combination of dt and dx, has a particular form that can be captured theoretically (as was done in the sections on kinematics above). However, when the medium is not horizontally layered, such a simple form does not exist and, in general, there is no one-to-one correspondence between events in the transfer function and PS-waves converted at a particular interface and slowness (or dx-dt)[4].

In this section, I propose an alternative way of calculating a receiver function that is independent of the model and applies to arbitrary inhomogeneous media. The approach is inspired by a method due to Grechka and Tsvankin (2002) to calculate pseudo-shear wave data from PP and PS converted waves. Their method relies on matching the slowness of a PS-converted wave to the slowness of the corresponding PP-wave on the source side and is illustrated in figure 5.8 [after Grechka and Tsvankin (2002), figure 2]. By comparing the reflection slope on the common receiver gather for the PS-converted wave recorded at $x^{(3)}$ to the reflection slope of the PP-wave recorded at $x^{(2)}$ it is found that they are equal for source at location $x^{(1)}$. Therefore, the PP-wave and the PS-converted wave must have left the synthetic source array at $x^{(1)}$ under the same angle, and have reflected and converted at the same subsurface location. By repeating this analysis for the PP-wave and its PS-conversion from a source at $x^{(2)}$ and subtracting and adding the appropriate traveltimes, Grechka and Tsvankin (2002) were able to construct pseudo-shear-wave data with correct offsets and traveltimes. The approach was automated in Grechka and Dewangan (2003) by formulating the procedure as a series of convolutions and crosscorrelations followed by stacking to yield the stationary phase contribution.

A similar approach to calculate receiver functions is to deconvolve (trace-by-

---

[4] To see this, note, e.g., that source and receiver side slowness are no longer necessarily identical for the incident and reflected wavefields.

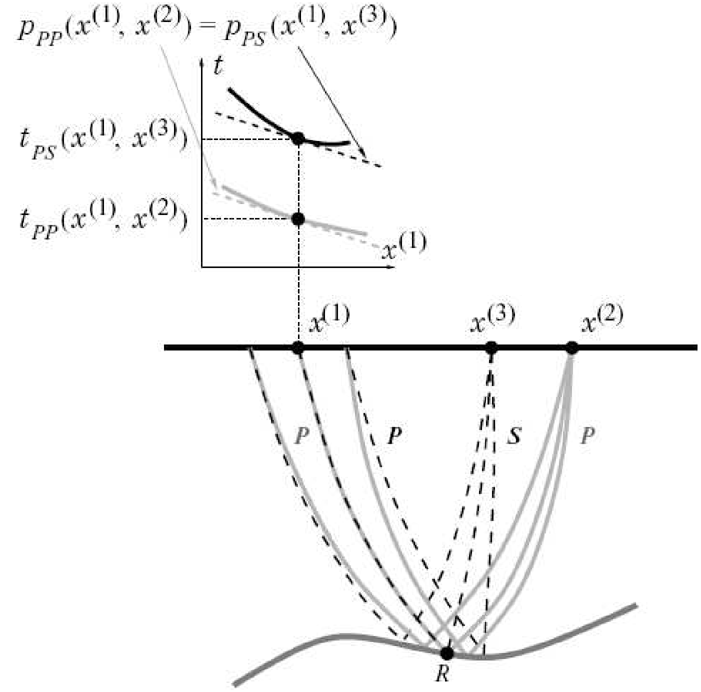

**Figure 5.8:** Model independent receiver function calculation by matching PP- and PS-wave slowness on the source side (after Grechka and Tsvankin, 2002)

trace) all PP-waves in a common receiver gather recorded at, say $x^{(2)}$, from all PS-converted waves recorded at, say $x^{(3)}$. Since the slope of the PP-waves and PS-converted waves is equal at some point $x^{(1)}$, the receiver functions will show a stationary event at $x^{(1)}$ at the corresponding traveltime difference. By stacking these receiver functions, a single function is obtained, giving the true amplitude relation between a PP- and PS-converted wave with that traveltime difference and the horizontal distance $dx = x^{(2)} - x^{(3)}$[5].

This approach is illustrated for a simple model consisting of a single reflector dipping 15 degrees to the right. In figure (5.9), the raypaths are shown for a PP-wave (solid) and PS-wave (dotted) common receiver gather recorded at points $x^{(2)}$ and $x^{(3)}$, respectively. The downgoing P-wave rays overlap for a source at $x^{(1)}$. In figure 5.10(a), the corresponding PP- and PS-wave arrivals are shown, generated by convolving a 30 Hz Ricker wavelet with appropriately delayed unit amplitude spikes. It can be seen that the reflection slopes match at $x^{(1)}$. In

---

[5] With true amplitude, here, we mean to emphasize that since the PP-reflection and PS-conversion point coincide, the deconvolution of the downgoing leg, and all propagation effects associated with it, is complete: the resulting receiver function is a combination only of the PP-reflection and PS-conversion coefficient and the corresponding upgoing paths.

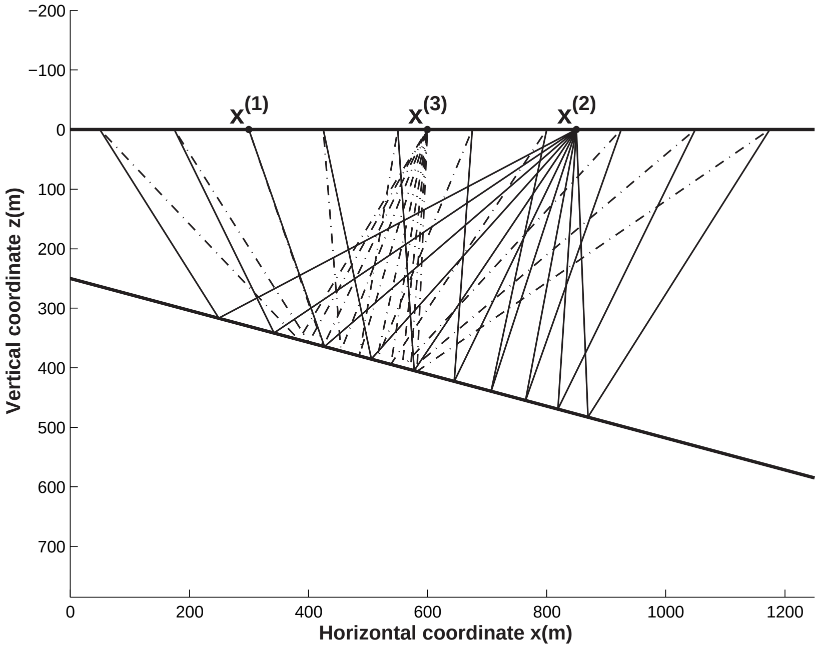

**Figure 5.9:** Raypaths in model independent receiver function calculation for a model consisting of a single layer dipping 15 degrees to the right. PP-wave raypaths (solid) for the common receiver gather recorded at $x^{(2)}$ and PS-wave raypaths (dotted) for the common receiver gather recorded at $x^{(3)}$. The downgoing P-wave rays match at source location $x^{(1)}$.

figure 5.10(b), the receiver functions are shown, calculated by trace-by-trace (1D) deconvolution of the PP- and PS-events in (a). The traveltime difference in the receiver functions is stationary around $x^{(1)}$. By stacking the receiver functions over the horizontal direction, outputting the result at the midpoint in between $x^{(2)}$ and $x^{(3)}$ and repeating this procedure for increasing horizontal differences $dx = x^{(2)} - x^{(3)}$, a common midpoint receiver function gather is obtained that can be further processed to yield an image of the (PS/PP)-reflectivity. Note that by taking $x^{(2)} = x^{(3)}$, i.e., by deconvolving PP- and PS-wave events in common receiver gathers recorded at the same location and stacking the resulting receiver functions, a zero-offset receiver function is obtained[6] that can be migrated in a homogeneous background medium using the pseudo-velocity $(VpVs)/(Vp-Vs)$. In the next section, I show how to migrate non-zero offset receiver functions.

---

[6] Note that in isotropic media no P-S conversion takes place at normal incidence. However, many authors have observed P-S converted waves at or near normal incidence and from a methodological perspective it may still be useful to talk about zero-offset receiver functions.

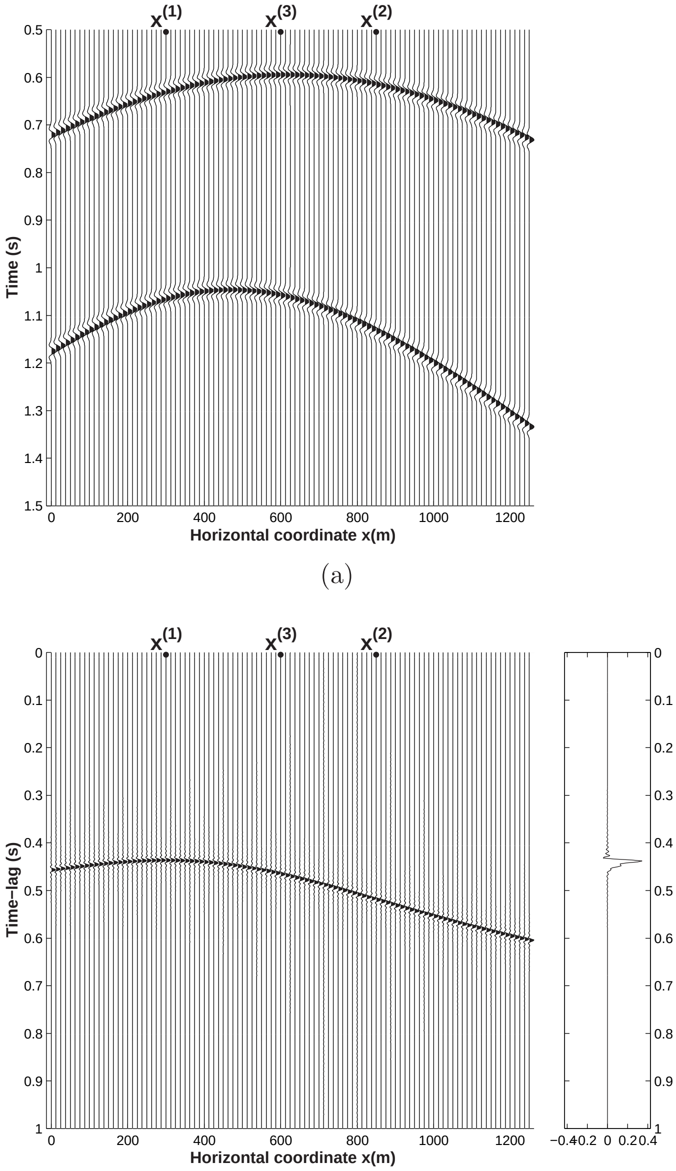

(a)

(b)

**Figure 5.10:** Slope matching in model independent receiver function calculation for a model consisting of single layer dipping 15 degrees to the right. (a) Common receiver gather P-wave data recorded at $x^{(2)}$ (top event) with superimposed the PS-wave data recorded at $x^{(3)}$ (bottom event). The reflection slopes match at a source location $x^{(1)}$. (b) Receiver functions resulting from trace-by-trace deconvolution of the PP- and PS-wave data shown in (a). The traveltime difference is stationary at $x^{(1)}$. A single receiver function is obtained for the points $x^{(2)}$ and $x^{(3)}$ ($dx = x^{(2)} - x^{(3)}$) by stacking the receiver functions over the horizontal coordinate.

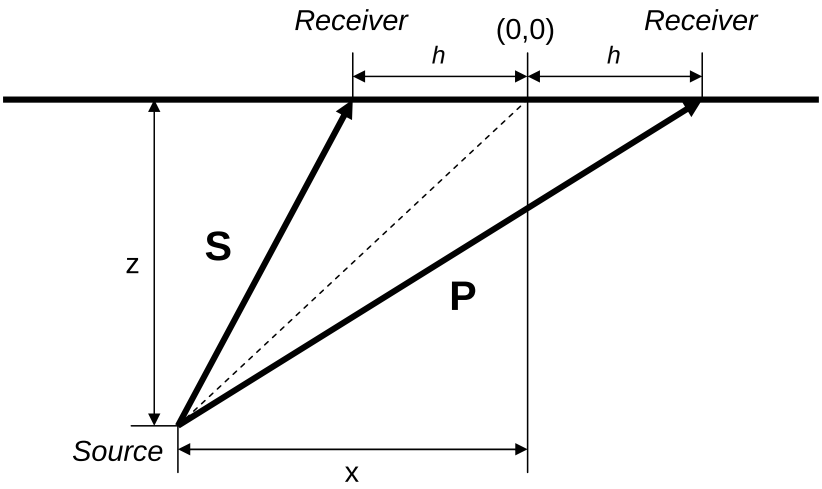

**Figure 5.11:** Raypath geometry for computing the locus of points consistent with an observed traveltime difference in the receiver functions.

## 5.6.2 Pre-stack migration of receiver functions

With the aid of the normal moveout equations and the Dix-Krey type equations presented earlier, receiver functions obtained for plane layered media can, in principle, be moveout corrected and stacked. However, when significant deviations from horizontal layering exist, such a procedure is suboptimal and may result in a significant mispositioning of the events in the receiver functions. In the previous section, a first step towards accommodating such lateral variations was made by showing how model independent receiver functions can be calculated for arbitrary inhomogeneous models. Here we show how such model independent receiver functions can be migrated (pre-stack) by deriving the locus of points from which an event with a certain PS-PP traveltime difference could have originated. In figure 5.11, the relevant geometry is shown. The traveltime difference, $dt_{ps}$, as can be seen from the figure is:

$$dt = \frac{\sqrt{(x-h)^2+z^2}}{\beta} - \frac{\sqrt{(x+h)^2+z^2}}{\alpha}, \tag{5.35}$$

where $\alpha$ and $\beta$ are the P- and S-wave velocities in the medium, respectively. Repeatedly squaring equation 5.35 and after some algebra we find:

$$\left(\frac{\alpha^2-\beta^2}{\alpha\beta}\right)^2 (x^2+h^2+z^2)^2 - 2\frac{(\alpha^2+\beta^2)}{\alpha\beta}\left[\frac{2(\alpha^2-\beta^2)}{\alpha\beta}(xh)+\alpha\beta dt^2\right](x^2+h^2+z^2)$$

$$+\left[\frac{2(\alpha^2-\beta^2)}{\alpha\beta}(xh)+\alpha\beta dt^2\right]^2+16(xh)^2=0. \tag{5.36}$$

This equation is of the form

$$A\epsilon^2+2B(x)\epsilon+C(x)=0 \tag{5.37}$$

which is quadratic in $\epsilon = z^2+x^2+h^2$ and can be solved using the well known formula. This gives:

$$z^2+x^2+h^2=(\alpha^2-\beta^2)^{-2}\left\{(\alpha^2+\beta^2)\left[\alpha^2\beta^2dt^2+2h(\alpha^2-\beta^2)x\right]\right.$$
$$\left.\pm\, 2\alpha^2\beta^2dt\sqrt{\alpha^2\beta^2dt^2+4h(\alpha^2-\beta^2)x}\right\}. \tag{5.38}$$

This equation gives the locus of points $(x,z)$ consistent with the observed traveltime difference $dt_ps$ at half offset $h$ and may be compared with equation 4.24 of Harrison (1992, pg. 63) for the depth migration locus of a PS-converted wave recorded at time $t$ and half offset $h$ converted at a distance $x$ away from the midpoint:

$$z^2+x^2+h^2=(\alpha^2-\beta^2)^{-2}\left\{(\alpha^2+\beta^2)\left[\alpha^2\beta^2t^2+2h(\alpha^2-\beta^2)x\right]\right.$$
$$\left.-\, 2\alpha^2\beta^2t\sqrt{\alpha^2\beta^2t^2+4h(\alpha^2-\beta^2)x)}\right\}. \tag{5.39}$$

Although the equations look virtually the same, the solution sets are quite different. This can be understood by considering the traveltime difference $dt_{pp}$ between two P-waves originating from the same point in depth (i.e., taking $\alpha=\beta=V$ in equation 5.36). This gives:

$$\left(\frac{x}{a}\right)^2-\left(\frac{z}{b}\right)^2=1, \tag{5.40}$$

where

$$a=Vdt_{pp}, \quad \text{and} \quad b=\frac{V\sqrt{dt_{pp}^2-4h^2/V^2}}{2}. \tag{5.41}$$

Equation 5.40 is the equation for a hyperbola with semimajor axis $a$ and semiminor axis $b$ and constitutes the less well known receiver function counterpart (to the best of my knowledge unknown) of the migration ellipse for P-P data.

Thus, although both solution sets belong to the family of conic sections, the curves look fundamentally different. For example, no solution points on the semiminor axis (the line vertically through the midpoint) exist for the hyperbola[7].

As in Harrison (1992), the depth migration curve, equation 5.35, can be converted to a time migration curve by substituting the vertical traveltime difference $dt0$, where

$$dt0 = \frac{z}{\beta} - \frac{z}{\alpha} = z\left(\frac{\alpha-\beta}{\alpha\beta}\right). \tag{5.42}$$

This gives

$$dt0^2 = \frac{1}{(\alpha+\beta)^2}\left[(\alpha^2+\beta^2)\left(dt^2 + 2\frac{(\alpha^2-\beta^2)}{\alpha^2\beta^2}(xh)\right)\right.$$

$$\left. \pm\, 2dt\sqrt{\alpha^2\beta^2 dt^2 + 4(\alpha^2-\beta^2)(xh)}\right] - \left(\frac{\alpha-\beta}{\alpha\beta}\right)(x^2+h^2). \tag{5.43}$$

For the mixed mode receiver functions, as for conventional PS-converted waves, there are no closed form solutions for the raypath depth- and time-migration curves, so equations 5.38 and 5.43 must be solved numerically. In figure 5.12, the solution sets are shown for an offset of $h$=1 km in a medium with $\alpha$=2000 m/s and $\beta$=1000 m/s for various traveltime differences.

### 5.6.3 Model independent approach: Q-deconvolution

To further illustrate the model independent approach and the potential of completely removing the downgoing P-wave leg and all propagation effects associated with it, we now briefly discuss a second example involving anelastic attenuation. In figure 5.13, left panel, a model with a single reflector at 250 m depth and a free-surface at the top is shown. Conventional absorbing boundaries (gray) were included on the remaining sides to truncate the computational domain. The quality factor, $Q$=250, is initially constant throughout the model. Selected primary PP-reflected and PS-converted wave raypaths are shown for a source at (0,0) m and multicomponent receivers distributed along the free-surface.

---

[7] One might speculate on uses of an equation such as eq. 5.40. One application that comes to mind is migration of interferometric data: consider crosscorrelating P-wave recordings from a noise source in the subsurface. The resulting traces contain events at time-lags $dt_{pp}$ and these can be re-positioned through a simple Kirchhoff migration using equation 5.40.

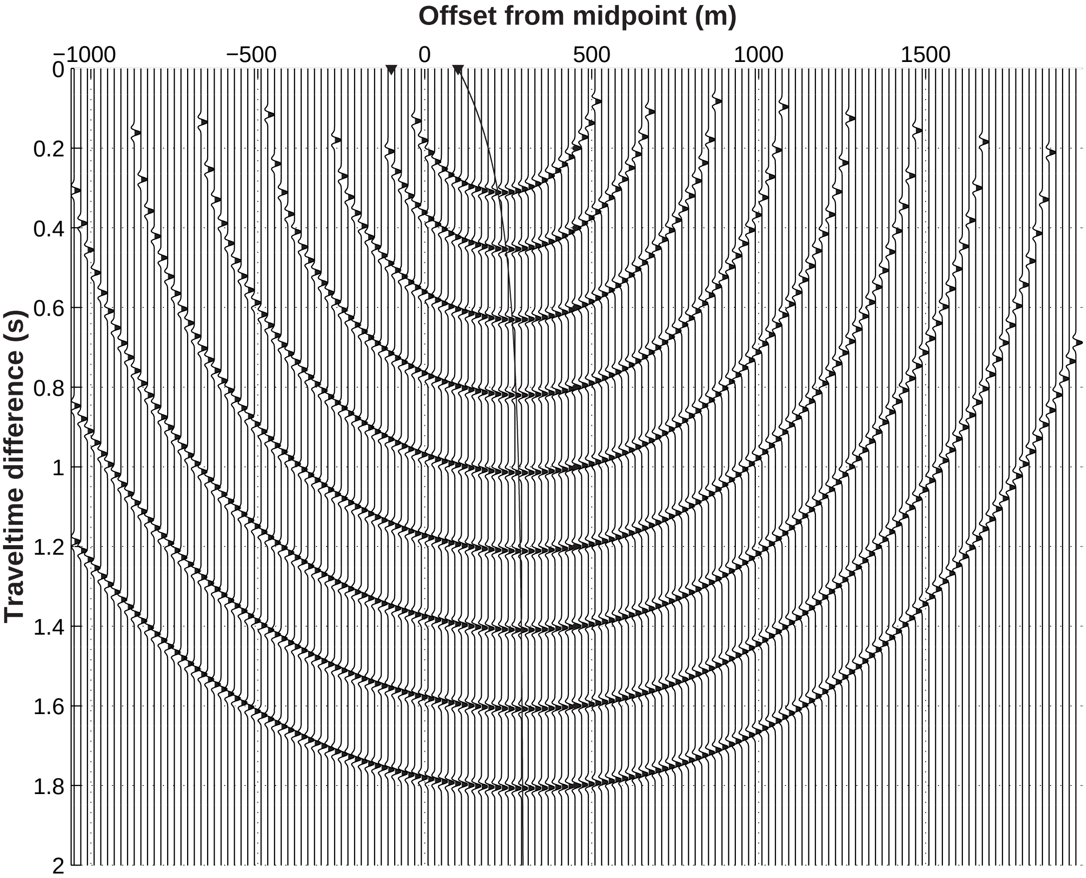

**Figure 5.12:** Receiver function migration curves for a receiver-to-receiver offset of 200 m and various one-way traveltime differences. The solid line denotes the particular solution for which the P- and S-wave slowness with respect to the receiver array are equal. The inverted triangles denote the two receiver locations. A constant amplitude Ricker wavelet of 30 Hz was used to generate this plot.

Data were generated using a viscoelastic finite-difference code (see e.g., Robertsson *et al.*, 1994). In figure 5.14 (top, left) and (top, right), the modeled primary PP-reflected and PS-converted waves are shown, as recorded on the vertical and horizontal components, respectively. The direct wave, free-surface related multiples and the projections of the primaries on the horizontal and vertical component have been muted. These data form the input for our receiver function reference.

Next, the model was perturbed by increasing the attenuation (decreasing the quality factor) to $Q = 50$ in the first layer for the leftmost 75 m of horizontal distance only. The resulting laterally varying Q-model is shown in figure 5.13,

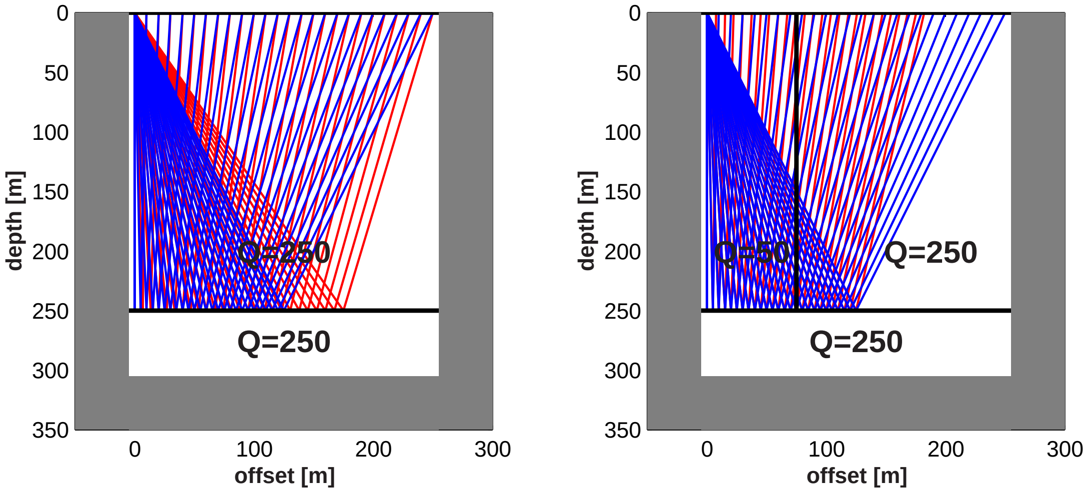

**Figure 5.13:** 2D finite-difference model used to illustrate the removal of increased attenuation associated with the common downgoing P-wave leg. In the left panel, the reference model with homogeneous attenuation (Q=250) is shown. Selected PP-reflected (blue) and PS-converted (red) raypaths arriving at the same receiver are also shown. In the right panel, the model with increased attenuation (Q=50) in the leftmost region is shown. Selected PP-reflected (blue) and PS-converted (red) raypaths with a common reflection/conversion point but arriving at different receivers are also shown. These raypaths experience exactly the same attenuation in the downgoing P-wave leg.

right panel. The apparent difference in raypaths is a matter of choice and explained later. Again, absorbing boundaries were included on the remaining sides, and selected (different) raypaths are shown. The modeled data are shown in figure 5.14 (bottom, left) and (bottom, right) on the same scale as reference data in the top panels. Notice how the increased attenuation in the left-hand side of the model has severely impacted the amplitudes and waveforms of the recorded data across the full offset range.

From the difference between raypaths in the left and right panels of figure 5.13, and our preceding discussion about matching the slowness on the source side, it is clear that in order to completely remove the effects associated with the increased attenuation – experienced (mainly) in the downgoing P-wave leg on the left-hand side – the downgoing raypaths should perfectly overlap. Thus, vertical and horizontal component data from a common reflection and conversion point on the interface should be used in the receiver function calculation.

Although we cannot use the stationary phase approach exactly as outlined in the previous paragraph, since we computed the data only for a single source position, we *can* illustrate the principle of removal of the common downgoing leg using a single trace. In figure 5.15, top panel, the primary PP-reflection at 175 m offset is shown for the model with homogeneous (blue) and heterogeneous attenuation (green). In the 2nd panel, the primary PS-converted wave from the same reflection point is shown (recorded at offset 129 m), again for homogeneous (blue) and heterogeneous (green) attenuation. In the third panel, the receiver function, calculated using 1D stabilised deconvolution is shown for the homogeneous (blue) and heterogeneous (green) attenuation. Perhaps surprisingly, the amplitudes and waveforms match (no additional scaling or filtering has been applied)! Thus, even though the waves in the perturbed model suffered significantly higher attenuation, this attenuation is removed because it is common between the PP-reflected and PS-converted wave. The bottom three panels, resulting from Fourier transforming the top three panels to the temporal frequency domain, again confirm these observations: while the amplitude spectra of the PP- reflected and PS-converted waves (green) are significantly attenuated compared to the data modeled for the homogeneous attenuation (blue), the resulting receiver function amplitude spectra in the bottom panel are almost identical.

Notice that, although we have illustrated the removal of attenuation associated with the downgoing P-wave leg, other propagation effects experienced in the downgoing P-wave leg, such as internal and free-surface related multiples, would also have been removed when calculating the receiver function in the model independent manner.

This concludes the treatment of model independent receiver functions. It is anticipated that the kinematic processing of receiver functions given above can be extended along the same lines as the kinematic development of PS-converted waves, drawing heavily on the work by Harrison (1992). For instance, the traveltime expressions for post-stack migration of PS-converted waves in horizontally layered media derived by Eaton *et al.* (1991) contain sums of down- and upgoing, P- and S-wave legs, respectively. Re-deriving these expressions for traveltime differences between P- and S-wave legs appears straightforward, although the physical interpretation of zero-offset receiver functions (as with PS-converted waves) may be questionable.

We will not follow this route here. Instead, we focus on a more pressing problem that plagues reflection receiver function calculation: while we have shown that the kinematic interpretation and processing of reflection receiver functions is straightforward and does not present any fundamental differences compared to transmission receiver functions, the same is not true for dynamics (i.e., amplitudes). In the next section, starting using a simple two-layer example, we will show that no simple transfer function exists between all joint pairs of PP-reflected and PS-converted waves. Although the reflection receiver function can be generalized to a reflection receiver transfer matrix using a non-stationary filter model, the sheer number of unknowns will prevent calculation without a-priori information.

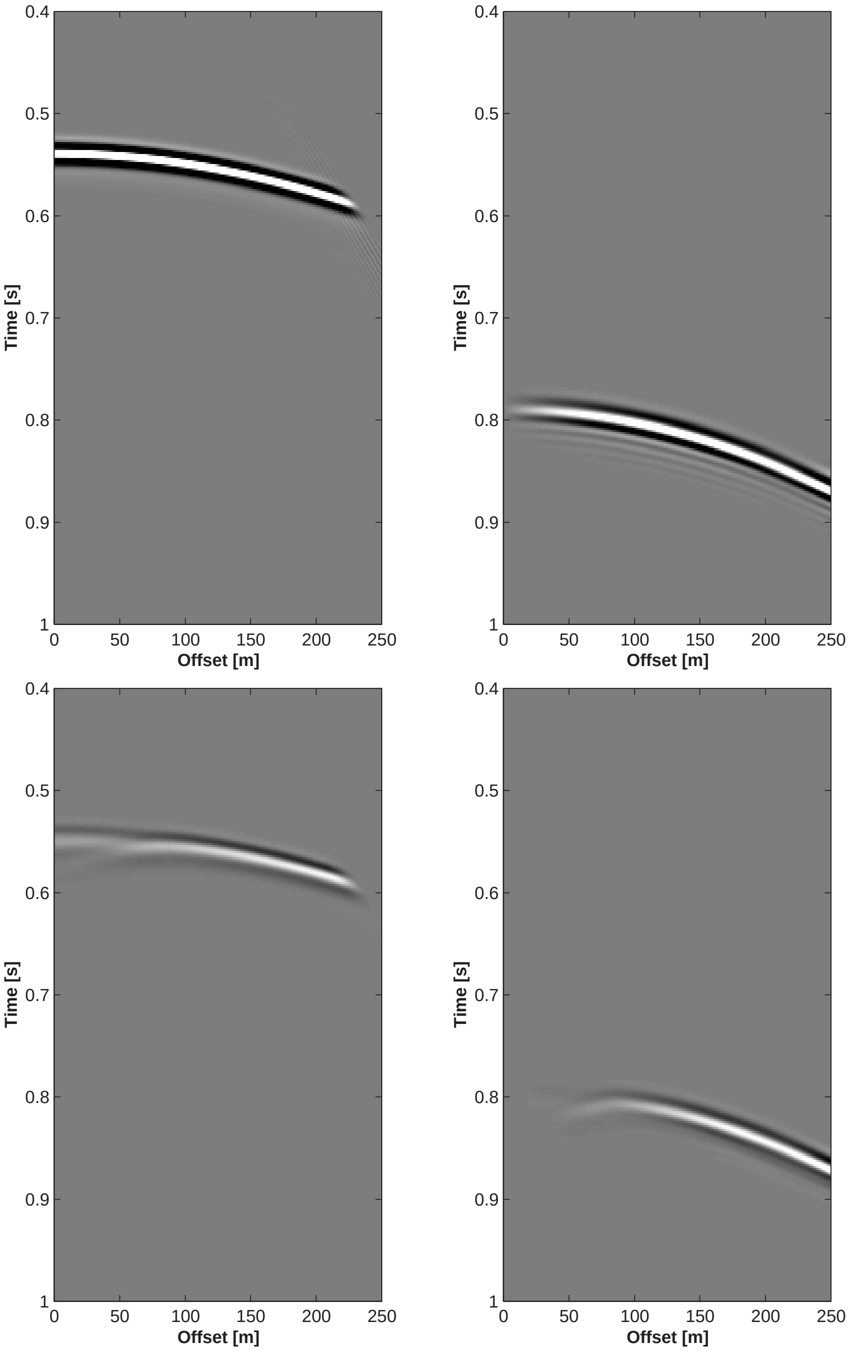

**Figure 5.14:** Finite-difference data computed for the anelastic models in figure 5.13. In the top panels, the PP- and PS-wave primary reflections are shown, as recorded on the vertical and horizontal components, respectively, computed for the model with homogeneous attenuation (Q=250). Note that the direct wave, free-surface related multiples and projections on the other component have been muted. In the bottom panels, the same events for the model with increased attenuation (Q=50) in the left-hand side is shown. Note the severe attenuation of the PP-reflected and PS-converted wave for the full range of receivers.

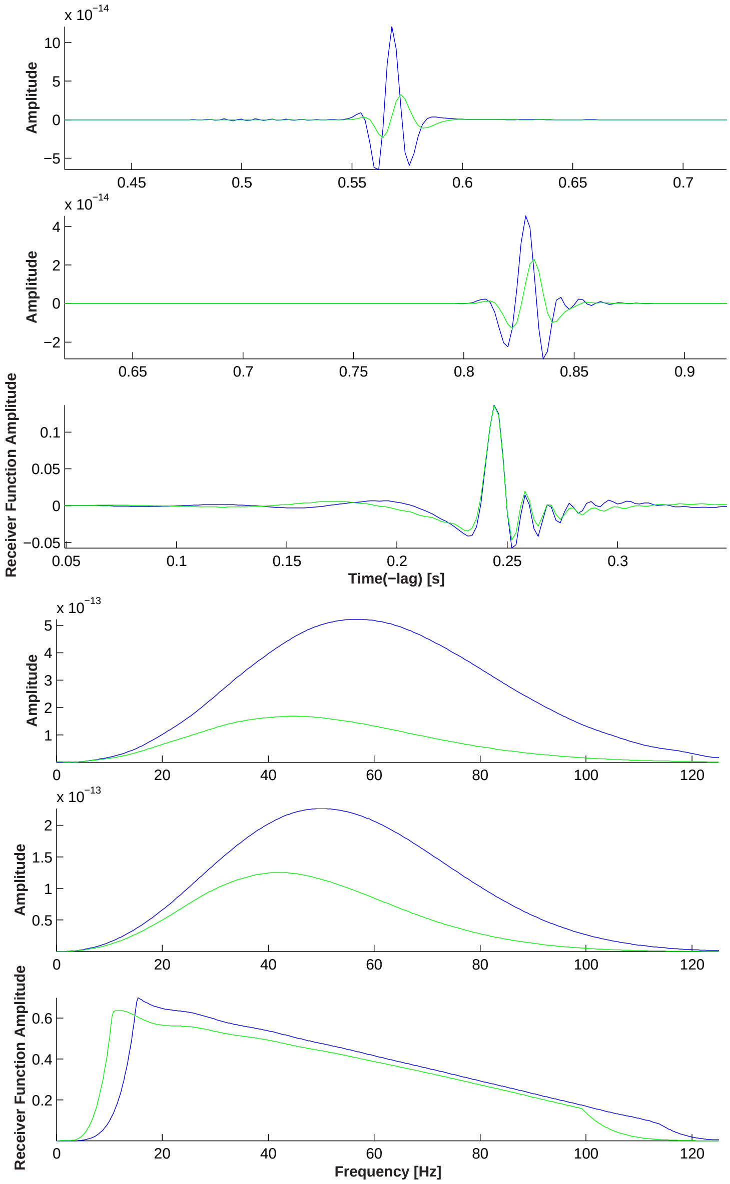

**Figure 5.15:** Receiver functions (time- and frequency-domain) computed for the (x,t)-domain input data from figure 5.14. In the top panel, the primary PP-reflection at 175 m is shown for the model with homogeneous (blue) and heterogeneous (green) attenuation. Similarly, in the second panel, the PS-reflection at 129 m, from the same subsurface reflection point is shown. In the third panel, the time-domain receiver functions obtained by deconvolution of the traces in the top panels are shown for homogeneous (blue) and heterogeneous (green) attenuation. In the bottom three panels, the corresponding amplitude spectra of the top three panels are shown, respectively. Note that despite the severe attenuation in the downgoing P-wave leg for the heterogeneous model, the receiver function is the same as for the model with homogeneous attenuation.

## 5.7 Dynamic development

As visual inspection of the receiver functions computed for the horizontally layered model in sections 5.4 and 5.5 already showed, the receiver functions contain a lot of spurious events that do not correlate with traveltime difference curves computed for PS-conversion upon reflection at the different known interfaces. Here, I will show with a simple two layer example that this is because of fundamental differences between receiver function calculation in reflection-seismic and transmission settings.

In global seismology the receiver function method is typically applied to teleseismic body waves that convert at intra-crustal or upper-mantle discontinuities (e.g. Paulssen *et al.*, 1993; Gurrola *et al.*, 1994). Hence, the original receiver function setting is almost exclusively a *transmission* setting. On the other hand, most mode-converted waves recorded in a surface seismic experiment have converted upon *reflection* at discontinuities in the model (Rodriguez-Suarez *et al.*, 2000).

### 5.7.1 A simple two layer example

To investigate the differences between a transmission and a reflection setting, I consider a horizontally layered model consisting of only two layers and calculate receiver functions for a transmission and reflection setting analytically. To make the problem tractable, internal and free-surface related multiples are ignored and only primary P-waves and singly mode-converted waves are considered[8]. It is also assumed that pure-mode transmission coefficients can be neglected in both settings. The geometry of the problem is shown in figure 5.16.

#### The transmission receiver function

Let $R_t(\omega)$ denote the radial component transmission seismogram recorded due to a plane P-wave incident on a two layer medium (overlying a halfspace) from below. $Z_t(\omega)$ denotes the corresponding vertical component seismogram. We assume that wavefield separation has been applied and that the vertical component only contains P-waves, and the radial component only PS-converted waves. The

---

[8] It was confirmed that these initial assumptions do not affect the general conclusion that in general no simple transfer function exists between reflected P- and S-waves.

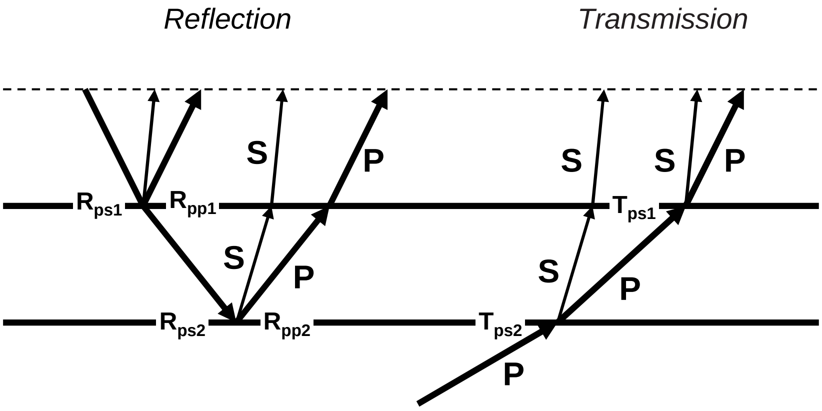

**Figure 5.16:** Two layer geometry for analytical receiver function calculation.

source-time function of the plane P-wave is taken to be a delta-function. If internal and free-surface related multiples are neglected, as well as multiple mode-conversions, $R_t(\omega)$ and $Z_t(\omega)$ can be written (in the frequency domain):

$$R_t(\omega) = T_{ps1} \cdot T_{pp2} \cdot e^{-i\omega(t_{s1}+t_{p2})} + T_{ss1} \cdot T_{ps2} \cdot e^{-i\omega(t_{s1}+t_{s2})}, \tag{5.44}$$

$$Z_t(\omega) = T_{pp1} \cdot T_{pp2} \cdot e^{-i\omega(t_{p1}+t_{p2})}, \tag{5.45}$$

where the $T_{pp1}$'s and $T_{ps2}$'s denote the transmission and conversion coefficients at the two layers and the dependence on slowness has been suppressed for notational convenience. The $t_p$ and $t_s$'s denote the one-way P- and S-wave traveltimes through each of the two layers respectively. The transmission receiver function, $H_t(\omega)$ is defined as the spectral ratio of the radial and the vertical component:

$$H_t(\omega) = \frac{R_t(\omega)}{Z_t(\omega)} = \frac{T_{ps1} \cdot T_{pp2} \cdot e^{-i\omega(t_{s1}+t_{p2})} + T_{ss1} \cdot T_{ps2} \cdot e^{-i\omega(t_{s1}+t_{s2})}}{T_{pp1} \cdot T_{pp2} \cdot e^{-i\omega(t_{p1}+t_{p2})}} \tag{5.46}$$

In the seismological literature, it has been argued (e.g. Langston, 1979) that the pure-mode transmission coefficients $T_{pp1}$, $T_{pp2}$, $T_{ss1}$ etc. can be neglected in the context of receiver function studies, where a teleseismic P-wave is near-vertically incident on the crust from below. Hence, the P-wave is recorded almost unperturbed on the vertical component. In addition, we can define transfer functions $H_{t1}(\omega)$ and $H_{t2}(\omega)$, predicting the amplitude and phase of the PS-converted waves on the radial component due to the P-wave on the vertical:

$$
\begin{aligned}
H_{t1}(\omega) &\equiv T_{ps1} \cdot e^{-i\omega(t_{s1}-t_{p1})}, &(5.47)\\
H_{t2}(\omega) &\equiv T_{ps2} \cdot e^{-i\omega(t_{s1}+t_{s2}-t_{p1}-t_{p2})}, &(5.48)\\
Z_t(\omega) &\approx e^{-i\omega(t_{p1}+t_{p2})}. &(5.49)
\end{aligned}
$$

$H_{t1}(\omega)$ and $H_{t2}(\omega)$ can be regarded as partial receiver functions for each layer, making up the total transmission receiver function for the stack of the layers, as will be clear by substitution into equation 5.46:

$$
H_t(\omega) = \frac{R_t(\omega)}{Z_t(\omega)} \approx \frac{H_{t1}(\omega)Z_t(\omega) + H_{t2}(\omega)Z_t(\omega)}{Z_t(\omega)} = H_{t1}(\omega) + H_{t2}(\omega). \qquad (5.50)
$$

Hence, in the transmission setting, under the aforementioned assumptions, the total receiver function is simply the sum of the partial receiver functions for each individual layer. Note that the time difference between a P- and PS-converted wave from a particular interface is integrated (summed) through all the layers above that interface and the amplitude of the event is, to first order, the PS-conversion coefficient of the interface. This remains valid for more complicated horizontally layered models with more than two layers.

### The reflection receiver function

Next we consider the same two layer medium, under the same assumptions of no internal and free-surface related multiples, and neglecting again transmission coefficients of order one. Let $R_r(\omega)$ and $Z_r(\omega)$ denote the radial and vertical component seismograms, due to a plane P-wave source at the free-surface. In this case, the primary PS-converted waves (converted upon reflection) on the radial and the P-reflections on the vertical can be written:

$$
\begin{aligned}
R_r(\omega) &= R_{ps1} \cdot e^{-i\omega(t_{s1}+t_{p1})} + T_{ss1} \cdot R_{ps2} \cdot \tilde{T}_{pp1} \cdot e^{-i\omega(t_{s1}+t_{s2}+t_{p2}+t_{p1})}, &(5.51)\\
Z_r(\omega) &= R_{pp1} \cdot e^{-i\omega(2t_{p1})} + T_{pp1} \cdot R_{pp2} \cdot \tilde{T}_{pp1} \cdot e^{-i\omega(2(t_{p2}+t_{p1}))}, &(5.52)
\end{aligned}
$$

where the $R_{ps1}$'s and $T_{ps2}$'s denote reflection and transmission coefficients respectively. The $\tilde{}$ serves to distinguish transmission coefficients from above from transmission coefficients from below. Again, the slowness dependence is suppressed in the notation because we consider a single set of plane-waves with equal slowness. Note that the $t_{s1}$'s etc. are exactly the same as those considered in the transmission setting, i.e., kinematically, the reflection and transmission setting are completely equivalent. Neglecting the single-mode transmission coefficients, we can define the approximate P-reflection from each layer on the vertical component $Z_{r1}(\omega)$ and $Z_{r2}(\omega)$ and transfer functions $H_{r1}(\omega)$ and $H_{r2}(\omega)$:

$$\begin{aligned} Z_{r1}(\omega) &\equiv R_{pp1} \cdot e^{-i\omega(2t_{p1})}, && (5.53) \\ Z_{r2}(\omega) &\equiv R_{pp2} \cdot e^{-i\omega(2(t_{p1}+t_{p2}))}, && (5.54) \\ H_{r1}(\omega) &\equiv \left(\frac{R_{ps1}}{R_{pp1}}\right) \cdot e^{-i\omega(t_{s1}-t_{p1})}, && (5.55) \\ H_{r2}(\omega) &\equiv \left(\frac{R_{ps2}}{R_{pp2}}\right) \cdot e^{-i\omega(t_{s1}+t_{s2}-t_{p1}-t_{p2})},. && (5.56) \end{aligned}$$

Again, the transfer functions $H_{r1}(\omega)$ and $H_{r2}(\omega)$ can be understood as partial receiver functions, relating to the PS-conversion at each of the two interfaces, predicting the converted wave signal on the radial component from the separate signals $Z_{r1}(\omega)$ and $Z_{r2}(\omega)$ on the vertical component. Thus, using these definitions the approximate reflection receiver function can be written:

$$H_r(\omega) = \frac{R_r(\omega)}{Z_r(\omega)} \approx \frac{H_{r1}(\omega) \cdot Z_{r1}(\omega) + H_{r2}(\omega) \cdot Z_{r2}(\omega)}{Z_{r1}(\omega) + Z_{r2}(\omega)}. \quad (5.57)$$

This expression for the approximate reflection receiver function should be compared with the corresponding approximate transmission receiver function for the same two layer medium (equation 5.46). Note that, as in the transmission seismic setting, we would have liked to have obtained a receiver function, simply containing a sum of the partial receiver functions $H_{r1}(\omega)$ and $H_{r2}(\omega)$ because in such a case the events in the receiver function are simply interpretable as ratios of P-wave and PS-wave reflection coefficients at each interface and integrated time-delays through the layered structure above it. What we have obtained, however, is more complicated because it consists of a division by the sum of two terms in the frequency domain, instead of a single term as in the transmission setting.

Since we are interested in the partial receiver functions, as they give information about each interface separately, the reflection receiver function presents a much harder dataset from which to extract this information than the transmission receiver function. This is because the vertical component now contains two primary reflections: while between each event in a pair a well defined transfer function exists, in general no simple, causal transfer function exists between two pairs of independently scaled seismic wavelets. As a consequence, the reflection receiver function now consists of an infinite number of peaks with distorted amplitudes. This amplitude distortion is discussed in detail in Appendix G, where also a series approximation to the reflection receiver function is presented.

To illustrate the complexity of even a two-layer receiver function in a reflection setting, we have performed a simple numerical experiment corresponding to the two-layer (over a halfspace) reflection seismic setting discussed above (i.e., equation 5.57). In figure 5.17 (top), wavefield-separated vertical and radial component data (in blue and red, respectively) are shown for the case that the P-wave reflection coefficient at the second interface is lower than the reflection coefficient at the first interface. In the 2nd panel, the corresponding receiver functions, calculated by stabilised deconvolution (green), as well as the five-term approximation from Appendix G (blue), and the desired partial receiver functions (red) are shown. Note that the receiver function contains a lot of unwanted events and that only one of the events matches a partial receiver function. In the 3rd panel, vertical and radial component data are shown for the case that the P-wave reflection coefficient at the second interface is higher than the reflection coefficient at the first interface. In the bottom panel, again, the resulting receiver functions (green), as well as a five-term approximation (blue), and the partial receiver functions (red) are shown. The receiver function is now even a-causal and, hence, unphysical as it contains a lot of energy before time-lag zero, implying that the slower S-wave precedes the arrival of the P-wave.

Notice that the analytical approximations, developed in Appendix G, match very well the stabilised deconvolution results and give insight into the complication that is introduced by additional P-events on the vertical component. It is an open question how serious this difference between the reflection and transmission setting is for real data, which contains many more than two layers. A further discussion on the differences between reflection and transmission and this two-layer example is included at the end of Appendix G.

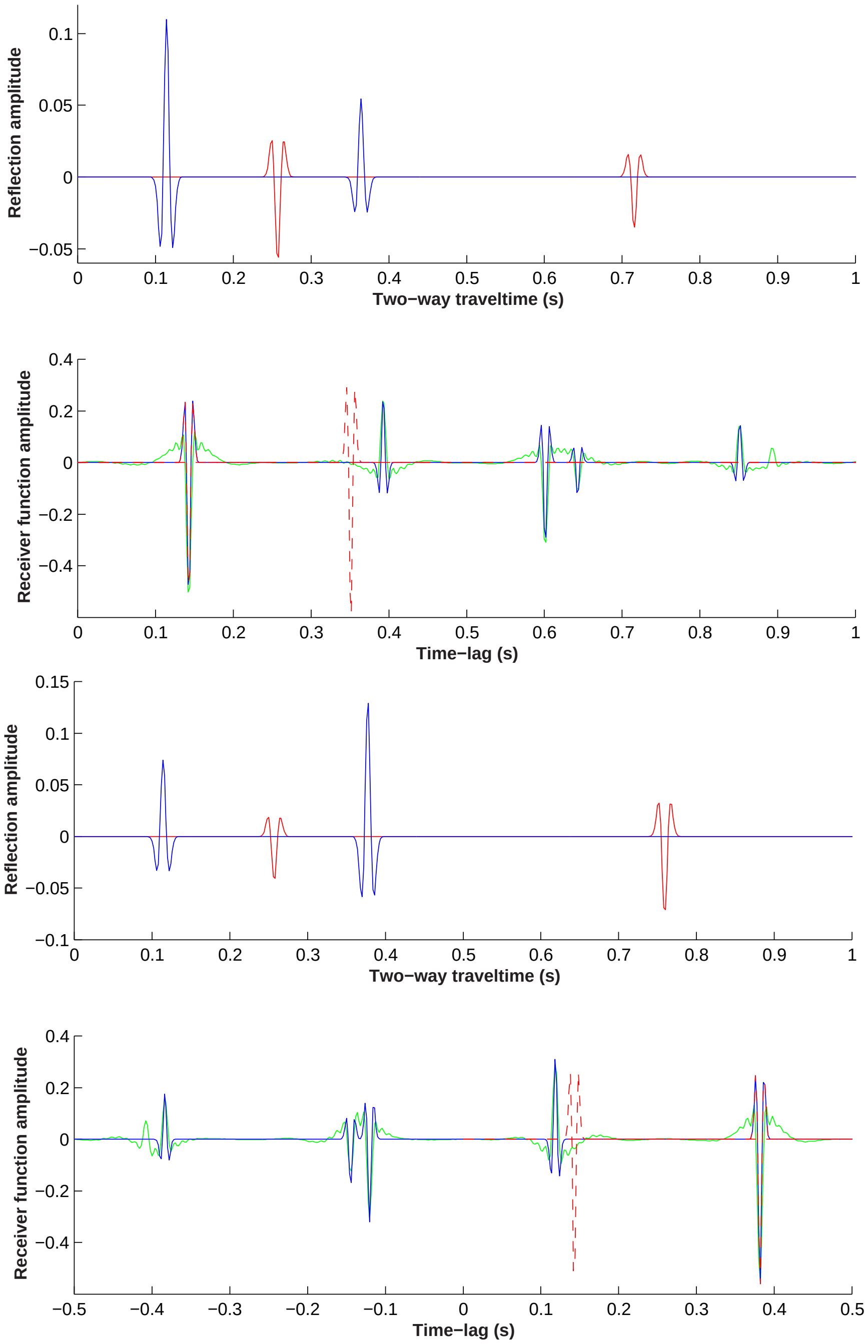

**Figure 5.17:** Receiver function calculation in a simple two layer medium. (top) Vertical and horizontal component reflection data (blue and red, respectively) when $R_{pp1} > R_{pp2}$. (2nd from top) Receiver function calculated by stabilised deconvolution (green, $c = 0.01$, $a = 125$ Hz) of the vertical and horizontal component data in the top panel and a five-term analytical approximation (blue). (3rd from top) Vertical and horizontal component reflection data (blue and red, respectively) when $R_{pp1} < R_{pp2}$. (bottom) Receiver functions calculated by stabilised deconvolution (green, $c = 0.01$, $a = 125$ Hz) of the vertical and horizontal component data in the third panel and a five-term analytical approximation (blue). For details, see text.

### 5.7.2 A model for the reflection receiver function

We have seen in the previous section that receiver functions calculated for reflection seismic data do not have the desirable property of maintaining a single event per interface, which transmission receiver functions do. This is because of the absence of a simple convolutional model between the P- and PS-converted waves for the reflection seismic setting. As a consequence, some of the events relating to a particular interface may be absent in the reflection receiver function or have perturbed amplitudes. In addition, spurious noise events are introduced.

To be useful and interpretable, the reflection receiver function has to be cleaned up, or perhaps, calculated by some other procedure. Ad hoc techniques, based on, e.g., simultaneous windowing of the P- and PS-wave data and an initial receiver function estimate can be tuned to work for certain simple models, but are likely to fail on more realistic models. One of the main problems with such an approach is the inherent assumption of a limited number of layers in the model, with sufficient two-way traveltimes to record the P- and PS-converted waves from each interface without interference from other layers.

Layer stripping or dynamic deconvolution methods (e.g., Claerbout, 1976; Robinson, 1982; Yagle and Levy, 1984, 1985; Bregman *et al.*, 1985; Carazzone, 1992) are in principle most powerful as they have the ability to strip away all effects due to an overlying layer, which will make iterative receiver function calculation for deeper layers more correct. However, they are notoriously unstable and seem overly complex for the purpose that we are considering here.

In this section, we briefly explore an alternative model for the reflection receiver function that is based on the theory of non-stationary filtering. The standard convolutional model for PP- and PS-waves, based on a source wavelet that does not change with depth (i.e., is stationary), does not solve the problem of multiple events on the vertical. On the other hand, a non-stationary but elastic model, in itself, is not general enough to deliver the expected advantages from receiver function calculation such as the removal of common propagation effects such as anelastic attenuation. Even a constant-Q model requires a non-stationary convolutional model to describe the increasingly attenuated source pulse with depth or two-way traveltime (Margrave, 1998).

Separation of the non-stationary Q-filters for downgoing (P) and upgoing

(P/S) waves leads naturally to a time-variant deterministic deconvolution procedure with similar advantages as seismological receiver function calculation. Since the increasingly attenuated downgoing incident wavelet is the same for the PP- and PS-wave models, it can be removed. Another question is how the PP and PS arrival times are reconciled in such a model and events are correlated. As shown below, PP/PS matching (see e.g., Gaiser, 1996) can be described as another time-variant filtering operation, since it involves stretching of the PP-wave trace. However, this will affect the spectra of the stretched trace. Finally, after inverse-Q filtering and stretching the PP-waves to PS-wave times, they need to be forward Q-filtered to match the frequency content of the PS-waves. As the model combines three steps that can all be formulated in terms of non-stationary filtering (inverse Q-filtering, time-stretching, and forward Q-filtering), the resulting model is also non-stationary.

We start by briefly reviewing the theory of non-stationary filtering (Margrave, 1998). The similarity principle, relating the spectra of the stretched and the original trace, is also discussed. The three elements are then illustrated with a simple example, before ending with a discussion and some conclusions.

### Non-stationary filtering

Non-stationary filtering has been described in detail by Margrave (1998). We only briefly review the theory here that is relevant to our application. Since we want to preserve the inverse Q-filtering aspect of receiver function calculation, it seems reasonable to start with a constant Q model. Note that even though we are dealing with constant Q, the increasing attenuation with depth (or traveltime) requires a non-stationary filter model.

**Constant Q filtering** Constant Q filtering is most easily described using the mixed domain formulation of non-stationary filtering (Margrave, 1998). The mixed domain formulation relates the frequency spectrum, $G(f)$, of the non-stationary filtering result to the time-domain input trace, $h(\tau)$, as follows:

$$G(f) = \int_{-\infty}^{\infty} \overline{a}(f,\tau)h(\tau)e^{-2\pi i f\tau}d\tau. \tag{5.58}$$

where $\overline{a}(f,\tau)$ denotes the non-stationary filter in the frequency-time domain. Attenuation can be described if we assume the following form for $\overline{a}(f,\tau)$:

$$\overline{a}(f,\tau) = e^{-\pi\alpha(t,f)+i\phi(t,f)}, \tag{5.59}$$

where $\alpha(t,f)$ is a generalized non-stationary attenuation function, and $\phi(t,f)$ is the phase associated with the attenuation (Schoepp, 1997). If $\alpha(t,f) = 1/Q(t)$, the attenuation becomes the constant Q model. To satisfy the minimum phase requirements the phase is usually calculated by taking the Hilbert transform, $H$, (over frequency) of the natural logarithm of the amplitude spectrum: $\phi(t,f) = H(-\pi\alpha(t,f))$. The time-domain non-stationary filter matrix $a(t,\tau)$ can be simply found by inverse Fourier transforming over the remaining frequency axis.

**Inverse Q-filtering** A similar non-stationary filter model was used by Schoepp and Margrave (1997) to remove the effects of constant Q-attenuation in a procedure referred to as time-variant spectral inversion. This procedure estimates the continuously changing wavelet by smoothing time-variant spectra. Once the time-variant wavelets have been found, stabilized inverses of them are calculated. The stabilized inverses are then applied in exactly the same manner as the time-variant forward-Q filter.

**Squeezing and stretching and the similarity principle** Squeezing of the PS-converted wave trace to P-wave times (and stretching of the P-wave trace to PS-wave times) can be simply described as another time-variant filter operation: a non-stationary phase-shift. Let the relation between input and output times $\tau$ and $t$ be denoted by some general function $s$ [i.e., $t = s(\tau)$], then non-stationary filtering of a trace $h(t)$ requires evaluation of the following integral:

$$g(t) = \int_{-\infty}^{\infty} \delta(t - s(\tau))h(\tau)\mathrm{d}\tau. \tag{5.60}$$

Defining a new integration variable $\overline{\tau} = s(\tau)$, and using the sifting property of the delta function it is straightforward to show that:

$$g(t) = \frac{h(s^{-1}(t))}{s'(s^{-1}(t))}. \tag{5.61}$$

where $s'(\tau) = \frac{\mathrm{d}s(\tau)}{\mathrm{d}\tau}$ and $s^{-1}(\overline{\tau})$ denotes the inverse of the stretching function. In order to interpret this formula, consider the case of uniform stretching: $s(\tau) = m\tau$, with $m$ a constant. Since $s'(\tau) = m$ and $s^{-1}(\overline{\tau}) = \frac{\overline{\tau}}{m}$, we find:

$$g(t) = \frac{1}{m}h(\frac{t}{m}) \tag{5.62}$$

To see how the spectrum of the stretched trace is affected, take the Fourier transform of equation 5.61 over the output time axis, $t$:

$$G(f) = \int\limits_{-\infty}^{\infty} \left[ \int\limits_{-\infty}^{\infty} \delta(t - s(\tau))h(\tau)\mathrm{d}\tau \right] e^{-2\pi i f t}\mathrm{d}t. \tag{5.63}$$

Changing the order of integration, and defining a new integration variable $t' = t - s(\tau)$, it is straightforward to show that:

$$G(f) = \int\limits_{-\infty}^{\infty} h(\tau)e^{-2\pi i f s(\tau)}\mathrm{d}\tau. \tag{5.64}$$

For uniform stretching, $s(\tau) = m\tau$, this can be recognised as the Fourier transform of $h(t)$, denoted $H(f)$, sampled at frequencies $mf$ instead of $f$:

$$G(f) = H(mf) \tag{5.65}$$

Combining equations 5.62 and 5.65, we find:

$$\frac{1}{m}h(\frac{t}{m}) \Longleftrightarrow H(mf). \tag{5.66}$$

This is the so-called similarity principle (Bracewell, 1965). If $H(f)$ is the spectrum of the un-compressed trace $h(t)$ and the uniformly compressed trace takes the form $1/mh(t/m)$, then the spectrum of the compressed trace is simply a frequency-scaled version $H(mf)$. This is the reason why Gaiser (1996), in his work on multicomponent Vp/Vs correlation analysis, implements a low-pass filter before transforming the PS-converted wave trace to P-wave times in a step which he describes as a matching of the PP and PS wavelengths.

As the stretching between PP- and PS-waves *only* concerns the reflectivities (the increasingly attenuated downgoing source wavelet is not affected by the different velocities for the PP-reflected and PS-converted waves), another implication of the similarity principle is that the source wavelet and effects of anelastic attenuation should be removed *before* stretching the PP-wave trace to PS-wave times. Since after inverse-Q filtering the spectra are significantly flatter, stretching (i.e., scaling) will not affect the spectra much. In contrast, if the PP-wave trace is stretched before removing the signature and attenuation effects, these common components will no longer match and hence can not be removed.

### Procedure and Example

Based on the discussion of non-stationary filtering above, the following procedure to calculate the PS-converted waves (or the horizontal component trace) from the primary PP-reflected waves now suggests itself:

1. Designature and time-variant inverse Q-filtering,
2. Reflectivity compensation and time-variant stretching to PS-times,
3. Signature and time-variant forward Q-filtering.

As all steps are described by non-stationary convolutions (i.e., matrix-vector multiplications), it is straightforward to combine them into a single non-stationary convolution by successive matrix multiplication[9].

---

[9] Notice that we could have chosen the opposite route as well: inverse-Q filtering the PS-converted wave trace, followed by compression to PP-wave traveltimes and forward Q-filtering. In principle, this approach is equally valid, however since the receiver function is defined as the deconvolution of the vertical component out of the horizontal component, it is natural to define the non-stationary filtering which, acting on $Z$, produces the horizontal component $X$. The resulting non-stationary filter matrix, $\mathbf{R}$, can then be seen as a generalized receiver function, as it constitutes the (2D) transfer function between the vertical component (PP-reflected waves) and the horizontal component (PS-converted waves).

To illustrate the procedure outlined above, synthetic multi-component data (primaries only) were generated for a simple horizontally layered model by randomly perturbing the shear-wave velocity obtained from Hamilton's, Gardner's and the Mudrock relations. PP-reflected and PS-converted wave traveltimes were calculated by raytracing through the resulting model and plane-wave reflection and conversion coefficients calculated using the relevant expressions from Aki and Richards (2002). The primary data were bandlimited using a 50Hz Ricker wavelet and forward Q-filtered (Q=50) to present realistically strong attenuation. The resulting PP-wave trace is shown in figure 5.18, top-middle panel.

Next, a non-stationary inverse-Q filter matrix was computed by calculating stabilized inverses of the bandlimited (by the source wavelet) forward-Q filters. The resulting filter matrix is shown in figure 5.18, top-left panel. Note that this step requires knowledge of Q and the source wavelet and normally would be done using a similar approach as Schoepp and Margrave (1998), i.e., by smoothing time-variant spectra and computing inverses of them. The result of applying the inverse-Q filter matrix to the PP-wave input trace is shown in the top-right panel. Following Margrave (1998), we have purposely placed the non-stationary filter matrices and the input and output traces to reflect the underlying corresponding matrix-vector multiplication.

In the second step, a non-stationary phase shift matrix was generated by interpolating the exact, time-varying traveltime differences for all 100 layers and computing accordingly delayed band-limited delta-functions. The resulting filter matrix is shown in figure 5.18, middle-left panel. This step also included a time-variant reflectivity compensation, obtained by interpolating the ratio of the PS-conversion and PP-reflection coefficient between each layer. In the middle-middle panel, the output trace from the top panel is repeated, as it now becomes the input for the time-variant stretching. The resulting time-stretched output trace is shown in the middle-right panel.

In the third and last step, the time-variant forward Q-filter and source wavelet are re-applied. Note that in this simple model there is no difference between the attenuation factor Q for the P-waves and for the S-waves. Thus, the same forward Q-filters can be applied to filter the reflectivity compensated and stretched output from the middle panel as were used to compute the initial attenuated

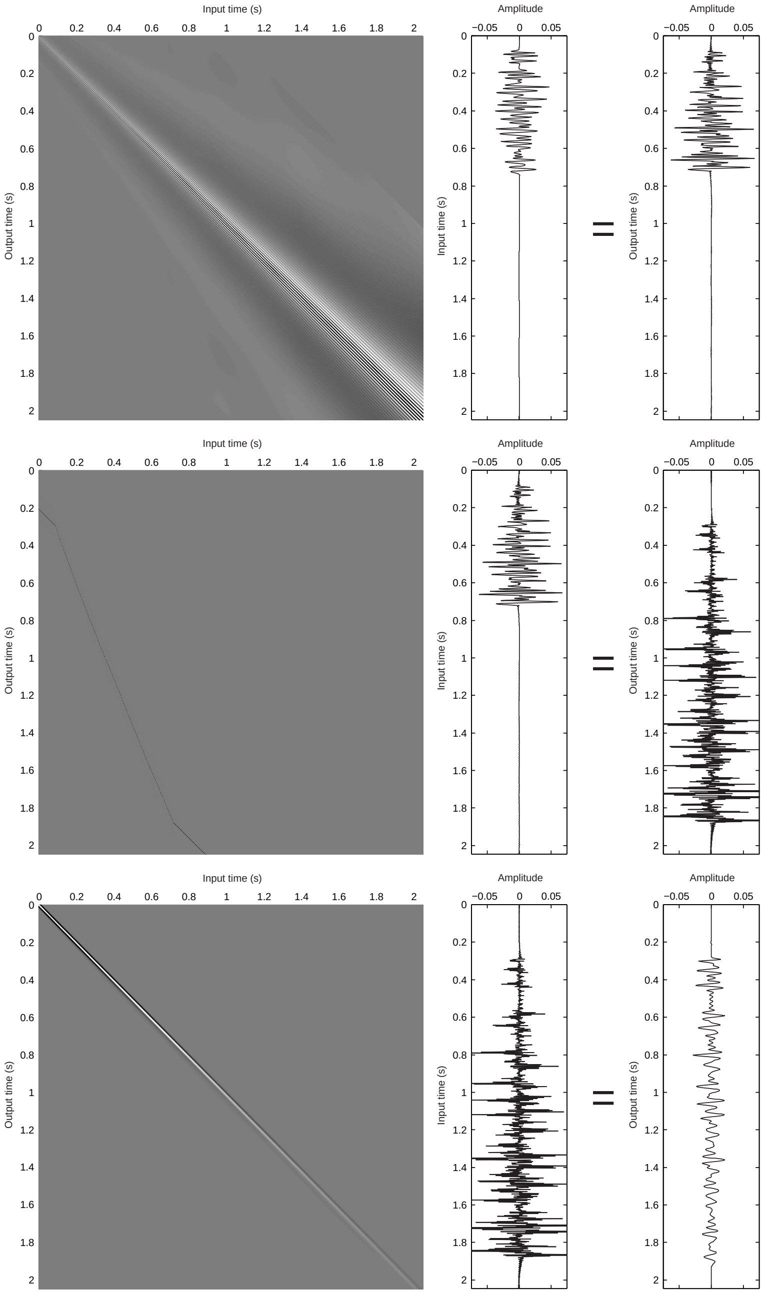

**Figure 5.18:** Time-variant filter model for reflection receiver functions. **(top)** Non-stationary inverse-Q filtering matrix (left) applied to the forward modeled PP-reflection data (center) by matrix-vector multiplication and the resulting inverse-Q filtered trace (right). **(middle)** Non-stationary phase shift matrix (left) applied to the inverse-Q filtering result from the top row (center) and the resulting trace stretched from PP- to PS-times (right). **(bottom)** Forward-Q filtering matrix (left) applied to the inverse-Q filtered, stretched result from the middle row (center), and the resulting pseudo PS-converted wave trace (right). By combining the three non-stationary filtering steps into a single non-stationary filtering step a generalized receiver function model is obtained.

PP-reflections. The resulting pseudo PS-converted wave trace is shown in the bottom-right panel.

### Discussion

The model outlined above conceptually generalizes the receiver function to the reflection seismic setting, while preserving the main attractive aspects of receiver function calculation in a transmission setting[10]. As there is no direct deconvolution of the two data traces with their countless PP- and PS-wave reflection pairs, a-causal and infinitely long transfer functions are avoided. Nevertheless, with that the simplicity and economy of the original approach are also lost: it is not clear how the receiver function transfer matrices can be estimated from the data in a single, deconvolution-like step without adding significant a-priori information.

While the inverse-Q filtering method by Schoepp and Margrave (1998) has seen some success in its application on field data, and the Vp/Vs correlation method by Gaiser (1996) has become the industry standard, both methods require a fair amount of interactive processing (and are thus usually applied post-stack) making this approach unattractive for pre-stack reflection receiver function calculation. Moreover, while together they provide all information necessary to calculate the receiver function, this is exactly the kind of information that would normally be obtained from the receiver function. Hence, such explicit processing undermines the very rationale behind receiver function calculation. At this point in time, it is an open question whether a direct method for estimating a non-stationary transfer matrix between two traces can be found.

## 5.8 Conclusion

This concludes the discussion of dynamic aspects of reflection receiver functions and also the receiver functions chapter. The previous two sections should have made it increasingly clear that it is not straightforward to come up with a model for reflection seismic receiver functions that is simple, preserves the advantages of the transmission setting and can handle an arbitrary number and complexity

---

[10] Designature and removal of common propagation effects.

of layers naturally. Indeed, it was shown that a simple convolutional model does not exist. Although time-variant convolutional models do exist, the receiver functions in such models become non-stationary filter matrices instead of single traces and inverting for them represents a seriously under-determined problem. In the discussion chapter we will briefly return to the problem of calculating a receiver functions in a seismic reflection setting and suggest research into a transformation approach which transforms reflection data into transmission data and vice-versa.

# *Chapter 6*

# Discussion

## 6.1 Interferometry: tunable full waveform modeling

A critical reader may well argue that no specific examples were given for which the interferometric modeling method is computationally cheaper than existing forward modeling methods. As argued in chapter 3, any discussion of a particular modeling scenario necessarily ignores one of the main advantages of the interferometric approach: namely, that one does not have to decide on a scenario upfront. This flexibility, that per definition cannot be expressed in terms of CPU time or the number of floating point operations, should rather be measured in terms of overall efficiency (including human) over the complete duration of a modeling project or application. The ability to meet changing requirements as the understanding of the modeler evolves, may well be one of the main advantages of the new method. Nevertheless, it is instructive to review some other promising approaches to reduce the cost of the new method, albeit at the expense of accuracy.

**Aperture** As shown in chapter 2, and originally suggested by Prof. Snieder (personal communication), in many cases there is a redundancy in the number of sources on the surrounding surface even when the boundary is sampled at the (local) Nyquist wavenumber. The phase of an arrival could still be reconstructed successfully after reducing the number of boundary sources by a factor of sixteen. The explanation for this, as in the case of super-resolution reported by Derode *et al.* (1995), is that strong multiple scattering augments the wavenumber spectrum, thus filling in gaps in the illumination by the sources on the surrounding surface and increasing their effective aperture.

**Illumination** Another case in which the number of sources on the surrounding surface can be reduced, is in the case of favorable geology. For example, in the truncated Pluto model discussed in chapter 3 and 4, it was noticed that the weighted crosscorrelations (in the interferometric construction) for boundary sources just below the salt did not contain any significant energy. This is because the high velocity of the salt bends the rays away from the vertical and hence produces a shadow zone beneath the salt. Because of reciprocity, boundary sources located in the shadow zone do not illuminate large parts of the model and hence can be neglected. Similarly, as explained in detail in chapter 3, no sources are required on interfaces with homogeneous boundary conditions. Thus, in some modeling scenarios where extremely large contrasts in acoustic or elastic impedances are encountered, it will be advantageous to let the surrounding surface coincide with such interfaces.

> *While raytracing can help to identify shadow zones along the boundary of the model, it should be mentioned that currently there is no mathematical or physical framework to determine, rigorously, a priori, which boundary sources can be neglected in the above two approaches. While for a particular pair of points in the medium, sources on the boundary in the point of interest gathers may not contain significant energy, it could be that for a different pair of points these sources do contain essential contributions.*

**Stationary phase** The closest thing to a mathematical framework to determine which source contributions can be neglected is probably the method of stationary phase. In the stationary phase interpretation (Snieder, 2004; Snieder *et al.*, 2006) an event will be reconstructed if the point for which the difference in traveltime to the two receivers is stationary wrt. position perturbations is included in the Kirchhoff integral. However, it is easy to show that even in the case of a single layer bounded by a free surface above and a half space below, an infinite number of such stationary points must exist – one for each multiple reflection bouncing back and forth between two points of interest. Similarly, in more complex models, in the presence of strong multiple scattering, a single boundary source may even act as stationary point for different events in the same reconstruction (i.e., between the same pair of points) in a non-trivial way. In principle, it is possible (and relatively straightforward) to determine such stationary points up to a predetermined order of events using a relatively cheap forward modeling algorithm such as raytracing. However, this seems contrary to the purpose of full waveform modeling in the first place. Besides, we have no guarantee that additional events (in addition to those ray-traced) will be reconstructed properly.

**Simultaneous sources** At this point I also would like to return briefly to the possibility of encoding the boundary sources using pseudo-noise sequences, which was discussed in detail in chapter 3. Some reviewers have argued that we are too pessimistic in our conclusion that encoding using orthogonal sequences does not pay off in forward modeling experiments. Perhaps they are right. To be clear, we never said that encoding using pseudo-noise sequences does not work – indeed it does work![1] – we merely emphasize that this will not be the holy grail that the full waveform modeling and inversion community is looking for. I feel that it is important to stress that having uncorrelated noise sources is not enough: one also has to listen (or model) long enough, or average over enough events, where long enough is dictated precisely by the signal-to-noise ratio that is required for the final application. And therein lies precisely the crux: while it is possible to speed up the computations by compromising on signal-to-noise ratio, in general, it will not be possible to achieve the same accuracy as the original finite-difference run at a reduced computational cost compared to the original simulations. In the physics of wave propagation there's no such thing as a free lunch!

**One-bit time-reversal** Another promising approach, that significantly reduces both the storage requirements and the cost of looking up a Green's function (but not the initial forward modeling effort), is suggested by the research of Derode

---

[1] For another recent example of successful simultaneous source encoding in the context of frequency domain forward modeling see Nihei and Nakagawa (2003).

*et al.* (1999). Discussing pulse compression with one-bit time reversal through multiple scattering they show that both the temporal and spatial resolutions of the refocused pulse remain unchanged when the scattered signals are digitized using only one bit. Moreover, in their experiments the compressed pulse is amplified by 12dB and the signal-to-noise ratio improved by 1.2 dB, making the one-bit results even better than the full 8-bit dynamic range digitization.

Derode *et al.* (1999) explain their results by remarking that although reducing the number of bits certainly changes the amplitude of the signal that is recorded on the time-reversal mirror, it does not change its correlation time. Another way of saying this is that the crucial information in the random signals for time-reversal and interferometry resides in the phase, or rather, the phase difference information of the recorded signals. Reconstruction (constructive and destructive interference) relies on phase differences being stationary and thus the amplitude of the reconstruction has perhaps more to do with the integral over the surrounding surface (the surface of Derode's time-reversal mirror) than the exact amplitude of the individual signals[2]. This observation is also consistent with the mentioned stability of time-reversal and the remarks of Snieder and Scales (1998), that the time-reversal mirror acts as a linear boundary condition on the time-reversed wavefield and therefore is robust to such dramatic changes in digitization.

Thus, it would be interesting to record the conventional full-precision boundary source simulations using a reduced number of bits (or, in the limit of one bit the sign only) in all points of interest. Note that this also has the desirable property of immediately reducing the storage requirements by a corresponding power of two and the look-up cost considerably as well! Again, I want to emphasize that the corresponding results will be approximate and that there is no real way, for a general model, to predict the accuracy of the reconstruction. Nevertheless, for sufficiently complex (read random) models, the results of Derode *et al.* (1999) are encouraging. Also, similar to the way in which the length of the orthogonal pseudo-noise sequence determines the accuracy of the results, here the accuracy can be controlled carefully through the number of bits in the recording.

---

[2] Note that this property is also exploited in methods that design signature deconvolution operators based on the full seismic trace. By applying a time-variant gain the later recorded data are weighted more equally and the dynamic range of the data, as in n-bit digitization, is reduced.

**Data compression** Clearly, the properties of the crosscorrelation and the linearity of the boundary condition on the time-reversal make the interferometric method also an ideal candidate to try various data compression algorithms (preferably to individual sources or to the point of interest gathers). While generally it is not possible to determine upfront whether a given reduction in boundary source sampling or in the number of bits used in digitization will lead to an acceptable noise level, a posteriori, the effect of such reductions can be evaluated and an optimal level, given the particular requirements for the data, chosen.

Thus, based on the above discussion on accuracy again a pattern of flexibility emerges: the interferometric modeling method allows compromising on accuracy while maintaining full multiple scattering. This aspect also makes the method an ideal candidate for full waveform inversion, where the sensitivity to the full data trace is maintained, while at the same time being able to trade-off the computational cost. This is also the case in the next section, where full waveform inversion in the frequency domain is discussed.

## 6.2 Frequency Domain Inversion (FDI)

In a typical FDI approach, (see e.g., Pratt *et al.*, 1998; Pratt, 1999), the acoustic or elastic wave equation is discretized in the frequency-space domain using a finite-difference or a finite-element approach and the resulting linear system of equations for a single frequency solved using direct matrix factorization methods. If LU factorization is used, Marfurt (1984) and Pratt and Worthington (1990) have shown that the matrix factors can be re-used to compute the response for a new source position using only a fraction (∼1 percent) of the time required to compute the original matrix factors (Stekl and Pratt, 1998). In addition, the frequency domain forward modeling approach leads to a straightforward matrix implementation of the backpropagation method of Lailly (1984) to compute the gradient of a misfit function (implicitly through the Frechet derivatives) in waveform inversion problems (see also section 6.4 below).

The interferometric modeling method does not rely on a frequency or time-domain implementation. Indeed, the equations for interferometric modeling in chapters 2 and 3 were derived in the frequency domain. The resulting multiplications with the complex conjugate were subsequently interpreted as crosscorrelations in the time domain. Thus, it is straightforward to apply the interferometric modeling method in conjunction with the frequency-domain forward modeling approach of Pratt *et al.* (e.g., 1998), with all the advantages discussed above. Since the response for different sources can be computed at only a fraction of the cost of the initial LU decomposition, the initial illumination of the model from a surrounding surface is cheap. Furthermore, instead of on the order of several thousand samples only one (complex-valued) sample needs to be stored for each frequency, reducing the storage requirements dramatically. Similarly, when looking up Green's functions only one complex multiplication needs to be computed for each boundary source and the results added.

It should be kept in mind however, that there could be some surprises when dealing with non-reciprocal absorbing boundary conditions in such methods (Pratt *et al.*, 1998, p. 344). With reciprocity such an essential ingredient of all time-reversal and interferometry-based methods, it may be that a renewed look at absorbing boundary conditions for frequency domain methods is required before interferometry can be applied. Also, it is an open question whether the exact boundary condition for non-linear model perturbations discussed in chapter 4 can be implemented in the frequency domain. The exact boundary condition relies heavily on causality and the condition of causality is not as easily ensured in the frequency domain as in the time domain. Since the benefits of a frequency domain approach are substantial, future research should address how to extend the exact boundary condition to the frequency domain.

## 6.3 Beyond 2D?

Unfortunately, the advantages of frequency domain finite-differences disappear when the method is applied to realistic 3D models and even the storage of the LU decomposition matrices becomes an problem. A similar storage problem also thwarts the interferometric modeling method: even for a relatively small 2D acoustic model of 300 x 300 gridpoints, storage of a reasonable subset of the Green's functions on the interior already requires up to 450 Gigabytes of data. Although such amounts of data are by no means show stoppers, for realistic 3D models we can forget about storing the response at all gridpoints in the medium and for all timesteps unless we find a way to drastically reduce both the internal memory and storage requirements.

Recently, however, an alternative approach has been suggested by Nihei and Nakagawa (2003), which keeps the advantages of the time-domain finite-difference approach in terms of algebraic complexity and memory requirements, while producing a single or a limited number of frequency outputs. The approach, which is based on so-called phase-sensitive detection (PSD), relies on running a time-domain finite-difference algorithm for a harmonic source out to steady state, before performing an integration over several cycles of the waveform correlated with a reference. Because the integration is performed as a running summation it is never necessary to store full waveforms.

The same approach could be applied to the interferometric modeling method. While not reducing the heavy computational burden, as frequency-domain finite-differences did in two-dimensions, this approach does reduce the storage requirements drastically. Another promising approach to reduce the computational and memory requirements associated with 3D full waveform inversion is to target the inversion to a particular region of interest. The potential of combining finite-difference injection techniques with interferometry to give flexible, targeted full waveform inversion is discussed next.

## 6.4 FD-injection + interferometry = targeted full waveform inversion

As mentioned above, Lailly (1984) and Tarantola (1984) have shown that by correlating backpropagated data-residuals with forward propagated wavefields, the gradient of the misfit function can be computed efficiently. Even though this approach reduces the number of forward modeling steps involved in the computation of the gradient for each shotpoint to two, the repeated modeling step still makes (frequency domain) full waveform inversion in 3D prohibitively expensive. Also, note that Marfurt (1984) and Pratt and Worthington (1990) do not teach us how to limit the modeling and inversion to a particular region of interest.

Robertsson and Chapman (2000), on the other hand, present an efficient method for updating full waveform seismograms after localized model perturbations. The method, based on superposition and continuity, works by recording the wavefield on a surface surrounding a region of interest during an initial run on the full grid and using the recorded wavefield to drive subsequent simulations on a smaller perturbed grid. In this way, all interactions with the exception of second and higher-order long-range interactions with the background model are properly accounted for (this, in stark contrast with hybrid methods). However, the authors do not discuss inversion. In another recent development, Valenciano *et al.* (2006) discuss targeted inversion. Their approach relies on writing the forward modeling operator in a target-oriented fashion and computing the Hessian explicitly. To limit the computational cost, one-way Green's functions are used.

It seems probable that by combining elements from both the global waveform inversion approach and the localized injection approach with interferometry that new, more optimal inversion strategies will be found. For example, instead of backpropagating the data-residuals through the background model using finite-differences on the full grid, one could compute a time-reversed injection wavefield by extrapolating data residuals from the surface through the background model using the Kirchhoff-Helmholtz integral and interferometrically computed Green's functions. The time-reversed injection wavefield would then drive a finite-difference simulation on the smaller (unperturbed) grid, giving rise to the exact same backpropagating data-residual wavefield that would have been obtained using finite-differences on the full grid. This so-called *missing diffracted field*, not taken into account by the current model (Tarantola, 1984), can then be correlated with the forward propagated wavefield in the usual way[3]. Alternatively, one could skip the injection step altogether and compute the forward and backward Kirchhoff-Helmholtz integral for each point in the target region explicitly and correlate the resulting extrapolated wavefields. The merits of each approach obviously depend on the number of points in the subgrid and the relative cost of Kirchhoff extrapolation vs. finite-differences, but are clearly more efficient than computing finite-differences on the full grid.

Note that, although interferometry is not strictly required for the above described application, interferometry provides the full waveform Green's functions for the background model cheaply (once the initial computational burden has been paid-off), consistently (compare with the one-way Green's functions of Valenciano *et al.* (2006) and other hybrid approaches) and flexibly – allowing the target region to be redefined, extended or completely changed without incurring significant new computational costs.

## 6.5 Receiver functions and a possible relation with interferometry

In the chapter on receiver functions, it was shown that the kinematic treatment of receiver functions can be extended quite far along the lines of conventional converted wave processing (e.g., by following the work of Harrison, 1992). It appears completely feasible to formulate such concepts as moveout correction,

---

[3] Note that one could also compute the forward injection wavefield interferometrically and inject the forward and time-reversed data-residual wavefield simultaneously, making use of linearity of the solutions of the wave-equation. The conventional zero-lag crosscorrelation can then be calculated implicitly in the finite-difference calculation on the subgrid through a running summation (integration) of the field variable(s) over time.

stacking, dip moveout and pre- and post-stack time or depth migration for receiver functions. Nevertheless, such kinematic extensions will only be successful if the receiver functions input to such algorithms have well defined meanings and simple interpretations, dynamically speaking. For receiver functions in a reflection seismic setting this is debatable at least. Due to the increased number of events on the vertical component in a reflection setting, there is no well defined (stationary) transfer function between the vertical and the horizontal components and the deconvolution (or crosscorrelation) thus produces a trace with many more events than the desired number of primary PP- and PS-converted wave pairs and without obvious interpretation. The concept of a receiver function simply cannot be extended in a straightforward manner to the reflection setting. As shown, even when adopting a non-stationary filter model along the lines of Margrave (1998), the resulting transfer function is not a *function*, but rather a *matrix* and it is not clear how this matrix, with its many more degrees of freedom, can be estimated cheaply and robustly without performing full converted wave processing.

At this point, it is interesting to step back a little and think a bit more about the fundamental differences between reflection and transmission data: what is the fundamental difference between reflection and transmission data? Are reflection data intrinsically “more complicated” than transmission data? Does reflection data contain more “information” than transmission data, or less, or perhaps equal? Or is it better to think of reflection and transmission data as complementary? A partial answer to this question, which bring us back to interferometry, was given by Claerbout, in a classic paper in 1968 titled: “Synthesis of a layered medium from its acoustic transmission response”. As the answer turned out to be surprisingly brief and simple, we can directly quote it from the paper here:

> *The reflection seismogram from a surface source and a surface receiver is one side of the autocorrelation of the seismogram from a source at depth and the same receiver.*

Thus, if we have measured the transmission response of a layered medium, we can reconstruct the reflection response simply by calculating the autocorrelation of the transmission response and taking one side of it.

Notice that Claerbout’s result seems to imply that the reflection and transmission responses indeed contain the same amount of information, since one can be calculated from the other by the process of spectral factorization. For horizontally layered acoustic media, embedded between two halfspaces, this is almost certainly the case. Recently Wapenaar (2004) generalized Claerbout's results to arbitrary inhomogeneous elastic media.

A more promising approach to receiver function therefore suggests itself: if it were possible to transform the multi-component reflection data into the equivalent multi-component transmission data for the same model, receiver function analysis could be applied to the transmission data using conventional methods and the extended kinematics presented in this thesis could be applied without all the problems associated with the increased number of events on the vertical component.

At this point it should be mentioned that for the acoustic case Thorbecke *et al.* (2003) have shown that the transmission *coda* that can be retrieved from reflection data but not the absolute transmission time of a primary due to a source below the stack of layers. It is not clear how this result generalizes to a horizontally layered elastic medium. For the above suggestion to work, it is important that the relative PP- and PS-converted wave transmission times are preserved. If this is not the case, then there is no merit in transforming the reflection data into transmission coda. It has also been pointed out (Wapenaar, 2007, personal communication) that the extension of the reflection-transmission transforms to 3D acoustic media is not straightforward either.

It is beyond the scope of this thesis to investigate the possible use of such reflection-transmission transforms for receiver function calculation. A brief survey of the existing literature however suggests that this may be a much harder problem than it appears to be at first sight. Going from transmission data to reflection data is relatively easy, as the interferometric Green's function constructions show. As mentioned in the introduction, already in 1968, Claerbout speculated that *"the synthesis problem with p-sv conversions may be solvable with two-channel time-series analysis."*.

Given the fact that it took more than 30 years to prove Claerbout's first conjecture, I will modestly conclude here by saying that interferometry, now perhaps more than ever, holds great promise and will continue to inspire researchers for many years to come!

# References

Aki, K. and Richards, P.G., 2002. *Quantitative Seismology (second edition)*. University Science Books.

Akkermans, E., Wolf, P.E., Maynard, R. and Maret, G., 1988. Theoretical study of the coherent backscattering of light by disordered media. *Journal de Physique France*, **48**, 77–98.

Amundsen, L. and Reitan, A., 1995. Decomposition of multicomponent sea-floor data into upgoing and downgoing p- and s-waves. *Geophysics*, **60**, 563–572.

Amundsen, L., Røsten, T., Robertsson, J.O.A. and Kragh, E., 2005. Rough-sea deghosting of streamer seismic data using pressure gradient approximations. *Geophysics*, **70**, V1–V9.

Bakulin, A. and Calvert, R., 2004. Virtual source: new method for imaging and 4d below complex overburden. 2477–2480.

Bakulin, A. and Calvert, R., 2006. The virtual source method: Theory and case study. *Geophysics*, **71**, SI139–SI150.

Bojarski, N.N., 1983. Generalized reaction principles and reciprocity theorems for the wave equations, and the relationship between the time-advanced and time-retarded fields. *Journal of the Acoustical Society of America*, **74**, 281–285.

Bracewell, R., 1965. *The Fourier Transform and its Application*. McGraw-Hill, Inc., New York, first edition.

Bregman, N.D., Chapman, C.H. and Bailey, R.C., 1985. A noniterative procedure for inverting plane-wave reflection data at several angles of incidence using the riccati equation. *Geophysical Prospecting*, **33**, 185–200.

Carazzone, J.J., 1992. Inversion of P-SV seismic data. *Geophysics*, **51**, 1056–1068.

Cassereau, D. and Fink, M., 1992. Time-Reversal of Ultrasonic Fields-Part III: Theory of the Closed Time-Reversal Cavity. *IEEE Transactions on Ultrasonics, Ferroellectrics, and Frequency Control*, **39**, 579–592.

Cassereau, D. and Fink, M., 1993. Focusing with plane time-reversal mirrors: an efficient alternative to closed cavities. *Journal of the Acoustical Society of America*, **94**, 2373–2386.

Claerbout, J., 1976. *Fundamentals of geophysical data processing*. McGraw Hill.

Claerbout, J.F., 1968. Synthesis of a layered medium from its acoustic transmission response. *Geophysics*, **68**, 264–269.

Clayton, R. and Engquist, B., 1977. Absorbing boundary conditions for acoustic and elastic wave equations. *Bulletin of the Seismological Society of America*, **67**, 1529–1540.

Dankbaar, J.W.M., 1985. Separation of P- and S-waves. *Geophysical Prospecting*, **33**, 970–986.

de Hoop, A.T., 1988. Time-domain reciprocity theorems for acoustic wave fields in fluids with relaxation. *J. Acoust. Soc. Am.*, **84**, 1877–1882.

de Hoop, A.T., 1995. *Handbook of Radiation and Scattering of Waves*. Academic Press.

de Rosny, J. and Fink, M., 2002. Overcoming the Diffraction Limit in Wave Physics Using a Time-Reversal Mirror and a Novel Acoustic Sink. *Physical Review Letters*, **89**, 124301.

de Rosny, J., Tourin, A., Derode, A., van Tiggelen, B. and Fink, M., 2004. Relation between time reversal focusing and coherent backscattering in multiple scattering media: A diagrammatic approach. *Physical Review E*, **70**, 046601.

Derode, A., Roux, P. and Fink, M., 1995. Robust Acoustic Time Reversal with High-Order Multiple Scattering. *Physical Review Letters*, **75**, 4206.

Derode, A., Tourin, A. and Fink, M., 1999. Ultrasonic pulse compression with one-bit time reversal through multiple scattering. *Journal of Applied Physics*, **85**, 6343–6352.

Derode, A., Larose, E., Tanter, M., de Rosny, J., Tourin, A., Campillo, M. and Fink, M., 2003. Recovering the Green's function from field-field correlations in an open scattering medium (L). *Journal of the Acoustical Society of America*, **113**, 2973–2976.

Dix, C.H., 1955. Seismic velocities from surface measurements. *Geophysics*, **20**, 68–86.

Donati, M.S. and Stewart, R.R., 1996. P- and S-wave separation at a liquid-solid interface. *Journal of Seismic Exploration*, **5**, 113–127.

Draeger, C. and Fink, M., 1999. One-channel time-reversal in chaotic cavities: Theoretical limits. *Journal of the Acoustical Society of America*, **105**, 611–617.

Eaton, D.W.S., Stewart, R.R. and Harrison, M.P., 1991. The Fresnel zone for P-SV waves. *Geophysics*, **56**, 360–364.

Fan, P. and Darnell, M., 2003. Sequence Design for communications applications. *Research Studies Press, Hertfordshire UK*.

Fokkema, J.T. and van den Berg, P.M., 1993. *Seismic Applications of Acoustic Reciprocity*. Elsevier.

Foldy, L.L., 1945. The Multiple Scattering of Waves. *Physical Review*, **67**, 107–119.

Gaiser, J.E., 1996. Multicomponent $\mathrm{V_P/V_S}$ correlation analysis. *Geophysics*, **61**, 1137–1149.

Ghosh, S. and Kumar, P., 2002. Divergent and asymptotic nature of the time-offset Taner-Koehler series in reflection seismics. *Geophysics*, **67**, 1913–1919.

Givoli, D. and Cohen, D., 1995. Nonreflecting Boundary Conditions Based on Kirchhoff-Type Formulae. *J. Comp. Phys.*, **117**, 102–113.

Grechka, V. and Dewangan, P., 2003. Generation and processing of pseudo-shear-wave data: Theory and case study. *Geophysics*, **68**, 1807–1816.

Grechka, V. and Tsvankin, I., 2002. PP + PS = SS. *Geophysics*, **67**, 1961–1971.

Groenenboom, J. and Snieder, R., 1995. Attenuation, dispersion and anisotropy by multiple scattering of transmitted waves through distributions of scatters. *Journal of the Acoustical Society of America*, **98**, 3482–3492.

Gurrola, H., Minster, J.B. and Owens, T., 1994. The use of velocity spectrum stacks for stacking receiver functions and imaging upper mantle discontinuities. *Geophysical Journal International*, **117**, 427–440.

Harrison, M.P., 1992. *Processing of P-SV Surface-Seismic Data: Anisotropy Analysis, Dip Moveout, and Migration*. Ph.D. thesis, The University of Calgary, Edmonton, Alberta, Canada.

Hokstad, K., Mittet, R. and Landrø, M., 1998. Elastic reverse time migration of marine walkaway vertical seismic profile data. *Geophysics*, **63**, 1685–1695.

Holvik, E., 2003. *Betti designature and elastic demultiple of multi-component seismic data*. Ph.D. thesis, NTNU Trondheim, Norway, Norway.

Holvik, E. and Amundsen, L., 2005. Elimination of the overburden response from multicomponent source and receiver seismic data, with source designature and decomposition into PP-, PS-, SP-, and SS-wave responses. *Geophysics*, **70**, 43–59.

Kennett, B.L.N., 1983. *Seismic Wave Propagation in Stratified Media*. Cambridge University Press.

Krey, T., 1954. Bemerkung zu einer Formel für geschwindigkeitsbestimmungen aus seismischen Messungen von C.H. Dix. *Erdöl und Kohle*, **7**, 8–9.

Lailly, P., 1984. The seismic inverse problem as a sequence of before stack migrations. *SIAM Conference on Inverese Scattering, Tulsa, Oklahoma*.

Langston, C.A., 1979. Structure under Mount Ranier, Washington, inferred from teleseismic body waves. *Journal of Geophysical Research*, **84**, 4749–4762.

Levin, V. and Park, J., 1997. P-SH conversions in a flat-layered medium with anisotropy of arbitrary orientation. *Geophysical Journal International*, **131**, 253–266.

Marfurt, K.J., 1984. Accuracy of finite-difference and finite-element modeling of the scalar and elastic wave equations. *Geophysics*, **49**, 533–549.

Margrave, G.F., 1998. Theory of nonstationary linear filtering in the Fourier domain with application to time-variant filtering. *Geophysics*, **63**, 244–259.

Mittet, R., 1994. Implementation of the Kirchhoff integral for elastic waves in staggered-grid modeling schemes. *Geophysics*, **59**, 1894–1901.

Nihei, K.T. and Nakagawa, S., 2003. An Efficient Approach for Computing the Frequency Response of Seismic Waves in Heterogeneous, Anisotropic Viscoelastic Media With FDTD+PSD Modeling. *Eos. Trans. AGU, Fall Meet. Suppl., Abstract*, **84**, S22G–07.

Oristaglio, M.L., 1989. An inverse scattering formula that uses all the data. *Inverse Problems*, **5**, 1097–1105.

Paulssen, H., Visser, J. and Nolet, G., 1993. The crustal structure from teleseismic P-wave coda - I. Method. *Geophysical Journal International*, **112**, 15–25.

Phinney, R.A., 1964. Structure of the Earth's Crust from spectral behaviour of long-period body waves. *Journal of Geophysical Research*, **69**, 2997–3017.

Porter, R.P., 1969. Image formation with arbitrary holographic type surfaces. *Physics Letters*, **29A**, 193–194.

Porter, R.P., 1970. Diffraction-Limited, Scalar Image Formation with Holograms of Arbitrary Shape. *Journal of the Optical Society of America*, **60**, 1051–1059.

Pratt, G., Shin, C. and Hicks, 1998. Gauss-newton and full newton methods in frequency-space seismic waveform inversion. *Geophysical Journal International*, **133**, 341–362.

Pratt, R.G., 1999. Seismic waveform inversion in the frequency domain, part 1: Theory and verification in a physical scale model. *Geophysics*, **64**, 888–901.

Pratt, R.G. and Worthington, M., 1990. Inverse theory applied to multi-source cross-hole tomography. part i: acoustic wave-equation method. *Geophysical Prospecting*, **38**, 287–310.

Rickett, J.E. and Claerbout, J.F., 2000. Calculation of the acoustic solar impulse response by multi-dimensional spectral factorization. *Solar Physics*, **192**, 203–210.

Robertsson, J.O.A. and Chapman, C.H., 2000. An efficient method for calculating finite-difference seismograms after model alterations. *Geophysics*, **65**, 907–918.

Robertsson, J.O.A. and Curtis, A., 2002. Wavefield separation using densely deployed three-component single-sensor groups in land surface-seismic recordings. *Geophysics*, **67**, 1624–1633.

Robertsson, J.O.A. and Kragh, E., 2002. Rough-sea deghosting using a single streamer and a pressure gradient approximation. *Geophysics*, **67**, 2005–2011.

Robertsson, J.O.A., Blanch, J.O. and Symes, W.W., 1994. Viscoelastic finite-difference modeling. *Geophysics*, **59**, 1444–1456.

Robinson, E.A., 1982. Spectral Approach to Geophysical Inversion by Lorentz, Fourier and Radon Transforms. In *Proc. IEEE, Volume 70, p. 1039-1054*, 1039–1054.

Robinson, E.A. and Treitel, S., 2002. *Geophysical Signal Analysis*. Society of Exploration Geophysicists, Tulsa, Oklahoma.

Rodriguez-Suarez, C., Stewart, R. and Margrave, G., 2000. Where does S-wave energy on OBC recordings come from. *70th Annual International Meeting, Society of Exploration Geophysicists, Expanded Abstracts*, 1170–1173.

Rose, J.H., 2002. *Imaging of Complex Media with Acoustic and Seismic Waves*, vol. 84 of *Topics Appl. Phys.*, chap. Time Reversal, Focusing and Exact Inverse Scattering, 97–105. Springer-Verlag Berlin Heidelberg.

Røsten, T., van Manen, D., Robertsson, J.O.A. and Amundsen, L., 2002. Optimal nonrecursive and recursive spatial filters for demultiple of OBS data. *72nd Annual International Meeting, Society of Exploration Geophysicists, Expanded Abstracts*, 1022–1025.

Ryberg, T. and Weber, M., 2000. Receiver function arrays; a reflection seismic approach. *Geophysical Journal International*, **141**, 1–11.

Schalkwijk, K.M., Wapenaar, C.P.A. and Verschuur, D.J., 1999. Application of two-step decomposition to multicomponent ocean-bottom data: Theory and case study. *Journal of Seismic Exploration*, **8**, 261–278.

Schoepp, A.R. and Margrave, G.F., 1998. Improving seismic resolution with nonstationary deconvolution. *68th Annual International Meeting, Society of Exploration Geophysicists, Expanded Abstracts*, 1096–1099.

Schuster, G.T., 1985. A hybrid BIE+Born series modeling scheme: Generalized Born series. *J. Acoust. Soc. Am.*, **77**, 865–879.

Schuster, G.T., 2001. Theory of daylight/interferometric imaging: tutorial. *63rd Annual International Meeting, European Association of Geoscientists and Engineers, Extended Abstracts*, A–32.

Snieder, R., 2002. *Scattering and Inverse Scattering in Pure and Applied Science*, chap. General Theory of Elastic Wave Scattering, 528–542. Academic Press, San Diego.

Snieder, R., 2004. Extracting the Green's function from the correlation of coda waves: A derivation based on stationary phase. *Physical Review E*, **69**, 46610.

Snieder, R. and Scales, J.A., 1998. Time-reversed imaging as a diagnostic of wave and particle chaos. *Physical Review E*, **58**, 5668–5675.

Snieder, R., Wapenaar, K. and Larner, K., 2006. Spurious multiples in seismic interferometry of primaries. *Geophysics*, **71**, SI111–SI124.

Stekl, I. and Pratt, R.G., 1998. Accurate viscoelastic modeling by frequency-domain finite differences using rotated operators. *Geophysics*, **63**, 1779–1794.

Stoughton, D., Stefani, J. and Michell, S., 2001. 2-D elastic model for wavefield investigations of subsalt objectives, deep water Gulf of Mexico. *71st Annual International Meeting, Society of Exploration Geophysicists, Expanded Abstracts*, 1269–1272.

Taner, M. and Koehler, F., 1969. Velocity spectra - digital computer derivation and applications of velocity functions. *Geophysics*, **34**, 859–881.

Tarantola, A., 1984. Inversion of seismic reflection data in the acoustic approximation. *Geophysics*, **49**, 1259–1266.

Teng, Z., 2003. Exact boundary condition for time-dependent wave equation based on boundary integral. *J. Comp. Phys.*, **190**, 398–418.

Tessmer, G. and Behle, A., 1988. Common reflection point data-stacking technique for converted waves. *Geophysical Prospecting*, **36**, 671–688.

Thorbecke, J., Wapenaar, K. and Dragonov, D., 2003. From reflection data to transmission coda. *65th Annual International Meeting, European Association of Geoscientists and Engineers, Extended Abstracts*, P142.

Ting, L. and Miksis, M.J., 1986. Exact boundary conditions for scattering problems. *J. Acoust. Soc. Am.*, **80**, 1825–1827.

Valenciano, A.A., Biondi, B. and Guitton, A., 2006. Target-oriented wave-equation inversion. *Geophysics*, **71**.

van Manen, D., 2001. *Seabed receiver statics using receiver functions*. Master's thesis, Utrecht University, the Netherlands.

van Manen, D., Robertsson, J.O.A., Curtis, A., Ferber, R. and Paulssen, H., 2003. Shear wave statics using receiver functions. *Geophysical Journal International*, **153**, F1–F5.

van Manen, D., Robertsson, J.O.A. and Curtis, A., 2005. Modeling of Wave Propagation in Inhomogeneous Media. *Physical Review Letters*, **94**, 164301.

van Manen, D., Curtis, A. and Robertsson, J.O.A., 2006. Interferometric modeling of wave propagation in inhomogeneous elastic media using time reversal and reciprocity. *Geophysics*, **71**, SI47–SI60.

van Manen, D.J., Robertsson, J.O.A., Røsten, T., Amundsen, L. and Strømmen-Melbø, A., 2004. Decomposition and Calibration of Multicomponent Data in the Common Shot Domain. *66th Annual International Meeting, European Association of Geoscientists and Engineers, Extended Abstracts*, D–26.

Vinnik, L.P., 1977. Detection of waves converted from P to SV in the mantle. *Physics of the Earth and Planetary Interiors*, **15**.

Wapenaar, C.P.A. and Haimé, G.C., 1990. Elastic extrapolation of primary seismic P- and S-waves. *Geophysical Prospecting*, **38**, 23–60.

Wapenaar, K., 2003. Synthesis of an inhomogeneous medium from its acoustic transmission response. *Geophysics*, **68**, 1756–1759.

Wapenaar, K., 2004. Retrieving the Elastodynamic Green's Function of an Arbitrary Inhomogeneous Medium by Cross Correlation. *Physical Review Letters*, **93**, 254301.

Wapenaar, K. and Fokkema, J., 2004. Reciprocity theorems for diffusion, flow and waves. *Journal of Applied Mechanics*, **71**, 145–150.

Wapenaar, K. and Fokkema, J., 2006. Green's function representations for seismic interferometry. *Geophysics*, **71**, SI33–SI46.

Wapenaar, K., Draganov, D. and Thorbecke, J., 2004. Relations between reflection and transmission responses of three-dimensional inhomogeneous media. *Geophysical Journal International*, **156**, 179–194.

Wapenaar, K., Fokkema, J. and Snieder, R., 2005. Retrieving the Green's function in an open system by cross-correlation: a comparison of approaches (L). *Journal of the Acoustical Society of America*, **118**, 2783–2786.

Weaver, R., 1990. Anderson localization of ultrasound. *Wave Motion*, **12**, 129–142.

Weaver, R.L. and Lobkis, O.I., 2001. Ultrasonics without a Source: Thermal Fluctuation Correlations at MHz Frequencies. *Physical Review Letters*, **87**, 134301.

Weaver, R.L. and Lobkis, O.I., 2003. Elastic wave thermal fluctuations, ultrasonic waveforms by correlation of thermal phonons. *Journal of the Acoustical Society of America*, **113**, 2611–2621.

Weaver, R.L. and Lobkis, O.I., 2006. Diffuse fields in ultrasonics and seismology. *Geophysics*, **71**, SI5–SI9.

Welch, L.R., 1974. Lower bounds on the maximum cross correlation of signals. *IEEE Transactions on Information Theory*, **20**, 397–399.

Yagle, A.E. and Levy, B.C., 1984. Application of the Schur Algorithm to the Inverse Problem for a Layered Acoustic Medium. *Journal of the Acoustical Society of America*, **76**, 301–308.

Yagle, A.E. and Levy, B.C., 1985. A Layer Stripping Solution of the Inverse Problem for a One-Dimensional Elastic Medium. *Geophysics*, **50**, 425–433.

Zhang, J. and Langston, C.A., 1995. Dipping Structure under Dourbes, Belgium, Determined by Receiver Function Modeling and Inversion. *Bulletin of the Seismological Society of America*, **85**, 254–268.

# *Appendix A*

# Computation of the gradient by spatial filtering

It is well known that when the wavefield on a boundary satisfies outgoing (i.e., radiation or absorbing) boundary conditions, the wavefield and its gradient (or traction) are directly related. For example, Holvik and Amundsen (2005) derive the following expressions in the frequency-wavenumber $(\omega, \mathbf{k})$-domain that relate the upgoing components of particle velocity $\mathbf{V}^{(up)}(\mathbf{k})$ of a plane wave propagating with horizontal slowness $\mathbf{p} = (\mathbf{k}/\omega)$ to the upgoing traction $\mathbf{T}^{(up)}(\mathbf{k})$ across a horizontal array of receivers (sources):

$$\mathbf{T}^{(up)}(\mathbf{k}) = \mathbf{L}_{TV}(\mathbf{k})\mathbf{V}^{(up)}(\mathbf{k}), \tag{A.1}$$

where the particle velocity and traction vector are defined as

$$\begin{aligned} \mathbf{V}^{(up)} &= \left(V_1^{(up)}, V_2^{(up)}, V_3^{(up)}\right)^T & \text{(A.2)} \\ \mathbf{T}^{(up)} &= \left(T_1^{(up)}, T_2^{(up)}, T_3^{(up)}\right)^T & \text{(A.3)} \end{aligned}$$

and $^T$ denotes transposed. The $3 \times 3$ matrix $\mathbf{L}_{TV}(\mathbf{k})$ is derived as (Holvik and Amundsen, 2005):

$$\mathbf{L}_{TV} = \frac{\rho\omega}{k_\phi} \begin{pmatrix} k_{z,\alpha} - \frac{k_y^2}{k_\beta^2}(k_{z,\alpha} - k_{z,\beta}) & \frac{k_x k_y}{k_\beta^2}(k_{z,\alpha} - k_{z,\beta}) & k_x(1 - 2k_\beta^{-2}k_\phi) \\ \frac{k_x k_y}{k_\beta^2}(k_{z,\alpha} - k_{z,\beta}) & k_{z,\alpha} - \frac{k_x^2}{k_\beta^2}(k_{z,\alpha} - k_{z,\beta}) & k_y(1 - 2k_\beta^{-2}k_\phi) \\ -k_x(1 - 2k_\beta^{-2}k_\phi) & -k_y(1 - 2k_\beta^{-2}k_\phi) & k_{z,\beta} \end{pmatrix}. \tag{A.4}$$

In equation A.4, $k_x$ and $k_y$ are the components of the wavenumber vector parallel to the array of receivers (sources), $k_r = (k_x^2 + k_y^2)^{\frac{1}{2}}$ is the length of the wavenumber vector and $k_{z,\alpha} = (k_\alpha^2 - k_r^2)^{\frac{1}{2}}$ and $k_{z,\beta} = (k_\beta^2 - k_r^2)^{\frac{1}{2}}$ are the P- and S-wavenumbers perpendicular to the array of receivers (sources) respectively with $k_\alpha = (\omega/\alpha)$ and $k_\beta = (\omega/\beta)$ the P- and S-wavenumbers. In addition, an auxiliary quantity $k_\phi = k_r^2 + k_{z,\alpha} k_{z,\beta}$ has been defined.

Similarly, for acoustic waves propagating in a single direction across an array, the pressure $P(\mathbf{k})$ and its gradient $\nabla P(\mathbf{k})$ are related through:

$$\frac{\partial P}{\partial n} \equiv \mathbf{n} \cdot \nabla P = i k_{z,\alpha} P, \tag{A.5}$$

where $\mathbf{n}$ is the normal to the array and $i$ is the imaginary unit. Note that these relations depend on material properties and require that the medium is (locally) laterally homogeneous.

Thus, equations A.1 and A.5 allow us to calculate the outgoing traction or pressure gradient associated with the modeled particle velocity or pressure on the surface surrounding the medium because absorbing boundaries were included right outside the enclosing boundary during the modeling.

The implementation of equations A.1 and A.5 is straightforward when the wavefield is recorded (or emitted) on a linear array of regularly spaced receivers (sources) embedded in a homogeneous medium. In that case, the point of interest gathers can be directly transformed to the frequency-wavenumber domain and the matrix multiplication carried out explicitly before the components of the resulting traction vector are inverse-Fourier transformed to the space-frequency domain.

Alternatively, when the medium is laterally varying or the array of receivers (sources) is curved, equation A.1 can be implemented by designing spatially compact filters that approximate the terms of $\mathbf{L}_{TV}$ (or, in the acoustic case, $i\omega q_\alpha$) and filtering the data in the space-frequency domain. Such an approach has been used in, for instance, the seabed seismic setting to decompose the wavefield measured at the seabed into up- and downgoing P- and S-waves (Røsten *et al.*, 2002; van Manen *et al.*, 2004) and is based on solving a linear least-squares problem with (in-)equality constraints to find a small number of spatial filter coefficients with a wavenumber spectrum that best matches the spectrum of the analytical expression. Since the analytical expressions (equations A.4 and A.5) are functions of frequency, this optimization is carried out for each frequency separately. The laterally varying seafloor properties are accommodated by designing such compact filters for the particular seafloor properties that are present at each receiver location. These filters are then applied to the point of interest gathers in the space-frequency domain by space-variant convolution.

Note that the filter coefficients only have to be optimized once for a particular model and can be reused for all Green's functions that are computed in the intercorrelation phase. This approach was tested on acoustic data computed for the Pluto model (modeled with $\beta = 0$ m/s) and gave good results.

# *Appendix B*

# The Welch bound and limits to encoding using pseudo-noise sequences

In communications analysis, the problem of encoding and decoding signals using pseudo-noise sequences and its limits are well known. In particular, Welch (1974) has shown that for any family of $M$ (unit energy) sequences $\{a_n^{(i)}\}$, $i = 0, \ldots, M-1$, $n = 0, \ldots, N-1$ of length $N$, a lower bound on the maximum (aperiodic) crosscorrelation or off-peak autocorrelation is

$$C_{max} = \max\{C_{am}, C_{cm}\} \geq \sqrt{\frac{M-1}{M(2N-1)-1}} \tag{B.1}$$

where $C_{am}$ and $C_{cm}$ are the maximum off-peak autocorrelation and maximum crosscorrelation values defined by

$$\begin{aligned} C_{am} &= \max_{i} \max_{1<\tau\leq N-1} |C_{i,i}(\tau)| \\ C_{cm} &= \max_{i\neq j} \max_{0<\tau\leq N-1} |C_{i,j}(\tau)| \end{aligned}$$

and $C_{i,j}$ is the discrete aperiodic correlation function of the sequences $a_n^{(i)}$ and $a_n^{(j)}$ defined as

$$C_{i,j}(\tau) = \begin{cases} \sum_{n=0}^{N-1-\tau} a_n^{(i)} a_{n+\tau}^{(j)}, & 0 \leq \tau \leq N-1 \\ \sum_{n=0}^{N-1+\tau} a_{n-\tau}^{(i)} a_n^{(j)}, & -N+1 \leq \tau < 0 \\ 0, & |\tau| \geq N. \end{cases}$$

Note that the Welch bound (equation B.1) holds without reference to a particular type of sequence set [e.g., maximal, Kasami or Gold sequences (Fan and Darnell, 2003)]. This means that when we encode signals using sequences of any such family, superpose the encoded signals and subsequently decode using crosscorrelation, there will be some point in the decoded output where the interference between the original data sequences is at least $C_{max}$. We can estimate the best possible performance that can be expected [without making any (questionable) assumptions about the uncorrelatedness of the Green's functions from boundary sources to points of interest] by looking at the (rms) expected signal-to-interference ratio when all members $a_n^{(i)}$ of the sequence set are simply added and the result $r_n$ is autocorrelated. Thus we have

$$r_n = \sum_i a_n^{(i)} \tag{B.2}$$

and the corresponding autocorrelation $C_r$,

$$C_r(\tau) = \sum_{n=0}^{N-1-\tau} r_n r_{n+\tau}, \quad 0 \leq \tau \leq N-1, \tag{B.3}$$

which, using equation B.2 can be written

$$C_r(\tau) = \underbrace{\sum_i \sum_{n=0}^{N-1-\tau} a_n^{(i)} a_{n+\tau}^{(i)}}_{C_D(\tau)} + \underbrace{\sum_{i \neq j} \sum_{n=0}^{N-1-\tau} a_n^{(i)} a_{n+\tau}^{(j)}}_{C_C(\tau)}. \tag{B.4}$$

The first term denotes the diagonal, or signal term $C_D(\tau)$ whereas the second term $C_C(\tau)$ denotes the cross-terms related to the (unwanted) interference between the different codes and contains a double summation.

Equation B.4 mimics the structure of the interferometric modeling equations (equations 3.10 and 3.11): when the boundary source signals are encoded using pseudo-noise sequences and excited simultaneously, it is their superposition (convolved with the Green's function) that is recorded in the points of interest, and when calculating the Green's function, decoding, crosscorrelation and summation are implicit in a direct correlation (just like in a typical retrieval of the Green's function from uncorrelated noise sources). Thus, as long as we assume that the Green's functions from the boundary to the points of interest do not influence the signal-to-interference ratio, an estimate of the ratio can be found by analyzing equation B.4. This is done by comparing the expected magnitude of the first term to the magnitude of the second term. Since the diagonal term consists of a sum of the autocorrelations of the sequences, its magnitude is maximum at zero-lag ($\tau = 0$) and equal to the family size $M$:

$$C_D(0) = \sum_i \sum_{n=0}^{N-1} a_n^{(i)} a_n^{(i)} = M \tag{B.5}$$

because the signals are unit energy. The expected value of the second term, is actually calculated by Welch as part of his derivation of equation B.1. In fact, Welch's original statement is basically a lower bound on the root-mean-square value of a family of unit energy signals:

$$C_{rms} \geq \sqrt{\frac{M-1}{M(2N-1)-1}} \tag{B.6}$$

and since $C_{max} \geq C_{rms}$, equation B.1 follows. Thus, the Welch bound gives the rms-value of each of the terms within the double sum in $C_C(\tau)$. Note that the sign of each of these $M(M-1)$ terms is not directly specified through the Welch bound. The only thing we can say about the sign is that its expected value is zero when the DC component of the sequences vanishes and the sequences are (in the ensemble average) uncorrelated. Thus, we estimate the magnitude of the term $C_C(\tau)$ by calculating the variance of

$$C_C(\tau) = \underbrace{\pm C_{rms} \pm C_{rms} \pm C_{rms} \ldots}_{M(M-1)\text{terms}} \tag{B.7}$$

which simply is

$$\langle C_C(\tau) \rangle^{\frac{1}{2}} = \sqrt{M(M-1)} C_{rms} \tag{B.8}$$

and the ratio of the signal term to the interference term becomes

$$\frac{C_D(0)}{\langle C_C(\tau)\rangle^{\frac{1}{2}}} \approx M\sqrt{\frac{M(2N-1)-1}{M(M-1)^2}}. \tag{B.9}$$

When both the sequence length $N$ and the family size $M$ are much larger than one, this becomes

$$\frac{C_D(0)}{\langle C_C(\tau)\rangle^{\frac{1}{2}}} \approx \sqrt{2N}. \tag{B.10}$$

Thus, the signal-to-interference ratio improves as the square-root of the sequence length.

# *Appendix C*

# Series expansion of the traveltime difference as function of slowness

In this Appendix, the difference in traveltime between a P-wave and PS-wave, converted at the base of layer $n$ is expanded into a Taylor series of increasing powers of slowness $p$. This leads naturally to a small slowness approximation, similar to the near-offset approximation in reflection seismics. As discussed in the main text, the traveltime difference can be written:

$$dt = \sum_{k=1}^{n} h_k \left( \sqrt{Vs_k^{-2} - p^2} - \sqrt{Vp_k^{-2} - p^2} \right). \tag{C.1}$$

Equation C.1 contains terms of the form: $(1 - p^2v^2)^{\frac{1}{2}}$, where $v$ can denote either the P- or S-wave velocity. Such terms can be expanded into a Taylor series as follows:

$$\left(1 - p^2v^2\right)^{\frac{1}{2}} = \sum_{j=0}^{\infty} q_j \left(p^2v^2\right)^j = 1 - \frac{1}{2}\left(p^2v^2\right) - \frac{1}{8}\left(p^2v^2\right)^2 - \frac{1}{16}\left(p^2v^2\right)^3 - \ldots, \tag{C.2}$$

where the coefficients $q_j$ are given by:

$$q_0 = 1, \quad q_j = \frac{\frac{1}{2}\left(\frac{1}{2}-1\right)\left(\frac{1}{2}-2\right) \times \ldots \times \left(\frac{1}{2}-j+1\right)}{j!} \left(-1\right)^j. \tag{C.3}$$

Substituting equation C.2 into equation C.1, the traveltime difference can be written:

$$dt = \sum_{j=0}^{\infty} q_j \sum_{k=1}^{n} h_k \left( Vs_k^{2j-1} - Vp_k^{2j-1} \right) \left( p^2 \right)^j . \tag{C.4}$$

Equation C.4 is an expansion of the traveltime difference between plane P- and PS-converted waves through an $n$-layered medium in increasing even powers of slowness. Note that the accuracy of the expansion is directly related to the accuracy of the substituted Taylor series approximation (equation C.2), which means that the product $p^2v^2$ should be small (at least the waves should be propagating) throughout the stack. Therefore the product of the highest P-velocity and the slowness determine the accuracy of equation C.4.

If we assume that $p^2v^2 \ll 1$, we can truncate the infinite series given by equation C.4 after the second term and neglect terms of fourth order in slowness and higher. This gives the small-slowness, or short-spread approximation:

$$dt^{\mathrm{smallp}} = \sum_{k=1}^{n} h_k \left( Vs_k^{-1} - Vp_k^{-1} \right) + \frac{1}{2} \sum_{k=1}^{n} h_k \left( Vp_k - Vs_k \right) p^2 . \tag{C.5}$$

# *Appendix D*

# A Dix-Krey-type relation for receiver function pseudo rms-velocities

The definition of a pseudo rms-velocity in equation 5.16 allows the derivation of a Dix-Krey-type formula that that relates the pseudo rms-velocities to the product of P- and S-wave interval velocities, as will be shown below. We apply a similar analysis as Tessmer and Behle (1988) and express the thickness $h_k$ of layer $k$ in terms of the one-way vertical traveltimes $\tau_k^p$ and $\tau_k^s$ and interval velocities in that layer:

$$h_k = \frac{1}{2}\left(Vp_k\tau_k^p + Vs_k\tau_k^s\right). \tag{D.1}$$

Furthermore the ratio of vertical one-way traveltimes equals the inverse of the ratio of interval velocities:

$$\frac{\tau_k^p}{\tau_k^s} = \frac{Vs_k}{Vp_k}. \tag{D.2}$$

If equation D.1 is subsituted into the definition of the pseudo rms-velocity (equation 5.16) and the identity D.2 is used, we arrive at the following expression for the pseudo rms-velocity at layers $n$ and $n-1$:

$$\tilde{v}_{\rm rms}^{n} = \frac{1}{2}\sum_{k=1}^{n}\left(\tau_k^s - \tau_k^p\right)\cdot Vs_kVp_k, \tag{D.3}$$

$$\tilde{v}_{\rm rms}^{n-1} = \frac{1}{2}\sum_{k=1}^{n-1}\left(\tau_k^s - \tau_k^p\right)\cdot Vs_kVp_k. \tag{D.4}$$

Subtracting equation D.4 from equation D.3, one arrives at:

$$Vs_n Vp_n = 2 \cdot \frac{\tilde{v}^n_{\mathrm{rms}} - \tilde{v}^{n-1}_{\mathrm{rms}}}{(\tau^s_n - \tau^p_n)}. \tag{D.5}$$

Finally, using the fact that the difference in vertical one-way S- and P-traveltime through layer $n$ is equal to the difference in vertical incidence traveltime differences between layer $n$ and layer $n-1$:

$$(\tau^s_k - \tau^p_k) = dt^n_0 - dt^{n-1}_0, \tag{D.6}$$

one arrives at:

$$Vs_n Vp_n = 2 \cdot \frac{\tilde{v}^n_{\mathrm{rms}} - \tilde{v}^{n-1}_{\mathrm{rms}}}{dt^n_0 - dt^{n-1}_0}. \tag{D.7}$$

Equation D.7 is the equivalent of the Dix-Krey-type formula derived by Tessmer and Behle (1988) for converted waves. It says that the product of P- and S-wave interval velocities in layer $n$ is simply twice the ratio of the differences in pseudo rms-velocities and vertical incidence traveltime differences. Equation D.7 can easily be verified by directly substituting the definitions of the pseudo rms-velocities and vertical incidence traveltime differences (equations 5.16 and 5.15). Note that equation D.7 is substantially different from the result derived by Tessmer and Behle (1988) for converted waves. This is because our approximations of the moveout in the traveltime difference and corresponding definition of the pseudo rms-velocity are done in the slowness domain.

# *Appendix E*

# Expansion of the traveltime difference as function of the difference in horizontal distance

Following the analysis of Tessmer and Behle (1988), we expand both dt and dx in equations 5.24 and 5.25 into infinite series of even powers of slowness. Hereby we use the Taylor series expansion of the function $(1-p^2v^2)^{\frac{1}{2}}$, where $v$ can denote both the P- and S-wave velocity.

$$\begin{aligned}\left(1-p^2v^2\right)^{-\frac{1}{2}} &= \sum_{j=1}^{\infty} q_j \left(p^2v^2\right)^{j-1} \\ &= 1+\frac{1}{2}\left(p^2v^2\right)+\frac{1\times 3}{2\times 4}\left(p^2v^2\right)^2+\frac{1\times 3\times 5}{2\times 4\times 6}\left(p^2v^2\right)+..\end{aligned} \tag{E.1}$$

where the coefficients $q_j$ are given by:

$$q_1=1, q_j=\frac{1\times 3\times\cdots\times(2j-3)}{2\times 4\times\cdots\times(2j-2)}. \tag{E.2}$$

Note that this expansion is the inverse of the expansion used in the previous sections (see equation C.2). We substitute equation E.1 into equations 5.24 and 5.25 for terms containing either P- or S-velocities to obtain infinite series for dt and dx:

$$\begin{aligned} dt &= \sum_{j=1}^{\infty} q_j \sum_{k=1}^{n} h_k \left( V s_k^{2j-3} - V p_k^{2j-3} \right) \left( p^{2j-2} \right), && \text{(E.3)} \\ dx &= \sum_{j=1}^{\infty} q_j \sum_{k=1}^{n} h_k \left( V s_k^{2j-1} - V p_k^{2j-1} \right) \left( p^{2j-1} \right). && \text{(E.4)} \end{aligned}$$

To simplify the appearance of equations E.3, E.4 and subsequent derivations, we define the following coefficients:

$$\begin{aligned} a_m &= \sum_{k=1}^{n} h_k \left( V s_k^{2m-3} - V p^{2m-3} \right), && \text{(E.5)} \\ b_m &= -q_m a_{m+1}, && \text{(E.6)} \\ \gamma_m &= q_m a_m. && \text{(E.7)} \end{aligned}$$

Using these, equations E.3 and E.4 become:

$$\begin{aligned} dt &= \sum_{j=1}^{\infty} \gamma_j p^{2j-2}, && \text{(E.8)} \\ dx &= p \sum_{j=1}^{\infty} b_j p^{2j-2}. && \text{(E.9)} \end{aligned}$$

The explicit form of equation 5.31 in the main text can be found by squaring the power series for $dt$ (equation E.8), calculating successive even powers of $dx$ (equation E.9) and ordering terms of equal powers in slowness $p$. We start by squaring $dx$:

$$\begin{aligned} dx^2 &= \left( p \sum_{k=1}^{\infty} b_k p^{2j-2} \right)^2 \\ &= p^2 \left( b_1 + b_2 p^2 + b_3 p^4 + b_4 p^6 + \cdots \right)^2 \\ &= p^2 \big( b_1^2 + \left( b_1 b_2 + b_2 b_1 \right) p^2 + \left( b_1 b_3 + b_2^2 + b_3 b_1 \right) p^4 \\ &\quad + \left( b_1 b_4 + b_2 b_3 + b_3 b_2 + b_4 b_1 \right) p^6 + \ldots \big) \\ &= p^2 \sum_{k=1}^{\infty} B_{k1} p^{2k-2}, && \text{(E.10)} \end{aligned}$$

where,

$$B_{k1} = b_1 b_k + b_2 b_{k-1} + \cdots + b_{k-1} b_2 + b_k b_1. \tag{E.11}$$

The higher, even powers of this series can be found by recursively applying equation E.10 to find the coefficients. This leads to the following result:

$$dx^{2n} = \sum_{k=1}^{\infty} B_{kn} p^{2k-2}, \tag{E.12}$$

where,

$$B_{kn} = B_{11} B_{k,n-1} + B_{21} B_{k-1,n-1} + \cdots + B_{k-1,1} B_{2,n-1} + B_{k1} B_{1,n-1}. \tag{E.13}$$

Note that the coefficients $B_{kn}$ have to be calculated recursively since they contain coefficients $B_{\dots,n-1}$. The same methodology can also be applied to find the square of $dt$ and we find:

$$\begin{aligned} dt^2 &= \left(\sum_{k=1}^{\infty} A_k p^{2k-2}\right) = c_1 + c_2 \cdot \underbrace{\left(p^2 \sum_{k=1}^{\infty} B_{k1} p^{2k-2}\right)}_{dx^2} \\ &+ c_3 \cdot \underbrace{\left(p^4 \sum_{k=1}^{\infty} B_{k2} p^{2k-2}\right)}_{dx^4} + c_4 \cdot \underbrace{\left(p^6 \sum_{k=1}^{\infty} B_{k3} p^{2k-2}\right)}_{dx^6} + c_5 \cdots, \end{aligned} \tag{E.14}$$

where,

$$A_k = \gamma_1 \gamma_k + \gamma_2 \gamma_{k-1} + \cdots + \gamma_{k-1} \gamma_2 + \gamma_k \gamma_1. \tag{E.15}$$

Hence, written out up to 6th order in $p$, equation E.14 becomes:

$$\begin{aligned} A_1 &+ A_2 p^2 + A_3 p^4 + A_4 p^6 + \cdots = \\ &c_1 + c_2 B_{11} p^2 + (c_2 B_{21} + c_3 B_{12})\, p^4 + (c_2 B_{31} + c_3 B_{22} + c_4 B_{13})\, p^6 + \cdots. \end{aligned}$$

Thus, we find for the first two coefficients, using equations E.5, E.6 and E.7,

$$c_1 = A_1 = \gamma_1^2 = (q_1 a_1)^2 = \left(\sum_{k=1}^{n} h_k \left(\frac{1}{Vs_k} - \frac{1}{Vp_k}\right)\right)^2 \equiv dt_0^2, \tag{E.16}$$

$$c_2 = \frac{A_2}{B_{11}} = \frac{2\gamma_1\gamma_2}{b_1^2} \frac{a_1}{a_2} = \frac{\sum_{k=1}^{n} h_k \left(\frac{1}{Vs_k} - \frac{1}{Vp_k}\right)}{\sum_{k=1}^{n} h_k \left(Vs_k - Vp_k\right)} \equiv \frac{1}{v_{rms}^2}. \tag{E.17}$$

# *Appendix F*

# A Dix-Krey relation for reflection seismic receiver functions

Analogous to the treatment in Appendix D, Dix-Krey-type relations can also be derived for the approximations of the traveltime difference as a function of the difference in horizontal travel distance, as developed in Appendix E. This is the topic of the current Appendix. As we will see, the result will relate the rms-velocities defined in the previous Appendix to the products of P- and S-wave interval velocities. We start from the squared rms-velocity:

$$v_{rms}^2 = \frac{\sum_{k=1}^{n} h_k \left(Vs_k - Vp_k\right)}{dt_0^2}. \tag{F.1}$$

Again, we proceed by using equation D.1 for the thickness of a layer $k$ and the ratio of one-way vertical traveltimes (equation D.2) to rewrite the numerator in equation F.1 and we have:

$$\begin{aligned} \sum_{k=1}^{n} h_k \left(Vs_k - Vp_k\right) &= \sum_{k=1}^{n} \frac{1}{2} \left(Vp_k \tau_k^p + Vs_k \tau_k^s\right) \left(Vs_k - Vp_k\right) \\ &= \sum_{k=1}^{n} \left(\tau_k^p - \tau_k^s\right) \cdot Vs_k Vp_k. \end{aligned} \tag{F.2}$$

Hence, combining equations F.2 and F.1, we find for layer $n$ and $n-1$ respectively:

$$dt_0^n v_{rms,n}^2 = \sum_{k=1}^{n} (\tau_k^p - \tau_k^s) \cdot Vp_k Vs_k, \tag{F.3}$$

$$dt_0^{n-1} v_{rms,n-1}^2 = \sum_{k=1}^{n-1} (\tau_k^p - \tau_k^s) \cdot Vp_k Vs_k, \tag{F.4}$$

Subtracting equation F.4 from equation F.3, we find for the product of P- and S-wave interval velocities in layer $n$:

$$Vp_n Vs_n = \frac{dt_0^n v_{rms,n}^2 - dt_0^{n-1} v_{rms,n-1}^2}{(\tau_n^p - \tau_n^s)}, \tag{F.5}$$

Now finally, using that:

$$(\tau_n^p - \tau_n^s) = dt_0^n - dt_0^{n-1}, \tag{F.6}$$

equation F.5 can be written:

$$Vp_n Vs_n = \frac{dt_0^n v_{rms,n}^2 - dt_0^{n-1} v_{rms,n-1}^2}{\left(dt_0^n - dt_0^{n-1}\right)}, \tag{F.7}$$

Equation F.7 is the desired result. It shows how the product of P- and S-wave interval velocities for a layer $k$, can be calculated once the rms-velocities and the vertical incidence time differences for that layer and the previous layer are known. Equation F.7 has exactly the same form as found previously for PS-converted waves by Tessmer and Behle (1988). Note however that the vertical incidence traveltime differences and rms-velocities are defined differently, as shown in Appendix E.

# *Appendix G*

# Analytical expressions for the receiver function in a two-layer medium

To get a better feeling for difference between a reflection and a transmission receiver function, we will now expand the approximate equation for the reflection seismic receiver function into an infinite series. As mentioned previously, division in the frequency domain, corresponds to deconvolution in the time domain. Alternatively, if we can calculate the inverse of the vertical component, we may convolve the numerator with the time-domain equivalent of the inverse. Hence, the objective of this section is to find the inverse of $Z_r(\omega)$ or, more correctly, of $Z_{r1}(\omega) + Z_{r2}(\omega)$:

$$Z_r^{-1}(\omega) \approx (Z_{r1}(\omega) + Z_{r2}(\omega))^{-1} = \frac{R_{pp1}^{-1} \cdot e^{+i\omega(2t_{p1})}}{1 + (R_{pp2}/R_{pp1}) \cdot e^{-i\omega(2t_{p2})}}. \tag{G.1}$$

Now if we define $k = (R_{pp2}/R_{pp1})$ and $z = \exp(-i\omega(2t_{p2}))$, the inverse of the denominator can be written:

$$\left(1 + (R_{pp2}/R_{pp1}) \cdot e^{-i\omega(2t_{p2})}\right)^{-1} = (1 + kz)^{-1}. \tag{G.2}$$

According to $k$ greater or smaller than one, equation G.2 signifies the inverse of a maximum or minimum delay wavelet respectively. In both cases a binomial expansion can be used to find a series approximation of the inverse (Robinson and Treitel, 2002). Both cases are now discussed in detail.

**Case 1:** $R_{pp1} < R_{pp2}$. In this case $k < 1$ and the stable inverse of a minimum-delay wavelet $(1, k)$ (in z-transform notation) is given:

$$(1 + kz)^{-1} = 1 - kz + k^2 z^2 - k^3 z^3 + k^4 z^4 - \cdots .$$

Substituting the infinite series in equation G.1, we find:

$$\frac{R_{pp1}^{-1} \cdot e^{+i\omega(2t_{p1})}}{1 + (R_{pp2}/R_{pp1}) \cdot e^{-i\omega(2t_{p2})}} = \\ \frac{1}{R_{pp1}} e^{-i\omega(-2t_{p1})} - \frac{R_{pp2}}{R_{pp1}^2} e^{-i\omega(2t_{p2}-2t_{p1})} + \frac{R_{pp2}^2}{R_{pp1}^3} e^{-i\omega(4t_{p2}-2t_{p1})} - \cdots . \tag{G.3}$$

Using the first three terms of this expansion in the reflection receiver function (equation 5.57) we get:

$$\begin{aligned} H_r(\omega) \approx & \left(\frac{R_{ps1}}{R_{pp1}}\right)\left(\frac{R_{pp2}}{R_{pp1}}\right)^0 e^{-i\omega(t_{s1}-t_{p1}+0t_{p2})} \\ - & \left(\frac{R_{ps1}}{R_{pp1}}\right)\left(\frac{R_{pp2}}{R_{pp1}}\right)^1 e^{-i\omega(t_{s1}-t_{p1}+2t_{p2})} \\ + & \left(\frac{R_{ps1}}{R_{pp1}}\right)\left(\frac{R_{pp2}}{R_{pp1}}\right)^2 e^{-i\omega(t_{s1}-t_{p1}+4t_{p2})} \\ + & \left(\frac{R_{ps2}}{R_{pp2}}\right)\left(\frac{R_{pp2}}{R_{pp1}}\right)^1 e^{-i\omega(t_{s1}+t_{s2}-t_{p1}-t_{p2}+2t_{p2})} \\ - & \left(\frac{R_{ps2}}{R_{pp2}}\right)\left(\frac{R_{pp2}}{R_{pp1}}\right)^2 e^{-i\omega(t_{s1}+t_{s2}-t_{p1}-t_{p2}+4t_{p2})} \\ + & \left(\frac{R_{ps2}}{R_{pp2}}\right)\left(\frac{R_{pp2}}{R_{pp1}}\right)^3 e^{-i\omega(t_{s1}+t_{s2}-t_{p1}-t_{p2}+6t_{p2})}, \end{aligned}$$

where, to emphasize regularity, we have defined: $(R_{pp2}/R_{pp1})^0 \equiv 1$ and added the zero phase term: $0t_{p2}$. This result can be transformed to the time-domain and slightly rewritten, to find for the first six terms of the reflection receiver function:

$$\begin{aligned} h_r(t) \approx\; & \left(\frac{R_{ps1}}{R_{pp1}}\right)\left(\frac{R_{pp2}}{R_{pp1}}\right)^0 \delta\left(t-(t_{s1}-t_{p1})-0t_{p2}\right) \\ - & \left(\frac{R_{ps1}}{R_{pp1}}\right)\left(\frac{R_{pp2}}{R_{pp1}}\right)^1 \delta\left(t-(t_{s1}-t_{p1})-2t_{p2}\right) \\ + & \left(\frac{R_{ps1}}{R_{pp1}}\right)\left(\frac{R_{pp2}}{R_{pp1}}\right)^2 \delta\left(t-(t_{s1}-t_{p1})-4t_{p2}\right) \\ + & \left(\frac{R_{ps2}}{R_{pp2}}\right)\left(\frac{R_{pp2}}{R_{pp1}}\right)^1 \delta\left(t-(t_{s1}+t_{s2}-t_{p1}-t_{p2})-2t_{p2}\right) \\ - & \left(\frac{R_{ps2}}{R_{pp2}}\right)\left(\frac{R_{pp2}}{R_{pp1}}\right)^2 \delta\left(t-(t_{s1}+t_{s2}-t_{p1}-t_{p2})-4t_{p2}\right) \\ + & \left(\frac{R_{ps2}}{R_{pp2}}\right)\left(\frac{R_{pp2}}{R_{pp1}}\right)^3 \delta\left(t-(t_{s1}+t_{s2}-t_{p1}-t_{p2})-6t_{p2}\right). \end{aligned} \tag{G.4}$$

Equation G.4 gives us some insight into the nature of the receiver function in a two layer reflection setting. The first term can be recognised as $h_{r1}(t)$, the partial receiver function for the first layer. This term has both the desired amplitude and phase, giving information about the ratio of the P-wave reflection and PS-wave conversion coefficients at the first interface and the difference in traveltime between the P- and PS-wave reflection at that interface.

The next two events are shifted - with respect to the traveltime difference through the first layer - by an integer number of times the traveltime through layer 2. To see why this is the case, one has to realize that the time through layer 2 equals the difference in traveltime between a P-wave reflected at layers 1 and 2. The amplitude of the second and third events is the ratio of the P-wave reflection and PS-conversion coefficients at the first interface modified by the ratio (squared) of the P-wave reflection coefficients at the two interfaces.

The last three terms can be interpreted similarly, but now relative to the traveltime difference between the PS-wave and the P-wave reflection at the second interface (i.e., $t_{s1}+t_{s2}-t_{p1}-t_{p2}$) and the corresponding ratio of reflection and conversion coefficients (i.e., $R_{ps2}/R_{pp2}$). Again, we see that the events are shifted by an integer number of times the traveltime through layer 2 and scaled by increasing powers of the ratio of P-wave reflection coefficients at the first and second interface.

**Case 2:** $R_{pp2} > R_{pp1}$. For completeness, I now discuss the case when the reflection coefficient at the second interface is larger than the first. We will see that this case is slightly different from the previous case considered. Since in this case $k > 1$, we need to find the inverse of a maximum-delay wavelet $(1, k)$. However, the causal binomial expansion used in the previous section is unstable when $k > 1$, so in this case we have to use the anti-causal binomial expansion:

$$(1 + kz)^{-1} = k^{-1}z^{-1} - k^{-2}z^{-2} + k^{-3}z^{-3} - k^{-4}z^{-4} + k^{-5}z^{-5} - \cdots .$$

Substituting $k$ and $z$ in the infinite series, we find for equation G.1:

$$\begin{aligned} &\frac{R_{pp1}^{-1} \cdot e^{+i\omega(2t_{p1})}}{1 + (R_{pp2}/R_{pp1}) \cdot e^{-i\omega(2t_{p2})}} = \\ &\quad \frac{1}{R_{pp2}} e^{+i\omega(2t_{p1}+2t_{p2})} - \frac{R_{pp1}}{R_{pp2}^2} e^{+i\omega(2t_{p1}+4t_{p2})} + \frac{R_{pp1}^2}{R_{pp2}^3} e^{+i\omega(4t_{p1}+6t_{p2})} - \cdots . \end{aligned} \tag{G.5}$$

Using the first three terms of this expansion in the reflection receiver function we get:

$$\begin{aligned} H_r(\omega) \;\approx\; & \left(\frac{R_{ps1}}{R_{pp1}}\right)\left(\frac{R_{pp1}}{R_{pp2}}\right)^1 e^{-i\omega(t_{s1}-t_{p1}-2t_{p2})} \\ - & \left(\frac{R_{ps1}}{R_{pp1}}\right)\left(\frac{R_{pp1}}{R_{pp2}}\right)^2 e^{-i\omega(t_{s1}-t_{p1}-4t_{p2})} \\ + & \left(\frac{R_{ps1}}{R_{pp1}}\right)\left(\frac{R_{pp1}}{R_{pp2}}\right)^3 e^{-i\omega(t_{s1}-t_{p1}-6t_{p2})} \\ + & \left(\frac{R_{ps2}}{R_{pp2}}\right)\left(\frac{R_{pp1}}{R_{pp2}}\right)^0 e^{-i\omega(t_{s1}+t_{s2}-t_{p1}-t_{p2}-0t_{p2})} \\ - & \left(\frac{R_{ps2}}{R_{pp2}}\right)\left(\frac{R_{pp1}}{R_{pp2}}\right)^1 e^{-i\omega(t_{s1}+t_{s2}-t_{p1}-t_{p2}-2t_{p2})} \\ + & \left(\frac{R_{ps2}}{R_{pp2}}\right)\left(\frac{R_{pp1}}{R_{pp2}}\right)^2 e^{-i\omega(t_{s1}+t_{s2}-t_{p1}-t_{p2}-4t_{p2})} . \end{aligned} \tag{G.6}$$

where, again to emphasize regularity, we have used: $(R_{pp1}/R_{pp2})^0 \equiv 1$ and added the zero phase term: $0t_{p2}$. This result can be transformed to the time-domain, to find the first six terms of the reflection receiver function:

$$\begin{aligned}
h_r(t) \;\approx\;& \left(\frac{R_{ps1}}{R_{pp1}}\right)\left(\frac{R_{pp1}}{R_{pp2}}\right)^1 \delta\left(t-(t_{s1}-t_{p1})+2t_{p2}\right) \\
-\;& \left(\frac{R_{ps1}}{R_{pp1}}\right)\left(\frac{R_{pp1}}{R_{pp2}}\right)^2 \delta\left(t-(t_{s1}-t_{p1})+4t_{p2}\right) \\
+\;& \left(\frac{R_{ps1}}{R_{pp1}}\right)\left(\frac{R_{pp1}}{R_{pp2}}\right)^3 \delta\left(t-(t_{s1}-t_{p1})+6t_{p2}\right) \\
+\;& \left(\frac{R_{ps2}}{R_{pp2}}\right)\left(\frac{R_{pp1}}{R_{pp2}}\right)^0 \delta\left(t-(t_{s1}+t_{s2}-t_{p1}-t_{p2})\right) \\
-\;& \left(\frac{R_{ps2}}{R_{pp2}}\right)\left(\frac{R_{pp1}}{R_{pp2}}\right)^1 \delta\left(t-(t_{s1}+t_{s2}-t_{p1}-t_{p2})+2t_{p2}\right) \\
+\;& \left(\frac{R_{ps2}}{R_{pp2}}\right)\left(\frac{R_{pp1}}{R_{pp2}}\right)^2 \delta\left(t-(t_{s1}+t_{s2}-t_{p1}-t_{p2})+4t_{p2}\right). \qquad \text{(G.7)}
\end{aligned}$$

Equation G.7 can be compared with the time-domain expression G.4 found in the previous section for the case $R_{pp1} > R_{pp2}$. The fourth term can be recognised as $h_{r2}(t)$, or the partial receiver function for the second interface and hence provides the ratio of the P-wave reflection to the PS-conversion coefficient at the second interface and is positioned (in time) at the difference in traveltime between the P-wave reflected and the PS-wave converted at the second interface. The other terms can be interpreted as in the previous section, with one important difference: whereas for the case $R_{pp1} > R_{pp2}$, the additional terms where delayed by integer multiples of the two-way traveltime through the second layer, in this case the additional terms are advanced. This means that, as the order of the terms in the approximation increases, these terms will end up more and more before the zero-lag of the deconvolution, thus representing energy at a-causal time-lags.

The receiver function calculation for the two-layer example, both analytically and numerically, shows that even for a simple two-layer medium, the change from a seismological transmission setting to a seismic reflection setting makes the interpretation of the receiver function much more difficult and ambiguous than in the corresponding transmission setting. Depending on the relative size of the P-reflection coefficients, the inverse “filter” of the vertical component is either a causal, stable, infinite time function or an a-causal, stable, infinite time function. Convolution with this inverse thus introduces a (theoretically infinite) number of secondary events, which appear as noise at causal or a-causal time-lags. For the two-layer model, under the mentioned assumptions, only one of the many events in the receiver function gives unperturbed information about the ratio of reflection and conversion coefficients at one of the two interfaces and appears at the correct time-lag corresponding to the difference in traveltime between the PS-wave and the P-reflection at that interface.

The deliberate choice of a medium consisting of only two layers allowed the expansion of the inverse of the vertical component (or P-wave) recording. Unfortunately, it is not straightforward to apply the same methodology to find analytic approximations of the receiver function in a general multi-layered reflection seismic setting. This makes it difficult to predict exactly what the receiver function will look like for such a complicated but more realistic model and it is not clear what kind of information can be obtained from such a receiver function. Once again, in the transmission setting, adding a layer to the existing stack, to first order, only leads to an additional PS-converted wave, recorded dominantly on the radial component. The vertical component remains virtually unchanged. In the reflection seismic setting, the addition of a layer, introduces, under the same approximations, at least two events; a P-wave on the vertical component and a PS-wave converted upon reflection, recorded on the radial component. For a more complicated medium in a reflection setting, with many layers, it seems reasonable to expect that: (a) no simple inverse will exist for the vertical component P-wave data, (b) the inverse will contain energy at both a-causal and causal time-lags (the earth reflectivity is very probably not a minimum, or maximum phase wavelet) and (c) the relative timing and amplitude of the events in the receiver function may be distorted by this complicated inverse of the vertical component.

On the other hand, it could also be possible that the randomness or “whiteness” of the earth reflectivity leads to some kind of stabilization in the receiver function calculation, preserving some of the relative amplitude and phase information.